# Non-equilibrium dynamics of dipole-coupled internal states in cold gases

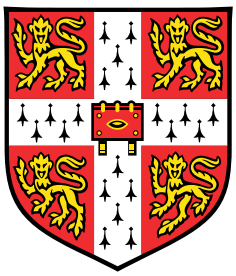

**Christopher David Parmee**

Department of Physics
University of Cambridge

This dissertation is submitted for the degree of
*Doctor of Philosophy*

Robinson College June 2019

# Declaration

This thesis describes work undertaken in the Theory of Condensed Matter Group (TCM) at the Cavendish Laboratory in Cambridge under the supervision of Prof. Nigel Cooper. Chapters 1 and 2 provide an introduction of the topics studied in this thesis, whereas the remaining chapters present work that is either published or being prepared for publication:

- **Chapter 3**: C. D. Parmee and N. R. Cooper, *Stable collective dynamics of two-level systems coupled by dipole interactions*, Phys. Rev. A 95, 033631 (2017) [1]
- **Chapter 4**: C. D. Parmee and N. R. Cooper, *Phases of driven two-level systems with nonlocal dissipation*, Phys. Rev. A 97, 053616 (2018) [2]
- **Chapter 5**: C. D. Parmee and N. R. Cooper, *Decay rates and energies of free magnons and bound states in dissipative XXZ chains*, arXiv:1812.07893 [3]
- **Chapter 6**: C. D. Parmee and N. R. Cooper, *Steady state phases of dissipative XXZ chains* (In preparation)

Parts of Chapters 1 and 3 were used in the Certificate of Postgraduate Studies report. Chapters 4-6 describe work carried out between January 2017 and March 2019. This dissertation is the result of my own work and includes nothing which is the outcome of work done in collaboration except as declared in the Preface and specified in the text. It is not substantially the same as any that I have submitted, or, is being concurrently submitted for a degree or diploma or other qualification at the University of Cambridge or any other University or similar institution except as declared in the Preface and specified in the text. I further state that no substantial part of my dissertation has already been submitted, or, is being concurrently submitted for any such degree, diploma or other qualification at the University of Cambridge or any other University of similar institution except as declared in the Preface and specified in the text. This thesis does not exceed 60,000 words.

Christopher David Parmee
June 2019

# Abstract

In this thesis, we consider the forms of non-equilibrium phenomena that can arise in atoms or polar molecules trapped in a deep optical lattice and coupled by dipolar internal degrees of freedom. We specifically focus on only two internal states, which results in the systems studied behaving as spin$-1/2$ models with long-range interactions.

We first study a closed system with both static and resonant near-field dipole interactions under an external drive. By studying the uniform mean-field dynamics of the system, we find the dynamics are given by Rabi oscillations, with a bifurcation in the dynamics as a function of drive strength between small scale and large scale oscillations. Analysing the stability of these oscillations to small fluctuations reveals that interactions tend to cause the oscillations to decohere. However, we find parameter regimes where coherent oscillations can persist for high enough intensity drive.

We then consider the effects of an environment on the non-equilibrium dynamics of the near-field dipole model. We find that within the mean-field approximation, an environment causes the system to relax to many novel steady state spin configurations, such as spin density waves, antiferromagnetism and long-time oscillations, as well as bistabilities between these phases. To assess the validity of the mean-field approximation, we compare our mean-field results to small quantum systems. We carry out a similar analysis on a system with far-field dipole interactions, where it is necessary to introduce nonlocal dissipation, which results in several decay modes into the environment. These decay modes lead to instabilities of many of the steady state phases that occurred in the near-field dipole system, leading to the emergence of more spin density wave and oscillatory phases.

Finally, we examine the dynamics on the approach to steady state in a dissipative dipolar system by studying Rydberg atoms coupled to a photonic crystal waveguide, which mediates an effective dipole-dipole interaction between the atoms. We find that if two excitations exist in the system, then bound states can form, with nonlocal dissipation resulting in a momentum dependent decay rate of the bound states and also greater freedom in engineering the bound state energy dispersion.

# Acknowledgements

First and foremost, I would like to thank my supervisor, Nigel, for his guidance, advice and many ideas and insights over the last three and a half years. It has been a pleasure to work with him and I have learnt a lot under his supervision.

Next, I am grateful to all those in TCM who I have come to know during my time here. I would like to thank Austen for providing advice on my first project, and also to all those who have given useful comments on my work at presentations. I would like to thank Eze for his numerous flattering sketches of me hidden throughout my work and the department, and Stephen and Max for the pub nights and for the fun company on the DesOEQ trips to Glasgow. I would also like to thank Eze and Stephen for proof reading parts of this thesis. I would like to thank my old office mates Daniel and Adam for being a source of useful scientific discussion and laughs, and my continued office mate, Benat, for being a source of constant confusion...(How do you think?). And finally, I would like to thank all the other friendly faces around TCM, who are too numerous to name. You have all made the department a welcoming and fun place to work during the PhD and I hope to stay in touch with as many of you as possible.

I would also like to mention those outside the department that made my time in Cambridge all that more enjoyable. I would like to thank Emma, for enduring my very minute periods of grumpiness, for her companionship and for supporting me throughout my PhD, as well as proof reading this thesis. I'd like to thank John for being a great friend and house mate over the years. I'd also like to thank the many friends from Robinson who have made my university days fun and memorable. A special thanks should also be given to all the Robinson cafe staff, for providing me with much needed coffee while I busied away in my usual spot.

Finally, I would like to thank my mum, dad and step mum for providing me with love and support throughout my Cambridge years, both before and during the PhD, as well as the rest of my family and friends from home.

# Contents

# Chapter 1

# Introduction

When atoms and molecules are cooled to low temperatures, their thermal energy becomes comparable to the energy scales of inter-particle interactions and quantum mechanical kinetic energy. The equivalence of these energy scales results in a significant interplay of these effects, leading to the emergence of new physical phenomena. The last few decades have seen major progress in observing these new phenomena in dilute cold gases, which have been cooled to near zero Kelvin. The first breakthrough was achieved by Chu, Cohen-Tannoudji and Phillips, who were awarded the 1997 Nobel prize [4] for engineering methods to cool and trap atoms using lasers and magnetic fields. These methods resulted in the production of optical molasses, gases of Sodium atoms at micro-Kelvin temperatures, which had greatly reduced velocities. The second breakthrough was by Ketterle, Cornell and Wieman with further cooling of gases by using a magneto-optical trap and evaporative cooling. This led to the achievement of nano-Kelvin temperatures and the realisation of the Bose Einstein condensate, a new phase of matter that is strongly characterised by quantum mechanical properties. For this result, Ketterle, Cornell and Wieman were awarded the 2001 Nobel prize [5]. Since these discoveries, the ability to readily produce ultracold atomic gases and molecules has opened up a new and exciting avenue to explore the effects of quantum mechanics and inter-particle interactions, and the discovery and realisation of other new exotic phenomena.

## 1.1 Quantum Simulation of Spin Systems

One of the most exciting aspects of ultracold atomic gases is the emerging field of quantum simulation. When theoretically modelling a quantum system, the biggest

obstacle one faces is the curse of dimensionality, where the dimension of a Hilbert space grows exponentially with the system size. Take, for example, $N$ two-level systems, for which the Hilbert space dimension grows as $2^N$. Classical computers can only currently simulate of the order $N \approx 30$ two-level systems and in order to simulate $N$ on the order of hundreds, you would need more atoms than are currently in the entire universe. The idea of a quantum simulator, suggested by Feynman [6], is to circumvent this issue by directly simulating the quantum dynamics in experiment and observing the outcome. While there are currently many theoretical ways to approximate the behaviour of large quantum systems, without direct simulation of the dynamics, it is difficult to tell what approximations are valid and when.

When building a quantum simulator, one usually wants to have the relevant particles studied to be subjected to periodic arrays, either to model crystalline materials or to exploit coherence effects. To do this, one can illuminate the particles with lasers, which results in a potential of the form [7]

$$V(\mathbf{r}) = -\mathbf{d}.\mathbf{E} = -\frac{1}{2}\beta\langle|\mathbf{E}(t,\mathbf{r})|^2\rangle_t, \tag{1.1}$$

where $\beta$ is the polarisability of the particle being illuminated, $\mathbf{d}$ is the dipole moment and $\mathbf{E}$ is the electric field from the laser. The angled brackets on the electric field represent temporal averaging. If counter-propagating lasers are used, the electric field is given by $\mathbf{E} = \mathbf{E}_0 \sin(\mathbf{k}\cdot\mathbf{r})$ and the potential takes the form

$$V(\mathbf{r}) = -\frac{\beta|\mathbf{E}_0|^2}{2}\sin^2(\mathbf{k}\cdot\mathbf{r}). \tag{1.2}$$

The particles now experience a periodic potential, known as an optical lattice. Optical lattices are an extremely versatile tool. By using different arrangements of lasers, it is possible to form a multitude of different lattice geometries such as 1D chains, 2D square and hexagonal lattices, as well as Kagome lattices, which can be used to study frustration effects, and also quasicrystal geometries [8]. By shaking the optical lattice, it is also possible to generate synthetic gauge fields [9] which can be used as a way to study the effects on magnetism on neutral particles. The high freedom and versatility of ultracold particles in optical lattices can be used to simulate a variety of real-world crystalline models and novel quantum phenomena [7, 10, 11].

In this thesis, we will be concerned with the quantum simulation of spin-1/2 systems, where each lattice site only contains two degrees of freedom. The following sections will

explain how these spin-1/2 systems can be realised, in ultracold gases and also other experimental settings, by exploiting either motional or internal degrees of freedom.

### 1.1.1 Motional Degrees of Freedom

When particles lie in an optical lattice, the dynamics of the particles depend on the depth of the lattice potential, which is given by $\beta|\mathbf{E}_0|^2/2$, in relation to the recoil energy, $\hbar^2|\mathbf{k}|^2/2m$, where $m$ is the mass of the particle. For sufficiently shallow lattices, we have $\beta|\mathbf{E}_0|^2/2 \sim \hbar^2|\mathbf{k}|^2/2m$ and it is possible for particles to quantum mechanically tunnel between different sites. To describe the behaviour of particles in the lattice, we consider the Hubbard model,

$$\hat{H}_{Hub} = -\sum_{\sigma}\sum_{\langle i,l\rangle}^{N} h_\sigma(\hat{a}^\dagger_{l,\sigma}\hat{a}_{i,\sigma} + \hat{a}_{l,\sigma}\hat{a}^\dagger_{i,\sigma}) + \sum_{\sigma}\sum_{l}^{N}\frac{U_\sigma}{2}\hat{n}_{l,\sigma}\left(\hat{n}_{l,\sigma}-1\right) + \sum_{l}^{N} U_{\uparrow\downarrow}\hat{n}_{l,\uparrow}\hat{n}_{l,\downarrow}, \quad (1.3)$$

where $\hat{a}^\dagger_{l,\sigma}$ and $\hat{a}_{l,\sigma}$ are either bosonic or fermionic operators, which create and destroy a particle on site $l$ respectively. The operator $\hat{n}_{l,\sigma} = \hat{a}^\dagger_{l,\sigma}\hat{a}_{l,\sigma}$ counts the number of particles on site $l$ [10, 12] and the index $\sigma$ indicates the spin of the particle, with $\sigma = \uparrow, \downarrow$. The first term in Eq. (1.3) is the kinetic energy of the particles hopping through the lattice, where the parameter $h_\sigma$ is the spin dependent hopping potential, which depends on the tunnelling strength between two adjacent sites. The second and third terms in Eq. (1.3) are onsite interaction terms, with strengths $U_\sigma$ and $U_{\uparrow\downarrow}$ respectively, which gives an energy cost for multiple occupation of a site. If the optical lattice is shallow, then $h_\sigma \gg U_\sigma, U_{\uparrow\downarrow}$ and so the particles are delocalised throughout the lattice rather than constrained on any site.

If the potential of the optical lattice is large however, such that $\beta|\mathbf{E}_0|^2/2 \gg \hbar^2|\mathbf{k}|^2/2m$, then $h_\sigma$ is small and tunnelling between sites is suppressed. In this case, $h_\sigma \ll U_\sigma, U_{\uparrow\downarrow}$, and so the system will lie in a Mott Insulator state where, on average, there is a single particle per site, with double occupation being unfavourable for $U_\sigma, U_{\uparrow\downarrow} > 0$. When this is the case, particles can still hop between sites, but only through swapping place with a nearby neighbour. For a spin-1/2 particle, particle motion coupled with the spin degree of freedom leads to a superexchange mechanism, that gives rise to an effective spin interaction of the following form [13]

$$\hat{H} = \sum_{\langle i,l\rangle}^{N} J_{zz}\hat{\sigma}^z_i\hat{\sigma}^z_l + J_{xy}\left(\hat{\sigma}^x_i\hat{\sigma}^x_l + \hat{\sigma}^y_i\hat{\sigma}^y_l\right), \quad (1.4)$$

where the $\langle . \rangle$ brackets indicate summation over nearest-neighbours only and the spin operators are defined as $\hat{\sigma}_l^z = |\uparrow_l\rangle\langle\uparrow_l| - |\downarrow_l\rangle\langle\downarrow_l|$, $\hat{\sigma}_l^y = -i|\uparrow_l\rangle\langle\downarrow_l| + i|\downarrow_l\rangle\langle\uparrow_l|$ and $\hat{\sigma}_l^x = |\uparrow_l\rangle\langle\downarrow_l| + |\downarrow_l\rangle\langle\uparrow_l|$. This is the XXZ model, and is just one example of how a spin-1/2 model can be engineered in cold atom gases. The parameters $J_{zz} = (h_\uparrow^2 + h_\downarrow^2)/2U_{\uparrow\downarrow}$ and $J_{xy} = h_\uparrow h_\downarrow / U_{\uparrow\downarrow}$ for fermions. This reduces to the well known Heisenberg model [14, 15] when $h_\uparrow = h_\downarrow$. For bosons, the parameters are given by $J_{zz} = (h_\uparrow^2 + h_\downarrow^2)/2U_{\uparrow\downarrow} - h_\uparrow^2/U_\uparrow - h_\downarrow^2/U_\downarrow$ and $J_{xy} = -h_\uparrow h_\downarrow / U_{\uparrow\downarrow}$ [13, 16].

We can also obtain spin Hamiltonians of the form in Eq. (1.4) when considering the Hubbard model, Eq. (1.3), with spinless ($\sigma$ takes only one value and $U_{\uparrow\downarrow} = 0$) fermions in a 1D optical lattice, when there are fewer fermions than lattice sites. Each site behaves as a spin-1/2 system, but with the spin degrees of freedom corresponding to a site being occupied ($|\uparrow_l\rangle$) or unoccupied ($|\downarrow_l\rangle$) rather than an internal spin degree of freedom as before. The Hubbard model, Eq. (1.3), can then be mapped to a spin system by applying the Jordan Wigner transformation [14]

$$\hat{\sigma}_l^z = 2\hat{f}_l^\dagger \hat{f}_l - 1, \;\; \hat{\sigma}_l^- = \hat{f}_l e^{-i\pi \sum_{m<l} \hat{n}_m}, \;\; \hat{\sigma}_l^+ = \hat{f}_l^\dagger e^{i\pi \sum_{m<l} \hat{n}_m}, \tag{1.5}$$

where $\hat{f}_l$ are fermionic operators.

The same is also true for few spinless bosons in an optical lattice of any dimension when $U_\sigma \to \infty$, which then means double occupation of a site is essentially forbidden, with $(\hat{b}_i^\dagger)^2 = 0$. We can then obtain a spin system by applying the following mapping to Eq. (1.3)

$$\hat{\sigma}_i^z = 2\hat{b}_i^\dagger \hat{b}_i - 1, \;\; \hat{\sigma}_i^- = \hat{b}_i, \;\; \hat{\sigma}_i^+ = \hat{b}_i^\dagger, \tag{1.6}$$

where $\hat{b}_i$ are bosonic operators. Bosonic excitations with $(\hat{b}_i^\dagger)^2 = 0$ are known as Hardcore bosons. Finally, spin models can also be achieved with spinless bosons in tilted optical lattices [17, 18].

### 1.1.2 Internal Degrees of Freedom

As well as through motional degrees of freedom, spin models arise naturally when particles interact purely through their internal degrees of freedom, such as electronic or hyperfine energy levels. Typically, the internal energy levels of particles interact through exchange of photons which couple to the dipole moment of the internal energy transition. In situations where the time scales set by the interactions are much faster

than the motional degrees of freedom, we can safely ignore any motional effects and treat the particles as if they are at fixed positions. For example, such a set up is possible in ultracold gases when the lattice potential is so large that $h_\sigma \approx 0$ and no particle hopping can occur. When only two internal states are relevant for the inter-particle interactions, the dynamics again map to spin-1/2 system, although including more internal states allows higher spin models to be achieved.

Through appropriate choice of the internal degrees of freedom, it is possible to tune a variety of spin interactions. As in the previous section, we will primarily focus on generic spin models of the type

$$\hat{H} = \sum_i^N \Delta_i^z \hat{\sigma}_i^z + \sum_i^N \Delta_i^x \hat{\sigma}_i^x + \sum_i^N \Delta_i^y \hat{\sigma}_i^y + \sum_{i,l}^N J_{il}^z \hat{\sigma}_i^z \hat{\sigma}_l^z + J_{il}^x \hat{\sigma}_i^x \hat{\sigma}_l^x + J_{il}^y \hat{\sigma}_i^y \hat{\sigma}_l^y, \tag{1.7}$$

where the quantities $\Delta^{x,y,z}$ are set by external drives and the interactions $J^{x,y,z}$ are set by the coupling of dipole moments between the two-level systems. The spin operators are now defined by the two energy levels involved,

$$\begin{aligned}
\hat{\sigma}_l^z &= |e_l\rangle \langle e_l| - |g_l\rangle \langle g_l|, \\
\hat{\sigma}_l^+ &= |e_l\rangle \langle g_l|, \\
\hat{\sigma}_l^- &= |g_l\rangle \langle e_l|, \\
\hat{\sigma}_l^x &= \hat{\sigma}_l^- + \hat{\sigma}_l^+, \\
\hat{\sigma}_l^y &= i\hat{\sigma}_l^- - i\hat{\sigma}_l^+,
\end{aligned} \tag{1.8}$$

where $|e_l\rangle$ is the excited energy level and $|g_l\rangle$ is the groundstate energy level of a particle on site $l$. Throughout this thesis, the appearance of the Pauli operators will occur often and will always obey these definitions unless stated otherwise. Also note that throughout this thesis, we will work with the convention that $\hbar = 1$.

For cold gases, spin systems can be implemented with the internal triplet states of alkaline-earth atoms such as Sr [19–21], or rotational energy levels of polar molecules such as KRb [22–24]. It is also possible to construct spin models with the electronic energy levels of Rydberg atoms, atoms which have their outermost electron excited to very high quantum numbers, inheriting very strong dipole moments as a consequence [25–30]. Engineering spin interactions through trapped particle degrees of freedom is also possible in a variety of different systems other than ultracold gases [31]. It is possible to engineer Hamiltonians of the form in Eq. (1.7) through trapped ions, where ions can be constrained using microtraps and then laser cooled [32, 33] and also

through coupled cavities, where atoms are trapped inside cavities which can be then arranged in periodic arrays [34, 35]. Further implementations are superconducting circuits, where the two-level system is formed of energy levels of an LC circuit with a Josephson junction [36, 37] and nuclear spins in Nitrogen vacancy (NV) centres [38–40]. Spin systems with motional degrees of freedom are also possible in other systems such as in arrays of quantum dots, where electrons are confined to discrete energy levels in semiconductor wells and form spin interactions via superexchange [41, 42].

While we have discussed both motional and internal degrees of freedom to construct spin models, we will only consider fixed particles interacting through their energy levels by dipole interactions from now on. The experimental focus will be on cold atoms and molecules, but the references in this chapter demonstrate that many of the models we consider in this thesis can be implemented in a variety of different ways.

## 1.2 Non-Equilibrium Phenomena

One major interest in quantum simulation is studying systems consisting of a macroscopic number of degrees of freedom, which can present interesting forms of collective behaviour, notably the existence of different phases of matter at thermal equilibrium. Much work is currently focused on macroscopic quantum systems in far-from-equilibrium settings [10] which are now possible to study experimentally in ultracold atomic gases [43, 44]. In closed quantum systems (systems that do not interact with an external environment), it is expected that interactions will lead to a redistribution of energy among all degrees of freedom, resulting in thermalisation at long times. This allows the system to be described in terms of only a few key macroscopic quantities rather than having to know the full details of the underlying microscopic dynamics. The thermalisation of quantum systems is usually expected due to the eigenstate thermalisation hypothesis, which postulates that the eigenstates of generic quantum systems inherently contain a thermal state and this thermal state is eventually revealed in the long-time limit under standard unitary evolution [45]. However, it is known that thermalisation of a quantum system need not always occur. Instead, there can be regimes of synchronization, where coherent dynamics persist, many-body localization, where quantum states are prevented from thermalisation due to disorder in the system, or prethermalisation, where the system appears to thermalise in the long-time limit, before undergoing further dynamics and reaching true thermal equilibrium at a later

time [46–49]. Determining under what conditions a system does not thermalise and the form of non-equilibrium phenomena that can exist is an active area of current research.

Interactions between atoms and molecules are crucial for thermalisation phenomena. For example, given a system of isolated two-level systems under an external drive, there is no mechanism for energy to be transferred between degrees of freedom and so we expect the system to not thermalise and instead for the two-level system to undergo persistent Rabi oscillations. However, interactions between the two-level systems leads to (local) energy shifts of the resonance frequency. Consequently, when driven out of equilibrium, the interactions are expected to lead to dephasing of collective Rabi oscillation [50–56] causing observables to relax to some (non-equilibrium) steady state values. In some systems, even with the presence of interactions, a system will not thermalise due to there being as many conserved quantities as degrees of freedom. Such systems are known as integrable [57].

As well as through interactions, far-from-equilibrium behaviour also naturally arises when systems are subject to noise from an external environment, which causes decoherence of quantum effects. This can lead to new phases of matter not found in isolated systems and also alter phase transitions that occur in closed systems. Simulating and studying the steady state behaviour of open quantum systems is a very active area of research [58–60], as exploiting the presence of an environment is useful, especially in experiments involving optical transitions where environmental effects are hard to remove. We will give a proper introduction to open quantum systems and the effects of an environment in the next chapter.

Finally, in addition to looking at the long-time dynamics and steady states of a system, it is also interesting to study transient non-equilibrium phenomena by studying the dynamics and decay of excitations within a system. With strongly coupled two-level quantum systems, it is possible to explore fundamental issues in the quantum dynamics of many-body systems subject to strong interparticle interactions [61–63]. An example we will look into is that of magnon dynamics, including magnon bound states, where two excitations in a quantum system can bind together and travel as a single unit.

## 1.3 Dipole Interactions

As mentioned earlier, interactions between fixed particles typically occur due to their dipole moments. We will therefore be focusing on dipole-dipole interactions between two-level systems in this thesis. This is one of the simplest physical realisations which

explores the far-from-equilibrium dynamics of many interacting quantum degrees of freedom. Dipole interactions can be long-ranged and dissipative, and arise naturally in many systems, such as ultracold polar molecules, polarisable ultracold atoms and Rydberg atoms. The range and form of the dipole interactions depends on the wavelength of the energy level transition between the internal states chosen. We shall look at both the case of near-field dipole interactions, which are short-ranged, and also far-field dipole interactions, which are long-ranged and dissipative. The different forms of the dipole interactions can have large differences on the resultant non-equilibrium phenomena.

### 1.3.1 Near-field Dipole Interactions

When the two-level transition wavelength is large compared to the distance between the particles, then the interactions between the internal states are described by a near-field dipole interaction of the form

$$\hat{H}_{Dip} = \sum_{\substack{i,l \\ i \neq l}}^{N} \frac{J_0}{r_{il}^3} \left[ \hat{\mathbf{d}}_i \cdot \hat{\mathbf{d}}_l - \frac{3(\hat{\mathbf{d}}_i \cdot \mathbf{r}_{il})(\hat{\mathbf{d}}_l \cdot \mathbf{r}_{il})}{r_{il}^2} \right], \tag{1.9}$$

where $\mathbf{r}_{il} = \mathbf{r}_i - \mathbf{r}_l$, with $\mathbf{r}_i$ being the position vector of a dipole on site $i$, $r_{il} = |\mathbf{r}_{il}|$, $\hat{\mathbf{d}}_i$ is the dipole moment operator on site $i$ and $J_0 = 1/4\pi\epsilon_0$ for electric dipoles or $J_0 = \mu_0/4\pi$ for magnetic dipoles. The spatial profile of the near-field dipole interactions is $1/r^3$, which means the boundary of the system will be important in 3D, but not important in 2D or 1D systems. Near-field dipole interactions occur when the wavelength of the two-level transition is typically in the microwave regime, which is common when working with rotational levels in polar molecules, such as KRb or with highly excited electronic states in Rydberg atoms. Both polar molecules and Rydberg atoms typically have both exchange and static dipole interactions. For the case of two energy levels, we can choose the quantisation of the dipole along the $z$ axis [64] and then have the static dipole terms, $d_0 = \langle g | d^z | g \rangle$, $d_1 = \langle e | d^z | e \rangle$, and also the transfer dipole term, $q_1 = |\langle g | d^z | e \rangle| = |\langle e | d^z | g \rangle|$, transforming the Hamiltonian in Eq. (1.9) into the following spin Hamiltonian

$$H_{Dip} = \sum_{\substack{i,l \\ i \neq l}}^{N} \frac{J_0}{r_{il}^3} \left( \frac{(d_1 - d_0)^2}{4} \hat{\sigma}_i^z \hat{\sigma}_l^z + q_1^2 (\hat{\sigma}_i^+ \hat{\sigma}_l^- + \hat{\sigma}_i^- \hat{\sigma}_l^+) + \frac{d_1^2 - d_0^2}{4} (\hat{\sigma}_i^z + \hat{\sigma}_l^z) + \frac{(d_1 + d_0)^2}{4} \right). \tag{1.10}$$

We can see here how the static dipole moment results in an Ising interaction while the exchange dipole moment results in an XY interaction. This type of Hamiltonian will appear in Chapters 3 and 4.

Many experiments have already been performed to realise isolated dipole coupled spin systems, where Rydberg atoms [65–68] have been used to realise XY models and Ising like models, as well as allow storage and read out of photons. There is also considerable progress using polar molecules to realise quantum magnetism [22, 23, 69–71]. There are numerous novel theoretical predictions for the behaviour of near-field dipole coupled spins. These include work showing how the $1/r^3$ nature of dipole interactions can stabilise Bose Einstein condensates against fluctuations and disorder [72], as well as lead to interesting topological properties of the groundstate of the Hamiltonian [64] and the role of dipole interactions in spin ice [73]. There are also many studies on the role of near-field dipole interactions in magnetic materials [74].

### 1.3.2 Far-Field Dipole Interactions

When the two-level transition wavelength is comparable to or smaller than the distance between the particles, the interactions between the internal states are then described by a far-field dipole interaction of the form

$$\begin{aligned}\hat{H}_{Dip} = -\frac{\kappa^3}{4\pi\epsilon_0}\sum_{\substack{i,l\\ i\neq l}}^{N} e^{i\kappa r_{il}}\Bigg\{ &\left[\hat{\mathbf{d}}_i\cdot\hat{\mathbf{d}}_l - \frac{(\hat{\mathbf{d}}_i\cdot\mathbf{r}_{il})(\hat{\mathbf{d}}_l\cdot\mathbf{r}_{il})}{r_{il}^2}\right]\frac{1}{\kappa r_{il}}\\ &+\left[\hat{\mathbf{d}}_i\cdot\hat{\mathbf{d}}_l - \frac{3(\hat{\mathbf{d}}_i\cdot\mathbf{r}_{il})(\hat{\mathbf{d}}_l\cdot\mathbf{r}_{il})}{r_{il}^2}\right]\left(\frac{i}{(\kappa r_{il})^2}-\frac{1}{(\kappa r_{il})^3}\right)\Bigg\},\end{aligned} \tag{1.11}$$

where $\kappa = 2\pi/\lambda_d$, with $\lambda_d$ being the wavelength of the dipole transition. In this regime, the spatial profile of the dipole interaction is long-ranged, with $1/r$ and $1/r^2$ terms as well as the $1/r^3$ form from the near-field case. The long-range nature of the interaction can have significant effects on the quantum system, especially the $1/r$ terms, which means the boundary of the system is important even in one dimensional systems. The interaction has real and imaginary parts, where the imaginary parts of the field correspond to loss into the environment and will play an important part of the dynamics. Note that in the limit $\kappa \to 0$, we regain the near-field dipole interaction in Eq. (1.9) as expected.

Far-field dipole interactions occur in polarisable atoms, rather than polar molecules and Rydberg atoms. For these systems, the wavelength of transition is in the optical

regime. We also lose the static dipole moment, as atoms have weak or non-existent permanent dipole moments. The interaction of an electromagnetic wave with a medium formed from an array of polarisable particles is a recurring problem in physics. If these particles are two-level quantum systems driven close to resonance, then collective effects can arise due to the strong resonant dipole-dipole interactions provided the average interparticle spacing is smaller than the dipolar transition wavelength. These collective effects give significant deviations in the behaviour of the medium compared to one formed of non-interacting scatterers. Key differences include the emergence of Lamb shifts, where interactions modify the two-level transition energies [75, 76], and the formation of superradiant and subradiant modes, where the dipole-dipole interactions enhance or suppress decay of excitations [77, 78]. Understanding how these collective effects alter the response of a medium is still an ongoing topic of research.

Because the transition wavelength is in the optical regime, dipole interactions of the form in Eq. (1.11) are very important in understanding how light scatters through cold disordered atomic gas clouds due to the large scale collective effects that can arise. Much work has already been carried out on theoretically understanding light scattering through cold atom gases [79–84], with some of these effects being realised experimentally [85–88]. Most work focuses on the low light intensity limit, where interactions between excitations is negligible and the full quantum model simplifies to a problem of classical scatterers. In these models, the collective effects can be exploited, especially when the atoms are arranged periodically on a lattice [89]. This can lead to effects such as electromagnetically induced transparency interferences [90, 91], long-time excitation storage in subradiant modes [92] and enhanced optical cross sections [93].

## 1.4 Outline of Thesis

The outline of this thesis is as follows. In Chapter 2, we introduce the theory of open quantum systems, when the atoms interact with a common environment, which will be required for later chapters on dissipative systems. In Chapter 3, we study a closed system of two-level systems with near-field static and exchange dipole interactions under an external drive, finding regimes of collective Rabi oscillations despite the presence of interactions. In Chapter 4, we look at the same near-field dipole system from Chapter 3, but now coupled to an environment, which induces local dissipation and causes the excitations to decay. We find the presence of an environment leads to a

range of new non-equilibrium phenomena. Then in Chapter 5, we focus on far-field dipole interactions, which introduces nonlocal dissipation to the system and changes the non-equilibrium phases that arise due to the coupling of several decay modes into the environment. In Chapter 6, we study the dynamics of excitations in dipole coupled systems on the approach to the steady state, looking at two-excitation bound states and how the presence of nonlocal dissipation effects their dynamics. Finally, in Chapter 7, we draw conclusions and also outline future work.

# Chapter 2

# Open Quantum Systems

## 2.1 Introduction

In nearly all experimental settings, a system cannot be perfectly isolated from its environment. Instead, interactions can cause decay of excitations and dephasing of the system and, in many cases, can have significant impact on the resultant dynamics and phases. In this chapter, we introduce how to handle the effects of an environment by using the theory of open quantum systems [94], which will be important in later chapters.

## 2.2 Master Equation Derivation

When a system interacts with an environment, it is useful to consider the system of interest and the environment together as one large isolated system. Then, one separates the system Hamiltonian into a bath Hamiltonian, $\hat{H}_B$, containing all unwanted degrees of freedom, the system Hamiltonian, $\hat{H}_S$, containing all the degrees of freedom of interest, and the interaction between the two, $\hat{H}_I$, such that

$$\hat{H} = \hat{H}_S + \hat{H}_B + \hat{H}_I. \tag{2.1}$$

To describe the dynamics of the system, it is convenient to work with the density matrix, defined as $\hat{\rho}(t) = |\psi(t)\rangle \langle\psi(t)|$, where $|\psi(t)\rangle$ is the wavefunction of the system. The density matrix has the property $\mathrm{Tr}\{\hat{\rho}(t)\} = 1$ due to unitarity, and any observable of the system is given by $\langle\hat{O}\rangle = \mathrm{Tr}\Big\{\hat{\rho}(t)\hat{O}\Big\}$, where $\hat{O}$ is some generic operator. The dynamics of the full system (system, bath and interaction) still obey the Schrödinger

equation. Therefore, the density matrix of the full system obeys

$$\frac{d\hat{\rho}(t)}{dt} = -i\left[\hat{H}_I + \hat{H}_S + \hat{H}_B, \hat{\rho}(t)\right]. \tag{2.2}$$

We wish to focus on the dynamics of just the system and its interaction with the environment, rather than trying to simulate the full system dynamics, which is generally impossible. Therefore, to proceed, we will need to develop an effective model of the environmental degrees of freedom. To do this, we first write Eq. (2.2) in the interaction picture by applying the unitary transform $\hat{U}(t,0) = \exp\Big(-it(\hat{H}_S + \hat{H}_B)\Big)$ to Eq. (2.2), which gives

$$\frac{d\hat{R}(t)}{dt} = -i\left[\hat{H}_I(t), \hat{R}(t)\right], \tag{2.3}$$

where the interaction picture density matrix is given by $\hat{R}(t) = e^{it(\hat{H}_S+\hat{H}_B)}\hat{\rho}(t)e^{-it(\hat{H}_S+\hat{H}_B)}$ and the interaction picture Hamiltonian defined by $\hat{H}_I(t) = e^{it(\hat{H}_S+\hat{H}_B)}\hat{H}_I e^{-it(\hat{H}_S+\hat{H}_B)}$. We now integrate Eq. (2.3) to obtain an expression for $\hat{R}(t)$ and then substitute this expression back into Eq. (2.3). By tracing out the environmental degrees of freedom, we define the reduced density matrix, $\hat{R}_S(t) = \mathrm{Tr}_B\{\hat{R}(t)\}$, which obeys

$$\frac{d\hat{R}_S(t)}{dt} = -\int_0^t ds\, \mathrm{Tr}_B\left\{\left[\hat{H}_I(t), \left[\hat{H}_I(s), \hat{R}(s)\right]\right]\right\}, \tag{2.4}$$

assuming that $\mathrm{Tr}_B\left\{\left[\hat{H}_I(t), \hat{R}(0)\right]\right\} = 0$ so there is no constant of integration. The dynamics of the reduced density matrix still depend on full density matrix $\hat{R}(t)$. Therefore, to simplify the dynamics, we follow the steps taken in Ref. [94]. Firstly, we apply the Born approximation, which involves assuming that the coupling between the system and the environment is weak, so that changes in the system have only a small effect on the environment. This allows us to write $\hat{R}(t) \approx \hat{R}_S(t) \otimes \hat{R}_B$. Furthermore, we have to assume that the environment has no memory effects, known as the Markov approximation, which means the dynamics of the density matrix do not depend on its previous state. This allows us to replace $\hat{R}(s)$ with $\hat{R}(t)$ in the integral equation, Eq. (2.4) and, with a subsequent relabelling of $s \to t - s$, change the upper limit of the integral to infinity. With these approximations, we can now write Eq. (2.4) as

$$\frac{d\hat{R}_S(t)}{dt} = -\int_0^\infty ds\, \mathrm{Tr}_B\left\{\left[\hat{H}_I(t), \left[\hat{H}_I(t-s), \hat{R}_S(t) \otimes \hat{R}_B\right]\right]\right\}. \tag{2.5}$$

To simplify the dynamics further, we now apply the Secular approximation, which first involves rewriting the interaction Hamiltonian in the basis of system Hamiltonian eigenstates. In the Schrödinger picture, the interaction Hamiltonian can be written in the following form

$$\hat{H}_I = \sum_\alpha \hat{A}_\alpha \otimes \hat{B}_\alpha, \tag{2.6}$$

where $\hat{A}_\alpha$ and $\hat{B}_\alpha$ are arbitrary Hermitian operators, where $\hat{A}_\alpha$ acts on the system and $\hat{B}_\alpha$ acts on the environment. We now introduce the operators

$$\hat{A}_\alpha(\omega) \equiv \sum_{\epsilon-\epsilon'=\omega} \hat{\Pi}(\epsilon)\hat{A}_\alpha\hat{\Pi}(\epsilon'), \tag{2.7}$$

where $\epsilon$ and $\epsilon'$ are eigenvalues of the system and $\hat{\Pi}(\epsilon)$ is a projector onto the eigenvector(s) of the eigenvalue $\epsilon$. The sum is over a finite bandwidth where the difference between energies satisfies $\epsilon - \epsilon' = \omega$. The operators $\hat{A}(\omega)$ obey the relations $[\hat{H}_S, \hat{A}_\alpha(\omega)] = -\omega\hat{A}_\alpha(\omega)$ and $[\hat{H}_S, \hat{A}^\dagger_\alpha(\omega)] = \omega\hat{A}^\dagger_\alpha(\omega)$. They also obey a completeness relation $\sum_\omega A_\alpha(\omega) = \sum_\omega A^\dagger_\alpha(\omega) = A_\alpha$ which allows us to write the interaction Hamiltonian as

$$\hat{H}_I = \sum_{\alpha,\omega} \hat{A}_\alpha(\omega) \otimes \hat{B}_\alpha = \sum_{\alpha,\omega} \hat{A}_\alpha(\omega)^\dagger \otimes \hat{B}^\dagger_\alpha. \tag{2.8}$$

In the interaction picture, the interaction Hamiltonian is then given by

$$\hat{H}_I(t) = \sum_{\alpha,\omega} e^{-i\omega t}\hat{A}_\alpha(\omega) \otimes \hat{B}_\alpha(t) = \sum_{\alpha,\omega} e^{i\omega t}\hat{A}_\alpha(\omega)^\dagger \otimes \hat{B}_\alpha(t)^\dagger, \tag{2.9}$$

where $\hat{B}_\alpha(t) = e^{i\hat{H}_B t}\hat{B}_\alpha e^{-i\hat{H}_B t}$. Inserting the interaction Hamiltonian into Eq. (2.5) gives

$$\begin{aligned}\frac{d\hat{R}_S(t)}{dt} &= -\int_0^\infty \mathrm{Tr}_B\left\{\hat{H}_I(t-s)\hat{R}_S(t)\otimes\hat{R}_B\hat{H}_I(t) - \hat{H}_I(t)\hat{H}_I(t-s)\hat{R}_S(t)\otimes\hat{R}_B\right\} + h.c. \\ &= \sum_{\omega\omega'}\sum_{\alpha\beta} e^{i(\omega-\omega')t}G_{\alpha\beta}(\omega)\left[\hat{A}_\beta(\omega)\hat{R}_S(t)\hat{A}^\dagger_\alpha(\omega') - \hat{A}^\dagger_\alpha(\omega')\hat{A}_\beta(\omega)\hat{R}_S(t)\right] + h.c.,\end{aligned} \tag{2.10}$$

where *h.c.* denotes the hermitian conjugate. The quantities $G_{\alpha\beta}$ are defined as

$$G_{\alpha\beta}(\omega) = \int_0^\infty \mathrm{Tr}_B\left\{\hat{B}^\dagger_\alpha(t)\hat{B}_\beta(t-s)\hat{R}_B\right\}e^{i\omega s}ds. \tag{2.11}$$

The terms of $\omega \neq \omega'$ in the sum of Eq. (2.10) can be ignored if they oscillate much faster than the inverse of the relaxation time of the system, $\tau_R$. Therefore, we only include the terms with $\omega = \omega'$ in the sum. Finally, splitting the function $G_{\alpha\beta} = \Gamma_{\alpha\beta}/2 + iS_{\alpha\beta}$ into real and imaginary parts gives

$$\begin{aligned}\frac{d\hat{\rho}_S(t)}{dt} &= -i\left[\hat{H}_S + \sum_{\omega}\sum_{\alpha\beta} S_{\alpha\beta}\hat{A}^{\dagger}_{\alpha}(\omega)\hat{A}_{\beta}(\omega), \hat{\rho}_S(t)\right] \\ &+ \sum_{\omega}\sum_{\alpha\beta}\frac{\Gamma_{\alpha\beta}}{2}(2\hat{A}_{\beta}(\omega)\hat{\rho}_S(t)\hat{A}^{\dagger}_{\alpha}(\omega) - \hat{A}^{\dagger}_{\alpha}(\omega)\hat{A}_{\beta}(\omega)\hat{\rho}_S(t) - \hat{\rho}_S(t)\hat{A}^{\dagger}_{\alpha}(\omega)\hat{A}_{\beta}(\omega)),\end{aligned} \tag{2.12}$$

where we have moved back to the Schrödinger picture. This is the master equation which describes the dynamics of the reduced density matrix of the system. The expression in the commutators represents unitary evolution under the Hamiltonian whilst the second term is the loss terms from interaction with the environment. In general, for the Markovian approximation to be valid, we require the reservoir correlation functions in Eq. (2.12) to decay much faster than the relaxation time $\tau_R$. If the environment density matrix $\hat{\rho}_B$ is a stationary state of the bath i.e. $[\hat{H}_B, \hat{\rho}_B] = 0$, then the quantities $G_{\alpha\beta}$ are independent of $t$, which will be assumed in future chapters.

## 2.3 Adjoint Equation

As for closed system quantum dynamics, it is sometimes useful to consider the evolution of the system from the perspective of the Heisenberg picture, looking at the dynamics of the operators rather than the density matrix. To do this, let us take the master equation, Eq. (2.12) and rewrite it using the Liouvillian superoperator $\hat{\mathcal{L}}$, which acts on an operator, $\hat{O}$, as follows

$$\begin{aligned}\hat{\mathcal{L}}\hat{O} &= -i\left[\hat{H}_S + \sum_{\omega}\sum_{\alpha\beta} S_{\alpha\beta}\hat{A}^{\dagger}_{\alpha}(\omega)\hat{A}_{\beta}(\omega), \hat{O}\right] \\ &+ \sum_{\omega}\sum_{\alpha\beta}\frac{\Gamma_{\alpha\beta}}{2}\left(2\hat{A}_{\beta}(\omega)\hat{O}\hat{A}^{\dagger}_{\alpha}(\omega) - \{\hat{A}^{\dagger}_{\alpha}(\omega)\hat{A}_{\beta}(\omega), \hat{O}\}\right),\end{aligned} \tag{2.13}$$

where the curly brackets denote the anti-commutator. The master equation, Eq. (2.12), can be written as $d\hat{\rho}(t)/dt = \hat{\mathcal{L}}\hat{\rho}(t)$. By introducing the propagator $\hat{V}(t, t_0) = T_{\rightarrow}\exp\left(\int_{t_0}^{t}\hat{\mathcal{L}}dt\right)$, the dynamical evolution of the open quantum system can be written

as

$$\hat{\rho}_S(t) = \hat{V}(t,t_0)\hat{\rho}_S(t_0), \tag{2.14}$$

where time ordering has been applied to $\hat{V}(t,t_0)$, denoted by $T_{\rightarrow}$. Any observable in the open quantum system is given by $\mathrm{Tr}_S\left\{\hat{O}\hat{V}(t,t_0)\hat{\rho}_S(t_0)\right\}$ which can be rewritten as $\mathrm{Tr}_S\left\{\hat{V}^\dagger(t,t_0)\hat{O}\hat{\rho}_S(t_0)\right\}$. This motivates the introduction of the Heisenberg operator as $\hat{O}_H(t) = \hat{V}^\dagger(t,t_0)\hat{O}$ where $\hat{V}^\dagger(t,t_0) = T_{\leftarrow}\exp\left(\int_{t_0}^{t}\hat{\mathcal{L}}^\dagger dt\right)$, and $T_{\leftarrow}$ denotes anti-chronological time ordering. The equation of motion for the Heisenberg operator is now given as

$$\frac{d\hat{O}_H(t)}{dt} = \hat{V}^\dagger(t,t_0)\hat{\mathcal{L}}^\dagger\hat{O}. \tag{2.15}$$

If the Liouvillian superoperator is time independent, then $\hat{V}^\dagger(t,t_0)$ and $\hat{\mathcal{L}}^\dagger$ commute. This means Eq. (2.15) can be written as $d\hat{O}_H(t)/dt = \hat{\mathcal{L}}^\dagger\hat{O}_H(t)$, which can be fully expanded to give the adjoint master equation,

$$\frac{d\hat{O}_H(t)}{dt} = i\left[\hat{H},\hat{O}_H(t)\right] + \sum_{\omega}\sum_{\alpha\beta}\frac{\Gamma_{\alpha\beta}}{2}\left(2\hat{A}^\dagger_\alpha(\omega)\hat{O}_H(t)\hat{A}_\beta(\omega) - \{\hat{A}^\dagger_\alpha(\omega)\hat{A}_\beta(\omega),\hat{O}_H(t)\}\right). \tag{2.16}$$

The adjoint master equation can be more convenient to study than the master equation in determining the dynamics of observables.

## 2.4 Single Two-Level System in an Electromagnetic Environment

In order to demonstrate some key properties of dissipative systems, we will now study a simple model of a two-level system interacting with an electromagnetic bath. This will form the basis for future chapters when considering several two-level systems interacting with each other and an electromagnetic environment. The system Hamiltonian is given by

$$\hat{H}_S = \frac{\omega_0}{2}\hat{\sigma}^z, \tag{2.17}$$

where $\omega_0$ is the frequency of the two-level transition, and the bath Hamiltonian is given by harmonic oscillators for each mode of the electromagnetic field,

$$\hat{H}_B = \sum_{\mathbf{k}}\sum_{\nu=1,2}\omega_{\mathbf{k}}\hat{a}^\dagger_\nu(\mathbf{k})\hat{a}_\nu(\mathbf{k}), \tag{2.18}$$

where $\mathbf{k}$ is the wavevector of the mode, $\omega_{\mathbf{k}} = c|\mathbf{k}|$ is the frequency of the mode and $\hat{a}_\nu$, $\hat{a}_\nu^\dagger$ are the bosonic annihilation and creation operators of a mode with a polarisation indexed by $\nu$. The interaction Hamiltonian is given by

$$\hat{H}_I = -\hat{\mathbf{d}}.\hat{\mathbf{E}}, \tag{2.19}$$

where $\hat{\mathbf{d}}$ is the dipole operator of the two-level system. The operator $\hat{\mathbf{E}}$ is the electric field, given by

$$\hat{\mathbf{E}} = i\sum_{\mathbf{k}}\sum_{\nu=1,2}\sqrt{\frac{\omega_{\mathbf{k}}}{V\epsilon_0}}\mathbf{e}_\nu(\mathbf{k})\left(\hat{a}_\nu(\mathbf{k}) - \hat{a}_\nu^\dagger(\mathbf{k})\right), \tag{2.20}$$

where $V$ is the volume of space within which the radiation field is quantised and $\mathbf{e}_\nu(\mathbf{k})$ is the transverse polarisation unit vector. Given our system Hamiltonian, we can see that the eigenvectors of the system are simply $|g\rangle$ and $|e\rangle$. The interaction Hamiltonian is already in the form of Eq. (2.6), so we can write down the operators $\hat{A}_\alpha(\omega_0)$ as $\hat{A}_\alpha(\omega_0) = \langle e|\,\hat{\mathbf{d}}_\alpha\,|g\rangle\,\hat{\sigma}^-$ where $\alpha$ labels the Cartesian components, $x$, $y$ and $z$. The functions $G_{\alpha\beta}$ are defined by the electric field and given by $G_{\alpha\beta} = \int_0^\infty \langle \hat{\mathbf{E}}_\alpha(t)\hat{\mathbf{E}}_\beta(t-s)\rangle e^{i\omega_0 s}ds$. For a bath at zero temperature, we can evaluate the integral in $G_{\alpha\beta}$ (full details are given in [94]) to obtain $G_{\alpha\beta}(\omega_0) = \delta_{\alpha\beta}(\Gamma(\omega_0)/2 + iS(\omega_0))$ where

$$\Gamma(\omega_0) = \frac{\omega_0^3|\mathbf{d}|^2}{3\pi c^3\epsilon_0} = \frac{\kappa^3|\mathbf{d}|^2}{3\pi\epsilon_0}, \tag{2.21}$$

where $\kappa = 2\pi/\lambda_0$, with $\lambda_0$ being the wavelength of the two-level transition. This definition of $\Gamma$ will appear in future chapters. We ignore the form of $S(\omega_0)$ as this just results in a energy shift of the two-level system and can therefore be absorbed into the definition of $\omega_0$. The final master equation is given by

$$\frac{d\hat{\rho}(t)}{dt} = -i[\hat{H}_S, \hat{\rho}(t)] + \frac{\Gamma}{2}(2\hat{\sigma}^-\hat{\rho}(t)\hat{\sigma}^+ - \hat{\sigma}^+\hat{\sigma}^-\hat{\rho}(t) - \hat{\rho}(t)\hat{\sigma}^+\hat{\sigma}^-). \tag{2.22}$$

Note here that $\hat{\rho}(t)$ is the system density matrix, but we have dropped the $S$ subscript. Unless stated otherwise, we will adopt this convention for the rest of the thesis. We will also adopt the same convention for traces, which will now always be over the system degrees of freedom.

We can also add additional terms to our system Hamiltonian without changing the dissipation. Primarily, we will be concerned with driving the two-level transition with an external field, $\mathbf{E} = \boldsymbol{\epsilon}e^{-i\omega t} + \boldsymbol{\epsilon}^* e^{i\omega t}$, with $\boldsymbol{\epsilon}$ being the polarisation of the drive. This

external field will also couple to the dipole moment to give a new term of the form

$$\hat{H}_{Drive} = \frac{\Omega}{2}\hat{\sigma}^x, \tag{2.23}$$

where $\Omega = 2\boldsymbol{\epsilon} \cdot \mathbf{d}^*$. Note that we have made the rotating wave approximation in Eq. (2.23), which also shifts the energy of the system Hamiltonian so that $\omega_0 \to \Delta$ in Eq. (2.17) where $\Delta = \omega - \omega_0$.

To study the dynamics of the driven dissipative two-level system in more detail, we can derive the equations of motion for the spin by taking the trace $S^\beta(t) = \frac{1}{2}\,\mathrm{Tr}\{\hat{\sigma}^\beta \hat{\rho}(t)\}$ where $\beta = x, y, z$, which gives

$$\begin{aligned}
\frac{dS^x(t)}{dt} &= -\frac{\Gamma}{2}S^x(t) - \frac{\Delta}{2}S^y(t), \\
\frac{dS^y(t)}{dt} &= -\frac{\Gamma}{2}S^y(t) + \frac{\Delta}{2}S^x(t) - \Omega S^z(t), \\
\frac{dS^z(t)}{dt} &= -\Gamma\left(\frac{1}{2} + S^z(t)\right) + \Omega S^y(t).
\end{aligned} \tag{2.24}$$

These equations are known as the optical Bloch equations. In Fig. 2.1, we plot some example dynamics of the optical Bloch equations for an initial condition of $(S^x, S^y, S^z) = (0, 0, 1/2)$ with $\Gamma/\Omega = 0$ and $\Gamma/\Omega = 0.5$.

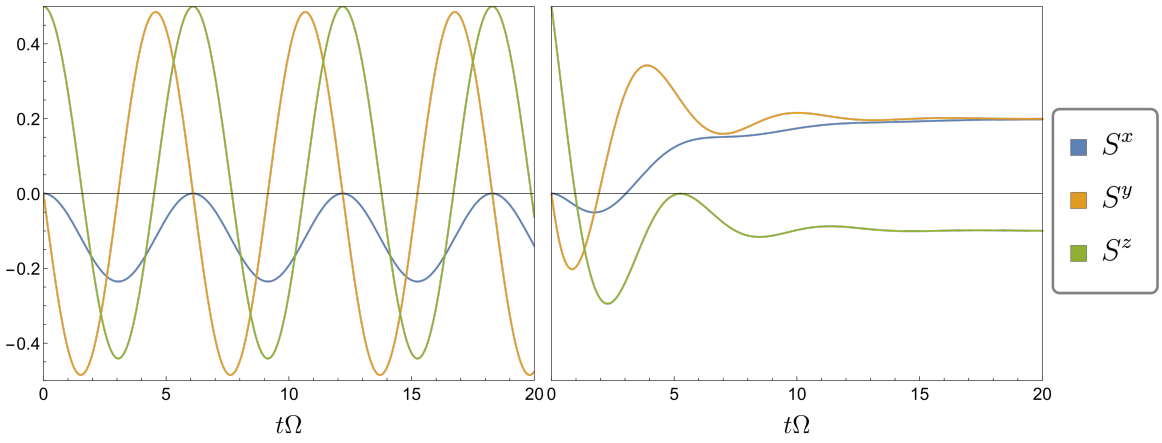


**Figure 2.1** Plot of the optical Bloch equations for $\Gamma/\Omega = 0$ (left) and $\Gamma/\Omega = 0.5$ (right) with $\Delta/\Omega = -0.5$. The presence of an environment drives the dynamics to a steady state at long times, whereas in a closed system, the dynamics would continuously oscillate due to the external drive.

The dynamics of the optical Bloch equations give examples of important changes due to the presence of an environment. For no dissipation, the system undergoes persistent Rabi oscillations, unless the initial condition is a steady state of the dynamics. However, introducing an environment causes the system to decay and results in the spin components always approaching a steady state, no matter how strong the drive or detuning. At low drive ($\Omega \approx 0$), this steady state is simply the groundstate of the system Hamiltonian, with $(S^x, S^y, S^z) = (0, 0, -1/2)$. However, at high drive, the solution is given by a mixed state with vanishing spin magnitude [95]. In later chapters, we will find examples of where we can recover oscillations even with dissipation when we include interactions between spin systems.

## 2.5 Superoperator Formalism

Finally, before moving to other chapters, it is worth discussing another convenient way to write the master Eq. (2.12). We mentioned in the discussion of the Adjoint master equation how the the Lindblad dynamics described by Eq. (2.12) can be written as a propagator acting on the density matrix. By working in a higher dimensional Hilbert space, we can rewrite this as a matrix equation by writing the density matrix in the superoperator formalism. This involves promoting the density matrix to a vector in Hilbert space of dimension $4^N$ and then the Lindblad master equation can be rewritten as a linear matrix equation of the form

$$\frac{d\boldsymbol{\rho}_S(t)}{dt} = \boldsymbol{\mathcal{L}}\boldsymbol{\rho}_S(t). \tag{2.25}$$

The $4^N \times 4^N$ matrix $\boldsymbol{\mathcal{L}}$ always has at least one zero eigenvalue, with the corresponding eigenvector being the steady state density matrix. All eigenvalues have zero or negative real part provided the master equation gives decay and the eigenvalues also come in complex conjugate pairs due to the Hermitian nature of $\hat{\rho}_S(t)$. In this form the time evolution is given by $\boldsymbol{\rho}_S(t) = \exp(\boldsymbol{\mathcal{L}}t)\boldsymbol{\rho}_S(0)$ which can be expanded in the eigenvalues of $\mathcal{L}$ to give

$$\boldsymbol{\rho}_S(t) = \sum_{i=0}^{4^N-1} c_i e^{\lambda_i t}\boldsymbol{R}_i, \tag{2.26}$$

where $c_i = \boldsymbol{L_i}.\boldsymbol{\rho}_S(0)$ and $\boldsymbol{L}_i$ and $\boldsymbol{R}_i$ are the left and right eigenvectors of $\boldsymbol{\mathcal{L}}$ which are distinct as $\boldsymbol{\mathcal{L}}$ is non-Hermitian.

Again, if we look at a single two-level system coupled to an electromagnetic field, we find the Liouvillian in superoperator form is given by

$$\boldsymbol{\mathcal{L}} = \begin{pmatrix} -\Gamma & -i\Omega & i\Omega & 0 \\ -i\Omega & \frac{\Gamma}{2} - 2i\Delta & 0 & i\Omega \\ i\Omega & 0 & \frac{\Gamma}{2} - 2i\Delta & -i\Omega \\ \Gamma & i\Omega & -i\Omega & 0 \end{pmatrix}. \tag{2.27}$$

There is a zero eigenvalue as expected, with the remaining eigenvalues, $\lambda$, given by solutions to the cubic

$$4\lambda^3 + 8\Gamma\lambda^2 + \left(5\Gamma^2 + 4\Delta^2 + 4\Omega^2\right)\lambda + \Gamma^3 + 4\Gamma\Delta^2 + 2\Gamma\Omega^2 = 0. \tag{2.28}$$

Using Descartes' rule sign we can explicitly see that all the eigenvalues must be negative or complex as there are no sign changes between coefficients and all coefficients are positive. More importantly, we can also see that there is never another zero eigenvalue, meaning there is only ever one steady state solution to the optical Bloch equations dynamics. Cases where there are two long-time steady states are referred to as bistabilities. An interesting quantity to study is the eigenvalue with the smallest real part which determines the approach to the steady state solution. In Fig. 2.2, we plot the smallest real part of the eigenvalues of the Liouvillian, also known as Liouvillian spectral gap.

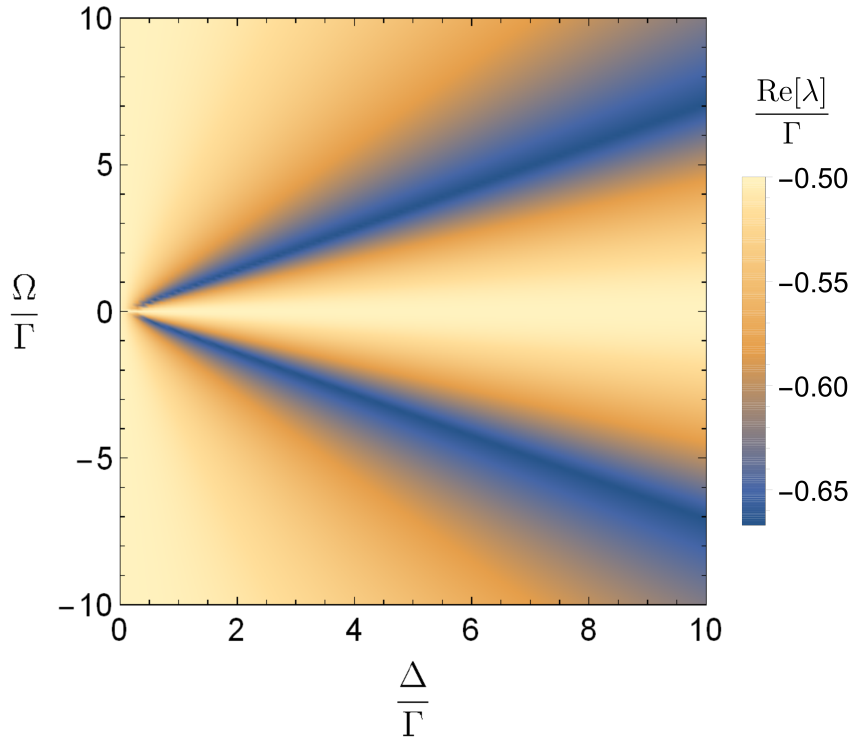


**Figure 2.2** Spectral gap of the Liouvillian for a single dissipative two-level system as a function of Rabi drive and detuning. We see the gap never decreases below $0.5\Gamma$ in magnitude, so there is only ever one steady state to the dynamics.

We see the gap never closes, and reaches a minimum of $0.5\Gamma$, so no bistability exists in a single spin coupled to an environment. In later chapters, we will look at examples where interacting spins have a gap smaller than $0.5\Gamma$ for certain $\Omega$ and $\Delta$, indicating that the gap could possibly close for large systems and that there could be more than one steady state.

# Chapter 3

# Stable collective dynamics of two-level systems coupled by dipole interactions

## 3.1 Introduction

In this chapter, we consider a closed system of a large number of two-level systems which are coupled by near-field dipole interactions and subjected to an external drive. After preparing the system out of equilibrium, we seek to find when collective coherent behaviour occurs, as a function of the strength of the external drive and also dependence on the form of the dipole-coupling (modified by the geometry, by the orientation of the dipoles, and by the relative strength of the static and transition dipole moments). Whereas the interactions give rise to chaotic behaviour and possible thermalisation in many cases, we show that there are parameter regimes where this no longer occurs and the system undergoes stable collective Rabi oscillations. By showing that stable collective oscillations can occur under an external drive, our work is complementary to that of Ref. [72] which considered the dynamics of non-equilibrium dipole-coupled two-level systems in a Ramsay sequence where the dynamics occur in the absence of any drive field.

This chapter is organised as follows. In Section 3.2 we define the model we study. We describe the resulting dynamical evolution in Section 3.3 as a function of the strength of the Rabi coupling. We focus first on a collective spin picture, §3.3.1, before proceeding to analyse when this collective picture breaks down, §3.3.2. In §3.3.3,

we study the high Rabi coupling limit analytically and show that in certain regimes collective Rabi oscillations are stable. The overall results are discussed in Section 3.4 and the conclusions are summarized in Section 3.5.

## 3.2 Model

We study the dynamics of $N$ two-level systems coupled by dipole interactions in a uniform external driving field, where $N$ is large. As mentioned in Chapter 1, such a system can be realised with atoms or polar molecules, held at fixed positions in an optical lattice, with the two levels being two internal energy levels between which there is a non-zero (magnetic or electric) dipole matrix element (e.g. these could be two rotational levels of a polar molecule). Representing each two-level system by a $S = 1/2$ spin, and working in the rotating wave approximation such that the drive field is time-independent, leads to the Hamiltonian

$$\hat{H} = \frac{\Omega}{2}\sum_{i}^{N}\hat{\sigma}_i^x + \sum_{\substack{i,l \\ i\neq l}}^{N}\frac{J_{il}}{4r_{il}^3}\left[\cos\alpha\hat{\sigma}_i^z\hat{\sigma}_l^z + \sin\alpha\left(\hat{\sigma}_i^y\hat{\sigma}_l^y + \hat{\sigma}_i^x\hat{\sigma}_l^x\right)\right], \tag{3.1}$$

where $\Omega$ is the Rabi coupling. We shall consider the positions of the two-level systems to be in 1D or 2D arrays, as specified by the couplings $J_{il}$. Here, $J_{il} = J_0a^3(1 - 3\cos^2\phi_{il}\sin^2\Theta)$, where $a$ is the lattice spacing, $\Theta$ represents the angle between the dipole orientation and the $z$ axis, and $\phi_{il}$ is the angle between dipoles in the $x-y$ plane (see Fig. 3.1). The parameter $J_0$ is given by $J_0 = 1/4\pi\epsilon_0$. For polar molecules, $\Theta$ can be tuned by application of a d.c. electric field along which the dipoles align [64]. The parameter $\alpha$ relates the relative strength of the Ising and XY dipole interactions and can take values between $-\pi$ to $\pi$. We focus only on the range $0 \leq \alpha < \pi$ as values below zero simply corresponds to a change in the sign of $J_0$ and give the same results. The value of $\alpha$ depends on the choice of internal states and external fields, with $\cos\alpha = (d_0 - d_1)^2$, where $d_0 = \langle g|\, d^z\, |g\rangle$ is the dipole moment of the groundstate, and $d_1 = \langle e|\, d^z\, |e\rangle$ is the dipole moment of the excited state. We also have $\sin\alpha = q_1^2$, where $q_1 = |\,\langle g|\, d^z\, |e\rangle\,| = |\,\langle e|\, d^z\, |g\rangle\,|$ is the exchange dipole moment [64]. One example of such a realisable set up involves the rotational states of polar molecules, the two levels being the ro-vibrational groundstate ($J = 0$) and one of the rotationally excited states ($J = 1, m_J = 0$). However, other states could also be chosen [22]. The dynamics of the system with no driving has already been studied [96–98]. The full model we

consider has been touched upon in [99], but that work does not consider the driven steady states that we identify here. Eq. (3.1) can also be mapped to a hardcore boson model [100].

We assume that all the two-level systems are initially in the groundstate, corresponding to all the spins lying along $(S^x, S^y, S^z) = (0, 0, -1/2)$. This initial state is not an eigenstate of Hamiltonian (3.1) and so the subsequent evolution involves far-from-equilibrium dynamics. Since we consider a macroscopic number of dipoles, an exact description of the dynamics is impossible. We make the approximation that the system behaves classically and quantum fluctuations are negligible. We expect this approximation to be valid in regimes where the two-level systems remain largely coherent – that is, with only long-range variations of the spin, such that there is a well-defined local spin and the system can be viewed as having slowly-varying ferromagnetic order. Indeed, we shall show that such situations of stable long-range coherence arise in certain parameter regimes.

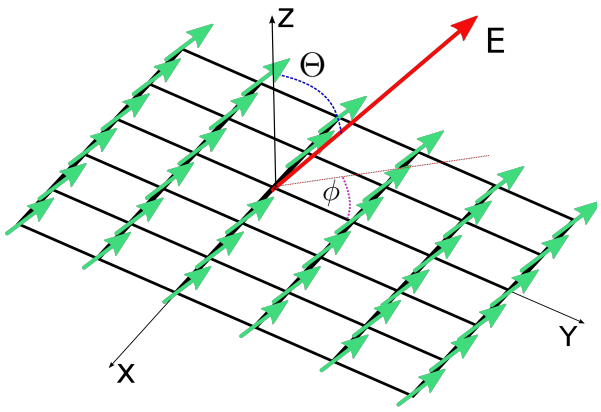


**Figure 3.1** A sketch of the considered geometry, with dipoles oriented at an angle $\Theta$ to a 2D lattice under an applied external field, **E**. $\phi$ is the 2D polar angle between dipoles.

## 3.3 Dynamical Evolution

In order to investigate the collective dynamics induced by Eq. (3.1), we solve numerically the Heisenberg equations of motion. For an exact quantum system, the number of equations of motion scales as $2^N$ where $N$ is the number of spins, making the problem intractable for large systems. However, in the classical approximation, we can ignore quantum correlations by factorizing $\langle \hat{S}_i^\alpha \hat{S}_l^\beta \rangle \approx \langle \hat{S}_i^\alpha \rangle \langle \hat{S}_l^\beta \rangle$, where $\hat{S}^\beta \equiv \frac{1}{2}\hat{\sigma}^\beta$ and $\beta$ takes

the values $x$, $y$ or $z$. The number of equations of motion then scales linearly with system size, and are given by

$$\begin{aligned}
\frac{dS_l^x}{dt} &= 2\sin\alpha \sum_{i(\neq l)}^{N} \frac{J_{il}}{r_{il}^3} S_l^z S_i^y - 2\cos\alpha \sum_{i(\neq l)}^{N} \frac{J_{il}}{r_{il}^3} S_i^z S_l^y, \\
\frac{dS_l^y}{dt} &= -\Omega S_l^z - 2\sin\alpha \sum_{i(\neq l)}^{N} \frac{J_{il}}{r_{il}^3} S_l^z S_i^x + 2\cos\alpha \sum_{i(\neq l)}^{N} \frac{J_{il}}{r_{il}^3} S_i^z S_l^x, \\
\frac{dS_l^z}{dt} &= \Omega S_l^y + 2\sin\alpha \sum_{i(\neq l)}^{N} \frac{J_{il}}{r_{il}^3} \left(S_i^y S_l^x - S_l^y S_i^x\right),
\end{aligned} \tag{3.2}$$

where $S_i^\beta \equiv \langle \hat{S}_i^\beta \rangle$. We impose periodic boundary conditions, which in the large $N$ limit approximate a system with open boundary conditions very well for 1D and 2D, as the boundary effects become negligible. This would not be the case in 3D (which we do not consider here), for which the choice of boundary remains important for the dynamics owing to the dipolar interactions.

Solving Eqs. (3.2) we find that the spins behave collectively if all prepared in the same initial state. We can therefore simplify the equations of motion and study the collective dynamics in more detail, before analysing the stability under perturbations.

### 3.3.1 Collective Dynamics

Treating the spins as a uniform collective spin, we set $S_i^\beta = S^\beta$ in Eqs. (3.2), and obtain a new set of equations valid on each lattice site

$$\begin{aligned}
\frac{dS^x}{dt} &= 2\tilde{\epsilon_0} S^z S^y, \\
\frac{dS^y}{dt} &= -\Omega S^z - 2\tilde{\epsilon_0} S^x S^z, \\
\frac{dS^z}{dt} &= \Omega S^y,
\end{aligned} \tag{3.3}$$

with $\tilde{\epsilon}_0 = (\sin\alpha - \cos\alpha)\sum_{i\neq 0}^{N} J_{i0}$ which is a measure of the dipole interaction strength, depending on the dipole tilt, underlying lattice and dimensionality. Fig. 3.2 shows the spin dynamics for the specific case of $\alpha = \pi/2$ and with the dipoles perpendicular to the lattice ($\Theta = 0$). We plot the orbit for an initial condition of $(S^x, S^y, S^z) = (0, 0, -1/2)$ in red (dashed line), and that for an initial condition of $(S^x, S^y, S^z) = (0, 0, +1/2)$ in

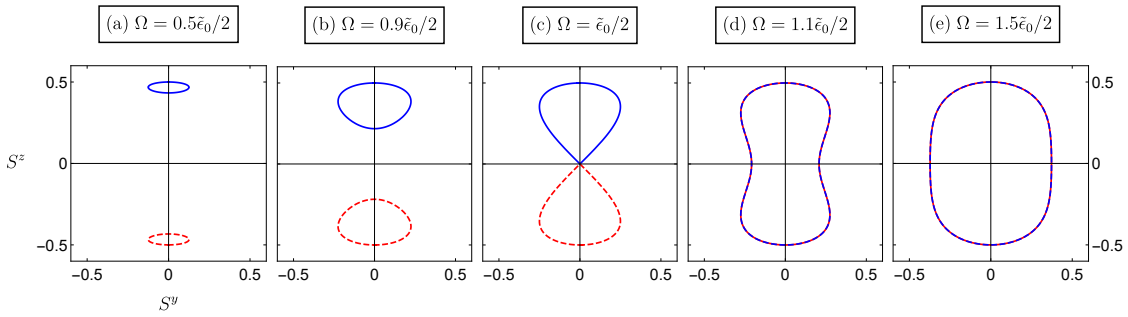


**Figure 3.2** Bifurcation Dynamics (a) - Small oscillations at low Rabi coupling. (b) - Before the critical Rabi coupling at $\Omega = 0.9(\tilde{\epsilon}_0/2)$. The two orbits for the spin up/down initial condition form teardrop shapes and start to meet at the origin which corresponds to the stationary state $(S^x, S^y, S^z) = (1/2, 0, 0)$. (c) - Orbit at the critical Rabi coupling, $\Omega = \tilde{\epsilon}_0/2$. The spin up and spin down orbits meet at the origin and form Homoclinic orbits. This change in dynamics is a Homoclinic Bifurcation. (d) - Past the critical Rabi coupling, $\Omega = 1.1(\tilde{\epsilon}_0/2)$. The two orbits have now merged and explore each other's phase space. As the frequency increases, the orbit becomes a circle centred about the origin. (e) - Rabi Oscillations at high Rabi coupling.

blue (solid line). The equations of motion conserve total spin, so, for clarity, the orbits can be projected down from the Bloch sphere onto the $S^z - S^y$ plane.

At low Rabi coupling, Fig. 3.2 (a), the orbits are small oscillations about the stationary states given by $(S^x, S^y, S^z) = \left(-\Omega/2\tilde{\epsilon}_0, 0, \pm\frac{1}{2}\sqrt{1-(\Omega/\tilde{\epsilon}_0)^2}\right)$. As the Rabi coupling increases, the orbit radius grows in size and the stationary state moves closer to the origin. At high Rabi coupling, Fig. 3.2 (e), the orbits have merged to give full Rabi oscillations about the stationary state $(S^x, S^y, S^z) = (1/2, 0, 0)$. This behaviour can be derived from the collective equations of motion, Eqs. (3.3), as $\tilde{\epsilon}_0$ becomes much smaller than $\Omega$ or zero in the special cases of dipole geometry or $\alpha = \pi/4$.

Fig. 3.2 (b), (c) and (d) show the dynamics at intermediate Rabi couplings. At a critical coupling, $\Omega = \tilde{\epsilon}_0/2$, there is a bifurcation in the dynamics, indicative of a sharp transition in the form of the expected time evolution of the system. We can study this bifurcation more clearly by writing $S^x = \sqrt{S^2 - (S^y)^2 + (S^z)^2}$ and defining new variables $x = \sqrt{2\tilde{\epsilon}_0}S^z/\Omega$ and $y = \sqrt{2\tilde{\epsilon}_0}S^y$. This allows us to rewrite the $S^z$ and $S^y$ equations of motion, Eqs. (3.3), as

$$\begin{aligned} \frac{dx}{dt} &= y, \\ \frac{dy}{dt} &= -\Omega^2\left(1 - \frac{\tilde{\epsilon}_0^{\,2}}{2\Omega^2}\right)x - \Omega^2\tilde{\epsilon}_0 x^3. \end{aligned} \tag{3.4}$$

The Hamiltonian of the system can also be recast as

$$H = \frac{1}{2}\Omega^2 \left(1 - \frac{\tilde{\epsilon_0}^2}{2\Omega^2}\right) x^2 + \frac{1}{4}\Omega^2 \tilde{\epsilon_0} x^4 + \frac{1}{2} y^2. \tag{3.5}$$

The collective equations of motion are now seen to be the equations of motion of a particle in a quartic potential well, which is also an undamped, unforced Duffing oscillator [101]. The potential energy forms a double well, with the spin initial conditions $(S^x, S^y, S^z) = (0, 0, \pm 1/2)$ sitting in one well each. At the bifurcation point, the two orbits hit the top of their respective potential wells and then move beyond them. Therefore, the Homoclinic orbit that arises at the critical frequency is also a separatrix between two different forms of orbits, those inside the double potential well and those outside. We can calculate the value of Rabi coupling at the bifurcation point by equating the energy of the orbit with that of the stationary state $(S^x, S^y, S^z) = (1/2, 0, 0)$, which gives the bifurcation coupling of $\Omega = \tilde{\epsilon_0}/2$ found in the dynamics. In summary, within the assumption of a uniform collective spin, the dynamics undergo a transition from small constrained orbits dominated by the dipole interaction at low Rabi coupling, to full Rabi oscillations at large Rabi coupling. The boundary between these two regimes is given by a bifurcation in the dynamics.

### 3.3.2 Stability to Non-Uniform Modulations

Having established the collective behaviour of the system, it is important to analyse the stability of the collective motion under small perturbations. To quantify this, we linearise the individual spin equations of motion, Eqs. (3.2), about the collective motion by setting $\mathbf{S}_i = \mathbf{S}_{col} + \delta\mathbf{S}_i$ where $\mathbf{S}_i$ is the spin vector on lattice site $i$. We then use the periodicity of the system to Fourier transform the linearised equations and put them into matrix form $d\delta\mathbf{S}_\mathbf{k}/dt = \mathbf{A}_\mathbf{k}(t)\delta\mathbf{S}_\mathbf{k}$ where the matrix $\mathbf{A}_\mathbf{k}(t)$ contains the collective solutions and is therefore periodic. This means that our matrix equation is now a Floquet equation. We can write the solutions to this equation as a matrix that obeys $d\mathbf{X}(t)/dt = \mathbf{A}_\mathbf{k}(t)\mathbf{X}(t)$ which allows us to define the Monodromy matrix $\mathbf{B} = \mathbf{X}(T)$. The Monodromy matrix propagates the solutions forward by one period such that $\mathbf{X}(t+T) = \mathbf{X}(t)\mathbf{B}$. After $n$ periods, we have $\mathbf{X}(t+nT) = \mathbf{X}(t)\mathbf{B}^n$ and so any individual eigenstate of $\mathbf{B}$ obeys $\mathbf{x}_l(t+nT) = \rho_l^n \mathbf{x}_l(t)$, with $\rho_l$ an eigenvalue of $\mathbf{B}$, which we refer to as a Floquet multiplier. More details on Floquet matrix theory are given in Appendix A. We calculate the full spectrum of Floquet multipliers and plot

the largest as a function of Rabi coupling, where any multiplier with magnitude greater than unity represents an instability in the orbit as it leads to exponential growth of fluctuations.

In our analysis of the dynamics of the collective spin of §3.3.1, the tilt of the dipoles, $\Theta$, and anisotropy, $\alpha$, acted only to rescale the parameter $\tilde{\epsilon_0}$. However, in analysing stability to non-uniform spin-states, both $\Theta$ and $\alpha$ can have significant effects. We therefore study three distinct geometries which are representative of all cases. The first is where all the dipoles are perpendicular to the lattice, $\Theta = 0$, giving an isotropic environment at each site. The second is where the dipoles lie in the lattice with $\Theta = \pi/2$. Finally, we consider the dipoles at the so called 'Magic Angle' for which the average dipole interaction vanishes. For 1D, this angle occurs at $\sin^2\Theta = 1/3$ and for 2D occurs at $\sin^2\Theta = 2/3$. We analyse the stability for each of the three dipole arrangements for specific cases of $0 \leq \alpha < \pi$.

### Isotropic

The first case we consider is the isotropic dipole arrangement, $\Theta = 0$. Fig. 3.3 shows the largest Floquet multiplier for specific values of $\alpha$ between 0 and $\pi$ in the 1D system. We find that for all values of $\alpha$, the initial instability behaviour is the same. At low coupling, the multiplier is near unity, but increases in size as a function of Rabi coupling. Stability is expected at zero coupling given that the initial state is an eigenstate of the Hamiltonian. As the Rabi coupling approaches the bifurcation value, the collective dynamics becomes increasingly unstable, reaching maximum values at the bifurcation point. Increasing the Rabi coupling further, past the bifurcation point, the multiplier decreases in value indicating a suppression of the instability. Therefore, we find that, in general, the collective picture is unstable and the only places where it may persist are high Rabi couplings. Our numerics show that in the high Rabi coupling region, stability depends on the value of $\alpha$. For $\pi/4 < \alpha \leq 7\pi/8$, our numerics show the Floquet multiplier never reaches unity except for $\alpha = 3\pi/4$, meaning the collective Rabi oscillations always break apart. However, for $0 \leq \alpha \leq \pi/4$, the multiplier tends to unity again and collective motion persists. Later, we will quantify analytically the high Rabi coupling behaviour and derive the regime of stability.

Moving away from the high Rabi coupling region, we find that for $0 \leq \alpha \leq \pi/4$, the multiplier is close to unity for a Rabi coupling that is comparable to, but still greater than, the dipole interaction. We also note the presence of oscillations in the multiplier value which are robust to changes in system size and geometry. These

oscillations and the stability down to relatively low values of the Rabi coupling stability are unexplained, but do not affect our conclusions in the high Rabi coupling regime.

Across the $\alpha$ range, the bifurcation point is seen to move closer to zero Rabi coupling as we move $\alpha$ from 0 through to $\pi/4$. At $\alpha = \pi/4$ there is complete stability for all values of the Rabi coupling. This can be understood as a consequence of the conservation of total spin which occurs as the Hamiltonian becomes an isotropic Heisenberg Hamiltonian.

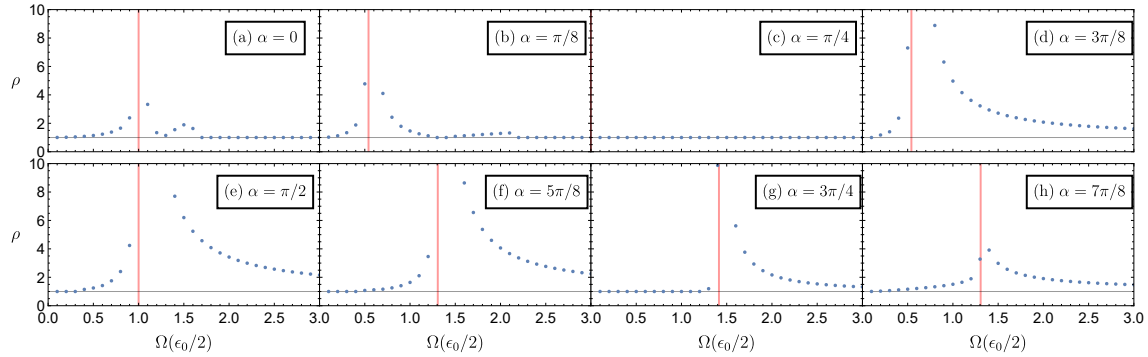


**Figure 3.3** Plots of the largest Floquet multiplier for the 1D system. The multiplier is plotted as a function of Rabi coupling. The bifurcation line is shown in red. For each plot, the system is unstable for low Rabi coupling across the bifurcation point. However, for $\alpha < \pi/4$, the multipliers are in general smaller than for $\alpha > \pi/4$ and also the curves return to unity at high Rabi coupling.

In Fig. 3.4, we plot the largest Floquet multiplier for the 2D system for the same $\alpha$ values. The qualitative results are the same as the 1D system, with the only difference being stability for the case $\alpha = 7\pi/8$ in 2D at high Rabi coupling. Overall, in both 1D and 2D, we find stability of the collective state can only be obtained either at high Rabi coupling, zero Rabi coupling, or when $\alpha = \pi/4$. Small perturbations otherwise broaden the bifurcation peak in the collective dynamics.

### In Plane

We now consider the case where the dipoles lie along the lattice, $\Theta = \pi/2$. For the 1D case, there is no change in stability due to the fact that tilting the dipoles only changes the relative sign of the interaction. Therefore, the results of the stability analysis will mirror that for the 1D isotropic case. For 2D however, the tilting of dipoles creates anisotropy in the dipole interaction and will have different effects. Fig. 3.5 shows the Floquet multiplier results. The same broad instability behaviour about the bifurcation

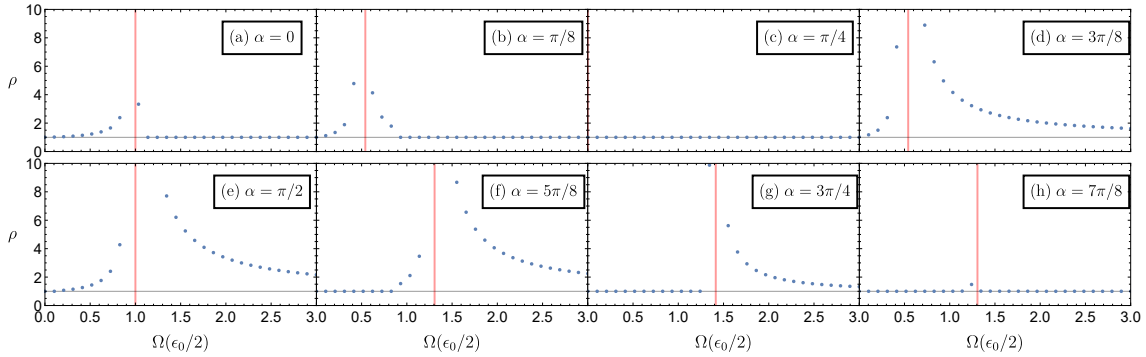


**Figure 3.4** Plots of the largest Floquet multiplier for the 2D isotropic system, with the bifurcation line shown in red. The multiplier is plotted as a function of Rabi coupling. The results are similar to those in 1D, but with stability arising for $\alpha = 7\pi/8$ at high Rabi coupling.

coupling is seen, but in contrast to the isotropic case, the only situation where stable orbits occur at high Rabi coupling is when $\alpha = \pi/4$.

#### Magic Angle

Finally, we consider the case where the dipoles are oriented at the magic angle which leads to an average zero dipole interaction. For 1D, the dipole interaction cancels entirely and so stable Rabi oscillations are seen across the entire Rabi coupling range for all $\alpha$ values. For 2D, the dipole interaction only cancels on average and so instability can still arise from fluctuations. We find that at low Rabi coupling, fluctuations give rise to large instabilities, but at large Rabi coupling, the system becomes stable again for $0 \leq \alpha \leq 3\pi/4$ and remains unstable for $3\pi/4 < \alpha < \pi$. Because of the average dipole cancellation, the time period of the collective state depends purely on the Rabi coupling and there is no longer a bifurcation or critical coupling. In Fig. 3.6 we show the Floquet multiplier results for $\alpha = 5\pi/8$, $\alpha = 3\pi/4$ and $\alpha = 7\pi/8$. Any oscillatory behaviour in the Floquet multiplier at low coupling is a finite size effect.

### 3.3.3 Analytical Analysis at High Rabi Coupling

Our numerical Floquet analysis showed that collective behaviour was only stable in the high Rabi coupling limit under certain ranges of $\alpha$ and with certain tilt angles of the dipoles. Here, we analytically compute when the collective picture is stable in the high Rabi coupling limit and compare to our numerical results. To do this, we move

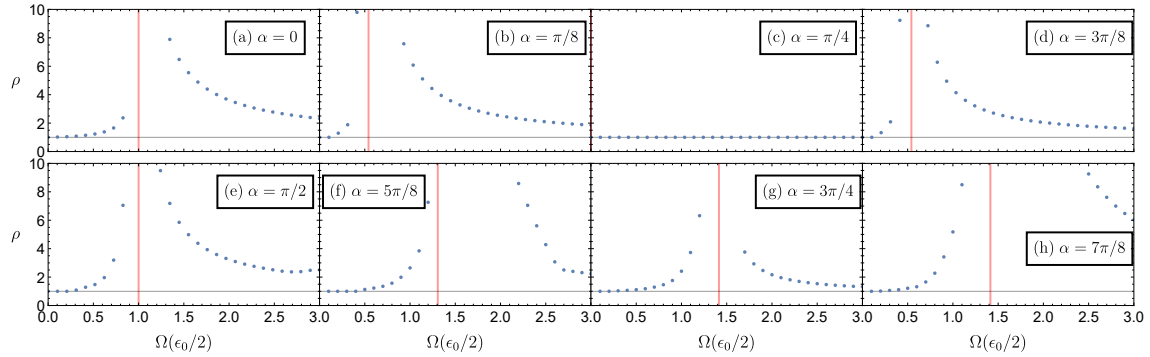


**Figure 3.5** Plots of the largest Floquet multiplier for a 2D lattice for an in plane geometry. The multiplier is plotted as a function of Rabi coupling. The bifurcation line is shown in red. For each plot, we see the system is unstable for low Rabi coupling across the bifurcation point, but also unstable at high Rabi couplings in contrast to the isotropic case.

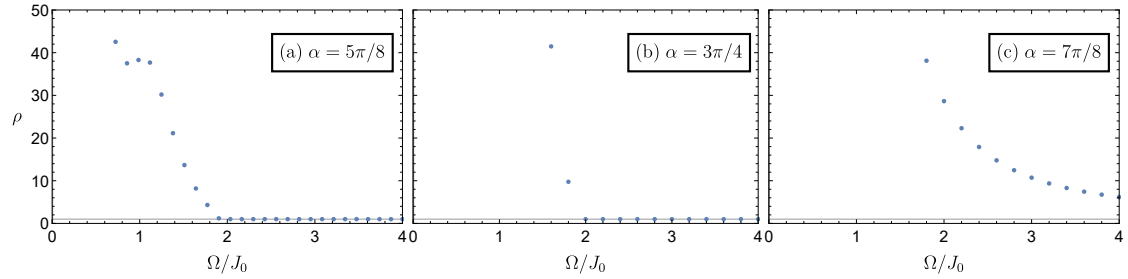


**Figure 3.6** Plots of the largest Floquet multiplier for a 2D system at the magic angle, $\sin^2\Theta = 2/3$. The multiplier is plotted as a function of Rabi coupling. The system is stable at high Rabi coupling for $0 \leq \alpha \leq 3\pi/4$, and unstable for $3\pi/4 < \alpha < \pi$.

to a frame rotating at the Rabi frequency, obtaining a time-dependent Hamiltonian with no Rabi term to which we apply a Magnus expansion, as outlined in Ref. [102], in powers of $J_0/\Omega$. We start with the time dependent Hamiltonian we obtain from applying the unitary transform $\hat{U} = \exp\left[i\Omega/2\sum_i^N \hat{\sigma}_i^x\right]$ to Eq. (3.1). Splitting into time

independent and dependent parts gives

$$\begin{aligned}\hat{H}_{rot} = \hat{H}_{stat} + \hat{V}(t) = &\sum_{\substack{i,l \\ i\neq l}}^{N} \frac{J_{il}}{4r_{il}^3}\left(\sin\alpha\hat{\sigma}_i^x\hat{\sigma}_l^x + \frac{\sin\alpha}{2}\hat{\sigma}_i^y\hat{\sigma}_l^y + \frac{\cos\alpha}{2}\hat{\sigma}_i^z\hat{\sigma}_l^z\right) \\ &+ \sum_{\substack{i,l \\ i\neq l}}^{N} \frac{J_{il}}{4r_{il}^3}\left(\frac{\cos\alpha - \sin\alpha}{2}\right)\left(\cos(2\Omega t)\left(\hat{\sigma}_i^z\hat{\sigma}_l^z - \hat{\sigma}_i^y\hat{\sigma}_l^y\right) + 2\sin(2\Omega t)\hat{\sigma}_i^y\hat{\sigma}_l^z\right) \\ &+ \sum_{i}^{N} \frac{\Delta_i}{2}\left(\hat{\sigma}_i^z\cos(\Omega t) + \hat{\sigma}_i^y\sin(\Omega t)\right),\end{aligned} \tag{3.6}$$

where we have introduced a detuning term to our original Hamiltonian, Eq. (3.1), with $\Delta_i \equiv \omega_{0i} - \omega$, where $\omega$ is the applied field frequency, and $\omega_{0i}$ the two-level transition frequency on site $i$. We now write the potential in terms of Fourier components

$$\begin{aligned}\hat{V}^{\pm 1} &= \sum_{l} \frac{\Delta_l}{4}\left(\hat{\sigma}_l^z \mp i\hat{\sigma}_l^y\right), \\ \hat{V}^{\pm 2} &= \sum_{\substack{j,l \\ j\neq l}} \frac{J_{jl}(\cos\alpha - \sin\alpha)}{16r_{jl}^3}\left[\hat{\sigma}_j^z\hat{\sigma}_l^z - \hat{\sigma}_j^y\hat{\sigma}_l^y \mp 2i\hat{\sigma}_j^y\hat{\sigma}_l^z\right].\end{aligned} \tag{3.7}$$

Following [102], we can now make the following unitary transform, $\hat{U} = \exp\left[i\hat{K}(t)\right]$, to move to a rotating frame that removes the time dependent parts. This gives the effective Hamiltonian

$$\hat{H}_{\text{eff}} = e^{i\hat{K}(t)}\hat{H}(t)e^{-i\hat{K}(t)} + i\frac{\partial e^{i\hat{K}(t)}}{\partial t}e^{-i\hat{K}(t)}. \tag{3.8}$$

We can expand $\hat{K}$ and $\hat{H}$ in powers of $1/\Omega$ and, by comparing powers, obtain the following

$$\begin{aligned}\hat{H}_0 &= \hat{H}_{stat}, \\ \hat{H}_1 &= \frac{1}{\Omega}\sum_{j=1}^{\infty}\frac{1}{j}\left[\hat{V}^{(j)}, \hat{V}^{(-j)}\right], \\ \hat{H}_2 &= \frac{1}{2\Omega^2}\sum_{j=1}^{\infty}\frac{1}{j^2}\left(\left[\left[\hat{V}^{(j)}, \hat{H}_0\right], \hat{V}^{(-j)}\right] + h.c.\right),\end{aligned} \tag{3.9}$$

where *h.c.* denotes the Hermitian conjugate. The effective high frequency Hamiltonian is simply given by the time independent Hamiltonian, $\hat{H}_{stat}$, which is explicitly given as

$$\hat{H}_0 = \sum_{\substack{i,l \\ i\neq l}}^{N} \frac{J_{il}}{4r_{il}^3}\left[\sin\alpha\hat{\sigma}_i^x\hat{\sigma}_l^x + \frac{\sin\alpha+\cos\alpha}{2}\left(\hat{\sigma}_i^y\hat{\sigma}_l^y + \hat{\sigma}_i^z\hat{\sigma}_l^z\right)\right], \tag{3.10}$$

while the the next term in the expansion is given by

$$\hat{H}_1 = \frac{1}{\Omega}\sum_{i}^{N}\Delta_i^2\hat{\sigma}_i^x + \frac{\cos\alpha-\sin\alpha}{32\Omega}\sum_{\substack{i,k,l \\ i\neq l \\ k\neq l}}^{N}\frac{J_{il}J_{kl}}{r_{il}^3 r_{kl}^3}\left(\hat{\sigma}_i^y\hat{\sigma}_k^y + \hat{\sigma}_i^z\hat{\sigma}_k^z\right)\hat{\sigma}_l^x. \tag{3.11}$$

The Kick operator to first order is given by

$$\begin{aligned}\hat{K}(t) =& \frac{1}{2\Omega}\sum_{i}^{N}\Delta_i\left(\hat{\sigma}_i^z\sin(\Omega t) - \hat{\sigma}_i^y\cos(\Omega t)\right) + \\ & \frac{1}{\Omega}\sum_{\substack{i,l \\ i\neq l}}^{N}\frac{J_{il}}{4r_{il}^3}\left(\frac{\cos\alpha-\sin\alpha}{4}\right)\left(\sin(2\Omega t)\left(\hat{\sigma}_i^z\hat{\sigma}_l^z - \hat{\sigma}_i^y\hat{\sigma}_l^y\right) - 2\cos(2\Omega t)\hat{\sigma}_i^y\hat{\sigma}_l^z\right).\end{aligned} \tag{3.12}$$

We now study the stability of persistent Rabi oscillations by performing a spin wave analysis [14] of the effective Hamiltonian about the $S^z$ collective state. We apply a spin wave analysis, where, for a generic spin magnitude $S$, we have the following transformations

$$\begin{aligned}\hat{S}_i^- &= \hat{a}_i^\dagger(2S - \hat{a}_i^\dagger\hat{a}_i)^{1/2} \approx \sqrt{2S}\hat{a}_i^\dagger, \\ \hat{S}_i^+ &= (2S - \hat{a}_i^\dagger\hat{a}_i)^{1/2}\hat{a}_i \approx \sqrt{2S}\hat{a}_i, \\ \hat{S}_i^z &= S - \hat{a}_i^\dagger\hat{a}_i,\end{aligned} \tag{3.13}$$

where $\hat{a}_i^\dagger$ and $\hat{a}_i$ are the bosonic creation and annihilation operators on site $i$ respectively. Applying these transformations for $S = 1/2$ and introducing the Fourier transform, $\hat{a}_i = \sum_{\mathbf{q}}\hat{a}_{\mathbf{q}}e^{i\mathbf{q}\cdot\mathbf{r}_i}/\sqrt{N}$, transforms the Hamiltonian into the following form

$$\hat{H} = \sum_{\mathbf{q}} A_{\mathbf{q}}\left(\hat{a}_{\mathbf{q}}^\dagger\hat{a}_{\mathbf{q}} + \hat{a}_{-\mathbf{q}}^\dagger\hat{a}_{-\mathbf{q}}\right) + B_{\mathbf{q}}\left(\hat{a}_{\mathbf{q}}^\dagger\hat{a}_{-\mathbf{q}}^\dagger + \hat{a}_{-\mathbf{q}}\hat{a}_{\mathbf{q}}\right) + O(\hat{a}_{\mathbf{q}}^4), \tag{3.14}$$

where $A_{\mathbf{q}} = (\cos\alpha + 3\sin\alpha)\epsilon_{\mathbf{q}}/8 - (\cos\alpha+\sin\alpha)\epsilon_{\mathbf{0}}/4$ and $B_{\mathbf{q}} = (\sin\alpha - \cos\alpha)\epsilon_{\mathbf{q}}/8$. Note that in Eq. (3.14) we have ignored any constant terms. The quantity $\epsilon_{\mathbf{q}}$ is the

dipole dispersion relation defined by

$$\epsilon_{\mathbf{q}} = \sum_{i}^{N} J_0 a^3 (1 - 3\cos^2\phi_{\mathbf{R}_i}\sin^2\Theta)\frac{e^{i\mathbf{q}\cdot\mathbf{R}_i}}{|\mathbf{R}_i|^3}, \tag{3.15}$$

where $\phi_{\mathbf{R}}$ is the angle between the position vector, $\mathbf{R}_i$, and the $x$ axis. To obtain the spectrum of excitations about the collective $S^z$ state, we apply the following Bogoliubov transform

$$\hat{a}_{\mathbf{q}} = \cosh\theta\hat{\alpha}_{\mathbf{q}} + \sinh\theta\hat{\alpha}^{\dagger}_{\text{-}\mathbf{q}}, \tag{3.16}$$

$$\hat{a}^{\dagger}_{\mathbf{q}} = \cosh\theta\hat{\alpha}^{\dagger}_{\mathbf{q}} + \sinh\theta\hat{\alpha}_{\text{-}\mathbf{q}}, \tag{3.17}$$

$$\tanh 2\theta = \frac{(\sin\alpha - \cos\alpha)\epsilon_{\mathbf{q}}}{2(\sin\alpha + \cos\alpha)\epsilon_{\mathbf{0}} - (3\sin\alpha + \cos\alpha)\epsilon_{\mathbf{q}}}, \tag{3.18}$$

which diagonalises the Hamiltonian to give

$$H = \sum_{\mathbf{q}} E_{\mathbf{q}}\hat{\alpha}^{\dagger}_{\mathbf{q}}\hat{\alpha}_{\mathbf{q}} + O(\hat{\alpha}^4_{\mathbf{q}}), \tag{3.19}$$

where we have again ignored any constant terms. The spin-wave excitation spectrum is given by

$$E_{\mathbf{q}} = \frac{1}{2}\sqrt{(\epsilon_{\mathbf{q}} - \epsilon_0)(\sin\alpha + \cos\alpha)((2\epsilon_{\mathbf{q}} - \epsilon_0)\sin\alpha - \epsilon_0\cos\alpha)}. \tag{3.20}$$

By studying when the excitation spectrum becomes imaginary, we can find when Rabi oscillations are unstable. Also note that as the momentum tends to zero, the excitation spectrum also tends to zero. This is consistent with the presence of a Goldstone boson, related to the continuous symmetry of the Hamiltonian under rotations around $S^x$.

Before examining the excitation spectrum for each of the three geometries, we establish the low momentum limit of the dipole dispersion, Eq. (3.15), which is important in determining the stability of Rabi oscillations. In 1D, $\phi_{\mathbf{R}} = 0$ and so we can expand Eq. (3.15) directly to obtain the following low momentum behaviour

$$\epsilon_q = \left(1 - 3\sin^2\Theta\right)\left(\epsilon_0^{(1\mathrm{D})} - J_0 a^2 q^2 + O(q^4)\right), \tag{3.21}$$

where $\epsilon_0^{(1D)} \approx 2.4J_0$. In 2D, due to the angle $\phi_{\mathbf{R}}$, we need to separate the dipole dispersion into different angular components

$$\epsilon_{\mathbf{q}} = \epsilon_{\mathbf{q}}^0 \left(1 - \frac{3}{2}\sin^2\Theta\right) - \frac{3}{2}\sin^2\Theta\left(\epsilon_{\mathbf{q}}^{(2)} + \epsilon_{\mathbf{q}}^{(-2)}\right), \tag{3.22}$$

where

$$\epsilon_{\mathbf{q}}^{(m)} = J_0 a^3 \sum_i^N \frac{e^{i\mathbf{q}\cdot\mathbf{R}_i + im\phi_{\mathbf{R}}}}{|\mathbf{R}_i|^3}. \tag{3.23}$$

For a large number of spins, the spectrum is conveniently found via Ewald summation [64, 103]. This involves rewriting the dispersion in terms of Bessel functions of the first kind, which on expansion give

$$\begin{aligned}\epsilon_{\mathbf{q}} &= \epsilon_0^{(2D)}\left(1 - \frac{3}{2}\sin^2\Theta\right) \\ &+ 2\pi J_0|\mathbf{q}|a\left(-1 + \frac{3}{2}\sin^2\Theta - \sin^2\Theta\cos 2\psi\right) \\ &+ J_0|\mathbf{q}|^2a^2\left(1 - \frac{3}{2}\sin^2\Theta - \eta\sin^2\Theta\cos 2\psi\right),\end{aligned} \tag{3.24}$$

where $\eta \simeq 0.23$ is a numerical constant. Here, $\epsilon_0^{(2D)} \approx 9J_0$ and $\psi$ is the angle between the $\mathbf{q}$ vector and the $q_x$ axis. The key difference between 1D and 2D is the presence of the linear term in momentum. Given the low momentum expansion of the dipole interactions, we can now study the stability of Rabi oscillations for the different geometries.

### Isotropic

For the isotropic case, stability is predominantly determined by low momentum fluctuations. Applying the low momentum expansions in the excitation spectrum gives $E_{\mathbf{q}} = \sqrt{\epsilon_0^{(2D)}\cos(2\alpha)(2\pi J_0|\mathbf{q}|a)}$ in 2D and $E_{\mathbf{q}} = \sqrt{\epsilon_0^{(1D)}\cos(2\alpha)(J_0q^2a^2)}$ for 1D. We find that stability depends only on the value of $\alpha$. For $0 \leq \alpha \leq \pi/4$, the spectrum is real and therefore we have stable Rabi oscillations. However, for $\pi/4 < \alpha < 3\pi/4$, the spectrum becomes imaginary and Rabi oscillations become unstable. Both these outcomes agree with the numerical analysis. We can see here that $\alpha = \pi/4$ and $\alpha = 3\pi/4$ result in zero excitation spectrum. When $3\pi/4 < \alpha$, the spectrum becomes imaginary as high momentum fluctuations cause instabilities instead of low momentum ones, but this is the only region where this occurs. The spectrum is real again when $7\pi/8 < \alpha$ in 1D and $2.506 < \alpha$ in 2D.

To compare our analytical results to our numerical results further, we can calculate the decay rate of the collective state in the unstable regions. From the spectrum of the $S^z$ state, the time scale of decay is derived from the momentum that causes maximum instability i.e. gives the largest imaginary component. When $\pi/4 < \alpha < 3\pi/4$, this maximum decay occurs when $\epsilon_{\mathbf{q}} = (3\sin\alpha + \cos\alpha)\epsilon_0/(4\sin\alpha)$, which gives an energy and corresponding decay time of

$$\mathrm{Im}(E) = 1/\tau = \frac{\epsilon_0(\sin\alpha - \cos\alpha)}{4\sqrt{2}}\sqrt{\frac{\sin\alpha + \cos\alpha}{\sin\alpha}}, \tag{3.25}$$

where we have assumed the expectation value of the spins decays as $\exp(iEt)$. However, when $3\pi/4 < \alpha < \pi$, there are still decay modes in certain cases, and these occur for $q = \pi$. The Floquet multipliers relate to the decay of the initial state in the following way

$$\mathbf{x}(t + nT) = \rho^n \mathbf{x}(t), \tag{3.26}$$

where $\mathbf{x}(t)$ is a vector of the classical solutions and the Floquet multiplier sets the growth rate of fluctuations/decay of the collective orbit. Given an initial state $\mathbf{x}(t)$, we can relate these two time scales by

$$\log\left(\frac{\mathbf{x}(t + nT)}{\mathbf{x}(t)}\right) = n\log(\rho) = \frac{nT}{\tau}, \tag{3.27}$$

where $\tau = 1/\mathrm{Im}[E]$. Therefore,

$$\tau = \lim_{\Omega\to\infty} \frac{T}{\log(\rho)}. \tag{3.28}$$

Fig. 3.7 shows the decay times for different values of $\alpha$ for the 1D isotropic case plotted with the theoretical curves from our analytic results. The blue (darker) curve is the decay time from Eq. (3.25) and the orange (lighter) curve from Eq. (3.20) at $q = \pi$. The agreement is excellent.

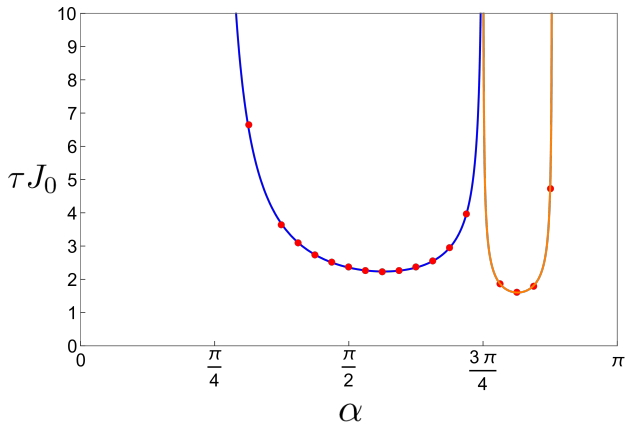


**Figure 3.7** Decay times for the 1D Floquet system. The blue (darker) curve is the analytic curve for decay from Eq. (3.25), the orange (lighter) curve is the excitation spectrum evaluated at $q = \pi$ and the points are the Floquet multipliers for $\Omega = 50\epsilon_0$. The numerically computed Floquet multipliers are very close to the analytic curve.

### In Plane

As we mentioned before in the Floquet analysis, §3.3.2, there is no change in the stability of the 1D dipole system when the dipoles lie in the lattice plane, as the head-head interactions simply becomes head-tail interactions, which leads to a change in sign of $J_0$. We can see this directly from the low momentum expansion Eq. (3.21). However, in 2D, there is now both head-head and head-tail interactions which gives an anisotropy to the dipole interaction. The 2D low momentum expansion, Eq. (3.24), has a negative quadratic dispersion along one direction, and positive linear dispersion along another, due to the $\cos 2\psi$ term. This means that the excitation spectrum Eq. (3.20) is unstable at both low and high momenta for all values of $\alpha$, as along certain directions the spectrum is imaginary. This again agrees with our numerical results which showed instability at high Rabi coupling for all values of $\alpha$ except $\alpha = \pi/4$ and $\alpha = 3\pi/4$.

As for the isotropic case, we can compute decay times to compare analytics and numerics. These are plotted in Fig. 3.8 for the 2D system. Although not plotted here the 1D curve is identical to that from the isotropic case. We see that the 2D data fits the theoretical curve well.

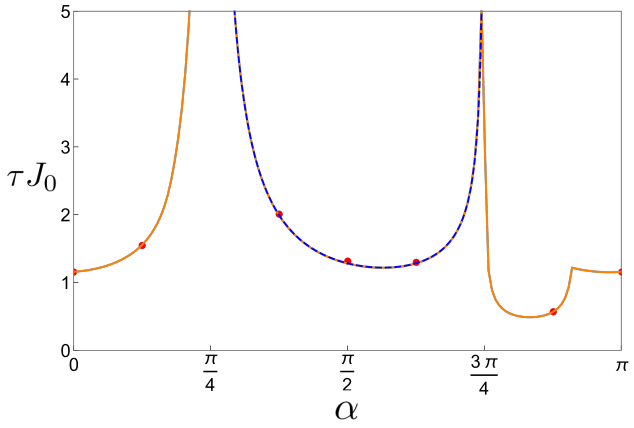


**Figure 3.8** Decay times for the 2D system with dipoles in plane. The blue (darker) curve is the analytic curve from the $\alpha$ decay and the orange (lighter) curve from numerical analysis of Eq. (3.20). The points are the Floquet multipliers evaluated at $\Omega = 50\epsilon_0$. The numerically computed Floquet multipliers match the analytic curve very well.

### Magic Angle

Lastly, we consider the case where the dipoles lie at the magic angle. For 1D, the dipole interaction disappears completely, so $\epsilon_q = 0$ for all momenta and there are no effects of spin-wave fluctuations at any Rabi coupling. For 2D, whilst $\epsilon_0 = 0$, the dipole interaction only cancels along certain directions. The fluctuation spectrum becomes

$$E_{\mathbf{q}} = \epsilon_{\mathbf{q}} \sqrt{2 \sin\alpha (\sin\alpha + \cos\alpha)}. \tag{3.29}$$

The average cancellation of the dipole interaction allows us to pull the dipole dispersion out of the square root. Now the stability of this spectrum depends purely on the relative strengths of the Ising and XY terms in the Hamiltonian and becomes unstable if $3\pi/4 < \alpha < \pi$, as seen in our numerical results.

### Higher Order Corrections

In our spin wave analysis, we have only focused on the leading term in the Magnus expansion, finding it gives excellent agreement with our numerical results at high Rabi coupling. We expect that terms of order $1/\Omega$ (see Eq. (3.11)) or higher in the Magnus expansion will also capture lower Rabi coupling behaviour under spin wave analysis, but have the additional complication of the kick operator. Study of the effective Hamiltonian by itself at higher orders results in a conservation of total $S^x$ which is

not physical at lower Rabi coupling and so the kick operator (which violates total $S^x$ conservation) must be included to capture the full system dynamics. However, this has no influence on our results, which are at zeroth order, as the leading term of the kick operator is of order $1/\Omega$.

## 3.4 Discussion

We have established the form of the collective dynamics of the system and the regimes and geometries under which the coherent collective dynamics of all two-level systems are stable against non-uniform modulations. We find in both 1D and 2D that stability occurs across the entire Rabi coupling range for $\alpha = \pi/4$ and otherwise stability occurs only at high Rabi coupling under certain conditions and dimensionality. In this high Rabi coupling limit, one can determine stability of the collective picture from the spectrum of spin waves of the effective Hamiltonian, Eq. (3.20). We use this to plot a phase diagram of the system in the high Rabi coupling regime as a function of tilt angle $\Theta$ and the relative strengths of the Ising and XY interaction, $\alpha$. These phase diagrams are shown in Fig. 3.9 and Fig. 3.10 for the 1D and 2D system respectively.

Summarising the key features of the phase diagrams, we find that for the isotropic geometry, $\sin^2\Theta = 0$, only the regions $0 \leq \alpha \leq \pi/4$, $\alpha = 3\pi/4$ or $\alpha_c < \alpha \leq \pi$ leads to stable Rabi oscillations in 1D and 2D. For $\pi/4 < \alpha < 3\pi/4$, instabilities arise from low momentum fluctuations whilst for $3\pi/4 < \alpha < \alpha_c$, instabilities arise from high momentum fluctuations. The cut off angle $\alpha_c$ is the value of $\alpha$ beyond which high momentum fluctuations cannot cause instability and we find these values take $\alpha_c^{(1\mathrm{D})} = 7\pi/8$ and $\alpha_c^{(2\mathrm{D})} = 2.506$ for 1D and 2D respectively. Increasing the tilt of the dipoles, we find these conditions of stability do not change in 1D where tilting the dipoles only scales the interaction strength, except at the magic angle where the dipole interactions cancel exactly. However, in 2D, the collective picture becomes unstable for all $\alpha$ past a certain value of $\sin^2\Theta$, when the anisotropy in the dipole dispersion becomes large enough to destabilise the excitation spectrum. We also find that $\alpha_c^{(2\mathrm{D})}$ depends on the tilt angle. Once the tilt reaches the magic angle, the average dipole interaction cancels and we again obtain stability across all values of $\alpha$ except in the range $3\pi/4 < \alpha < \pi$ for 2D.

The existence of stable collective Rabi oscillations over a range of Rabi couplings at the magic angle is surprising in 2D, given that small scale fluctuations still exist and otherwise destabilise the collective picture at tilt angles above and below the critical

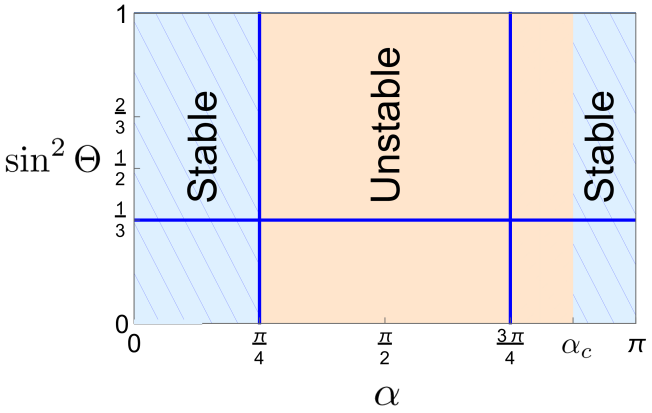


**Figure 3.9** Phase diagram at high Rabi coupling in 1D. The blue (lined) regions represent stability and the orange (plain) regions represent instability. The $\alpha = \pi/4$ line is stable across all tilt angles due to the Heisenberg symmetry. The magic angle line at $\sin^2\Theta = 1/3$ is stable across the entire $\alpha$ range and occurs due to the cancellation of the entire dipole interaction. There is a region of instability between $3\pi/4 < \alpha \leq 7\pi/8$ due to high momentum fluctuations.

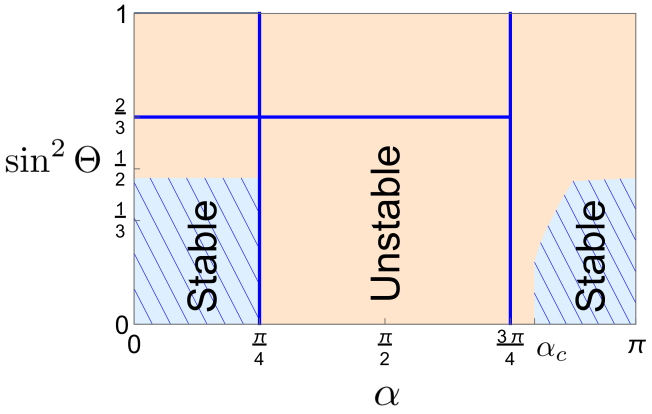


**Figure 3.10** Phase diagram at high Rabi coupling in 2D. The blue (lined) regions represent stability and the orange (plain) regions represent instability. As for 1D, the $\alpha = \pi/4$ line is stable across all tilt angles due to the Heisenberg symmetry. The magic angle line at $\sin^2\Theta = 2/3$ is stable up to $\alpha = 3\pi/4$. Unlike in 1D, the anisotropy in the dipole interaction causes instability as the dipoles are tilted for $0 \leq \alpha \leq \pi/4$.

line. It would be interesting to see how this depends on the underlying geometry and why the fluctuations can behave in such a way that stability is retained. In all other cases, the collective picture breaks apart after a finite time set by the value of the Floquet multiplier, with quickest decay of the collective dynamics occurring at the bifurcation coupling. By studying the time evolution of the system in the unstable regions via numerical simulations, we find that chaotic dynamics dominate and possible thermal states form. For example, at low Rabi coupling when $0 < \alpha < \pi/4$, we find there is an average steady state of spins lying in the $xz$ plane. This result is similar to those of exact diagonalization results in a system with Van der Waals interactions [56].

Our results in this section rely on two important approximations. One approximation is the truncation of the Magnus expansion to lowest order. This neglects terms of order $J_0^2/\Omega$, so our results should hold at least up to time scales of $t \approx \Omega/J_0^2$. While our results could persist much longer than this, the full Magnus expansion is expected to break down on time scales that are exponentially long in $\Omega/J_0$, which sets an upper limit for the lifetime of stable oscillations before the system becomes ergodic and heats to infinite temperature [104]. The other approximation is to treat the effective Hamiltonian Eq. (3.10) within the classical approximation. Exact diagonalization of the effective Hamiltonian shows that for small systems (up to $N = 12$), the classical approximation breaks down due to spin squeezing [105], where quantum fluctuations of the collective spin grow in the $zy$ plane. Consequently the classical approximation is only valid up to times of order $t \approx 2\sqrt{N}/\tilde{\epsilon_0}$. Thus, for any finite systems the Rabi oscillations will dephase for all $\alpha$.

Finally, we comment on how our results relate to experiment. In our analysis, we have implemented periodic boundary conditions as a convenient way of studying the thermodynamic limit. From numerical simulations of the dynamics of systems with open boundary conditions in 1D and 2D, we find that the collective oscillation can break down more easily for small systems with open boundary conditions than for periodic boundary conditions. However, these finite size effects become insignificant at the high Rabi couplings for which we predict collective behaviour and our analytic analysis becomes valid. Indeed, the analytic results at high Rabi coupling are readily performed also for open boundary conditions, and lead to the same conclusions and same phase diagrams. Therefore, we expect our results to hold in systems that are large, but still well below the thermodynamic limit.

Furthermore, in Fig. 3.7 and Fig. 3.8, we have calculated the dephasing time of our system which we now compare to other experimental time scales. If we consider a

system of KRb molecules with $J_0/h = 52\text{Hz}$, where $h$ is Planck's constant, then this gives a decay time of around $2s$ (for $\alpha = \pi/2$). This is much lower than the lifetime of the molecules (up to $25s$) [53] so the breakdown of Rabi oscillations should be evident in experiment. Similarly, for Rydberg atoms under resonant exchange ($\alpha = \pi/2$), we find dephasing time scales of $25\mu s$ and Rydberg lifetimes of up to $100\mu s$ in the absence of motional dephasing [65], so again, we expect our results to be observable.

Lastly, we briefly studied the numerics of non-unity filling fraction and detuning which can arise in experimental set up. We first consider non-unity filling disorder, where each site is randomly occupied or unoccupied with an occupation probability of 0.75. The decay time is calculated for each configuration and averaged over 100 different configurations. Results are shown in Fig. 3.11.

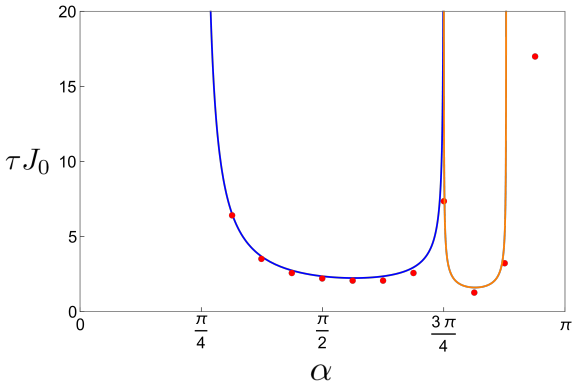


**Figure 3.11** Decay times of a 1D system where each site has an occupation probability of 0.75. We find that filling disorder can cause decay in the region $\alpha_c < \alpha < \pi$ which is stable at unity filling, but with long decay times. Otherwise, filling disorder causes no other instabilities.

We find that the same stability/instability transition as for the homogeneous system, except in the range $\alpha_c < \alpha < \pi$ which becomes unstable, but with large decay times. Therefore, in this range, we expect breakdown of the Rabi oscillations will occur, but otherwise our results should hold in the presence of filling disorder. We find that at high Rabi coupling, any effects from filling disorder do not appear to be significant for $0 \leq \alpha < \alpha_c$. Inhomogeneity did seem to cause decay for $\alpha_c < \alpha < \pi$ where before the system was stable, but with large decay times. Therefore, experimentally, the Rabi oscillations will eventually breakdown in this region.

We also calculate the decay time for small random detunings that are Gaussian distributed about zero with a standard deviation $W = 0.1J_0$, and once again average over 100 configurations. The decay times are shown in Fig. 3.12.

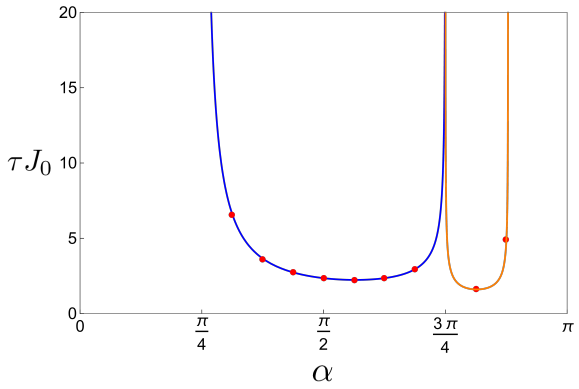


**Figure 3.12** Decay times of a 1D system with small random detunings that are Gaussian distributed about zero with a standard deviation of $W = 0.1J_0$. We find the detuning disorder does not cause further instabilities compared to the ordered system.

We find no change in stability across the entire range of $\alpha$. This agrees with our Magnus expansion, where detuning appears as a $1/\Omega$ term and so should be negligible at high enough Rabi coupling. Non-unity filling, however, appears even at zeroth order in the Magnus expansion as it modifies the dipole coupling $J_{il}$. In both disorder studies, we have looked at a low level of disorder. We expect that at strong enough disorder, more instabilities will arise and Rabi oscillations will break down for all $\alpha$.

## 3.5 Conclusions

We have studied a system of interacting dipoles with both an Ising and XY dipole interaction terms under external driving in both 1D and 2D. After preparing all the spins in an ideal $S^z$ state, we found that collective behaviour occurred, with Rabi oscillations at high Rabi coupling, small oscillations at low Rabi coupling and a bifurcation in the dynamics at a critical value of coupling. Using Floquet analysis, we have found that the collective picture is unstable for most values of Rabi coupling. However, we did find stable collective behaviour at high coupling under certain regimes, either when the dipoles are oriented at the magic angle or when the Ising interaction dominates over the XY interaction.

# Chapter 4

# Phases of driven two-level systems with local dissipation

## 4.1 Introduction

In this chapter, we now examine how dissipation alters the dynamics of a dipole coupled quantum system. Whereas dissipative processes have been viewed as an issue in experiment, recent work has shown that the interplay between an external drive and dissipation can produce exotic non-equilibrium phases such as spin density waves, persistent oscillations and phase bistabilities within spin-1/2 systems [106–109] and also higher spin systems [110] or systems with mixtures of atomic species [111].

In order to capture the steady state phases in a macroscopically large system, it is common to employ a mean-field approximation, where correlations between sites are ignored. While the use of the mean-field approximation is well understood in equilibrium phenomena, a key question that still remains is the validity of the mean-field approximation for dissipative systems. For thermal gases, the mean-field approximation becomes valid as quantum fluctuations become negligible [112, 113]. However, for cold systems, this is not necessarily the case. There have already been many studies into the true phases and transitions for the driven dissipative systems, using variational methods [114], Keldysh methods [115], cluster mean-field [116–118], Monte Carlo [119] and also t-DMRG [120] and other Matrix Product Operator methods [121, 122]. These studies have shown that first order transitions in the mean-field approximation can become second order when quantum fluctuations are included, and that bistabilities can be lost [114, 115, 117, 121, 122]. They have also shown

that the emergence of certain phases, such as antiferromagnetism phases or long-time oscillations may not occur in low dimensional spin-1/2 systems [115, 116, 118, 119].

Despite the disagreements between mean-field and exact numerics of quantum systems, the mean-field approximation can still serve as an indicator of features that emerge in the full quantum system. For example, it has been shown that regions of mean-field bistability for the Ising model correspond to long spatial correlations in the full quantum model [123]. Also, while it has been shown that true bistability cannot occur for finite sized quantum systems [124], the bistable nature of the mean-field solutions is evident in quantum trajectories of the system [125–127] and also results in a decrease in the spectral gap of the Liouvillian [108]. Therefore, it is interesting to ask to what degree the mean-field imprints itself on the dynamics and phases of the full quantum system.

In this chapter, we study a driven-dissipative XXZ model with a tunable ratio between the XY and Ising near-field dipole interactions, which was studied in Chapter 3, as a function of detuning and external drive. We calculate the non-equilibrium phase diagram at mean-field level, finding many phases such as antiferromagnetism, spin density waves, persistent oscillations and bistabilities. We then analyse small quantum systems and carry out an in-depth comparison to the mean-field phase diagram. As for similar previous studies, while we do not find the same phase diagram for the full quantum system, we do find strong signatures of the mean-field in the spin fluctuations which relate to bistabilities and spatial phases that arise in the mean-field results.

The rest of this chapter is organised as follows. In Section 4.2, we describe the model. Then in Section 4.3, we derive the mean-field phase diagram as a function of parameters. In Section 4.4, we then look at the full quantum model. Finally, we discuss the results in Section 4.5 before drawing conclusions in Section 4.6.

## 4.2 Model

The system consists of a large number, $N$, of two-level systems coupled by dipole interactions in 1D under a uniform external driving field, which is detuned from resonance, and interacting with an electromagnetic environment which causes decay. Under the Born and Markov approximations, the dynamics of the system are then

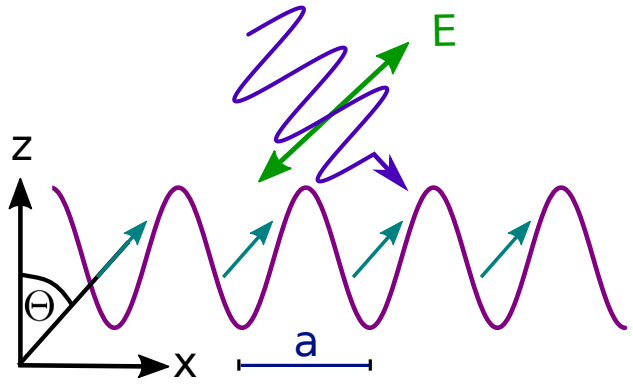


**Figure 4.1** A schematic of a 1D array of atoms or polar molecules under an external drive. The electric field, shown by the green arrow, is oriented at an angle Θ to the z axis and controls the orientation of the dipoles. The lattice spacing is denoted by a.

described by the following master equation

$$\frac{d\hat{\rho}_N(t)}{dt} = -i\left[\hat{H}, \hat{\rho}_N(t)\right] + \frac{\Gamma}{2}\sum_i^N \left[2\hat{\sigma}_i^- \hat{\rho}_N(t)\hat{\sigma}_i^+ - \left\{\hat{\sigma}_i^+\hat{\sigma}_i^-, \hat{\rho}_N(t)\right\}\right], \tag{4.1}$$

where the single atom decay rate, Γ, is defined in Eq. (2.21). Provided $\Gamma > 0$, then Eq. (4.1) describes decay of the excited state, driven by the operators $\hat{\sigma}_i^-$. The Hamiltonian is given by

$$\hat{H} = \frac{\Omega}{2}\sum_i^N \hat{\sigma}_i^x - \frac{\Delta}{2}\sum_i^N \hat{\sigma}_i^z + \sum_{\substack{i,l \\ i\neq l}}^N \frac{J}{4r_{il}^3}\left[\cos\alpha\hat{\sigma}_i^z\hat{\sigma}_l^z + \sin\alpha\left(\hat{\sigma}_i^y\hat{\sigma}_l^y + \hat{\sigma}_i^x\hat{\sigma}_l^x\right)\right], \tag{4.2}$$

where the detuning is given by $\Delta = \omega - \omega_0$, where $\omega$ is the drive frequency and $\omega_0$ the two-level transition frequency, and the drive strength is set by the Rabi coupling Ω. The dipole-dipole interaction is given as in the previous chapter by $J = J_0 a^3(1 - 3\sin^2\Theta)$ where $a$ is the lattice spacing [96] and where we have set $\phi_{il} = 0$ as we will only look at 1D geometries (see Fig. 4.1). Also, as in the previous chapter, the angle Θ is the orientation of the dipoles, with $\Theta = \pi/2$ corresponding to the dipoles lying along the atomic chain. For the remainder of the chapter, we will work with $\Theta = \pi/2$. Other values of Θ will result in a sign change and scaling of the interaction in 1D, but will not lead to significant changes in the types of phases that appear in our system, only in the size of the regions as a function of Δ and Ω. We will also work with $J_0 a^3/\Gamma = -5$ throughout this chapter.

In order to find the long-time steady state of Eq. (4.1), we make a Gutzwiller mean-field approximation which involves taking $\hat{\rho}_N(t) = \otimes\hat{\rho}_i(t)$, where $\hat{\rho}_i(t)$ is a density matrix on site $i$, and effectively ignoring correlations between spins. Then, by taking the trace of Eq. (4.1) over all the sites except a given site $l$, we obtain the equations of motion as

$$\begin{aligned}
\frac{dS_l^x}{dt} &= -\Gamma S_l^x - \Delta S_l^y + 2\sin\alpha \sum_{i(\neq l)}^{N} \frac{J}{r_{il}^3} S_l^z S_i^y - 2\cos\alpha \sum_{i(\neq l)}^{N} \frac{J}{r_{il}^3} S_i^z S_l^y, \\
\frac{dS_l^y}{dt} &= -\Gamma S_l^y - \Omega S_l^z + \Delta S_l^x - 2\sin\alpha \sum_{i(\neq l)}^{N} \frac{J}{r_{il}^3} S_l^z S_i^x + 2\cos\alpha \sum_{i(\neq l)}^{N} \frac{J}{r_{il}^3} S_i^z S_l^x, \\
\frac{dS_l^z}{dt} &= -\Gamma(S_l^z + 1/2) + \Omega S_l^y + 2\sin\alpha \sum_{i(\neq l)}^{N} \frac{J}{r_{il}^3} (S_i^y S_l^x - S_l^y S_i^x),
\end{aligned} \tag{4.3}$$

where $S_l^\beta(t) = \frac{1}{2}\,\mathrm{Tr}\{\hat{\sigma}_l^\beta \hat{\rho}_N(t)\}$ are the spin expectation values, which have their time argument suppressed in Eqs. (4.3). We can see that in the limit $\Gamma \to 0$ and with $\Delta = 0$, we recover the mean-field equations in Eqs. (3.2).

## 4.3 Mean-Field Phase Diagram

We compute the mean-field phase diagram by finding the steady states to Eqs. (4.3) within a bipartite sublattice ansatz, where we split the lattice into two sublattices, A and B. Depending on the parameters, Eqs. (4.3) can result in up to three uniform solutions and three sets of antiferromagnetic solutions. To determine the final phases that exist in the system, we perform linear stability analysis of the resultant solutions. To confirm the sublattice results, we evolve Eqs. (4.3) in time until the long-time limit (up to $t\Gamma = 1000$ for a system size of $N = 100$ with periodic boundary conditions (PBCs)) and also find the resultant phases in regimes where the sublattice ansatz breaks down. For our dynamical simulations, we use either an initial condition of $(S^x, S^y, S^z) = (0, 0, -1/2)$ or, if examining phase instability, the steady state that becomes unstable as the initial condition.

In Fig. 4.2, we show a collection of phase diagrams as a function of $\Delta$ and $\Omega$ for select values of $\alpha$ in the range $0 \leq \alpha < \pi$. Note that for $\pi \leq \alpha < 2\pi$, we will obtain the same phases as for $0 \leq \alpha < \pi$ but with the phase diagram reflected about $\Delta = 0$ due to the sign change in the interaction term. This is also true if the dipoles are tilted out of plane ($\Theta = 0$), although the interaction strength is then scaled by a factor of

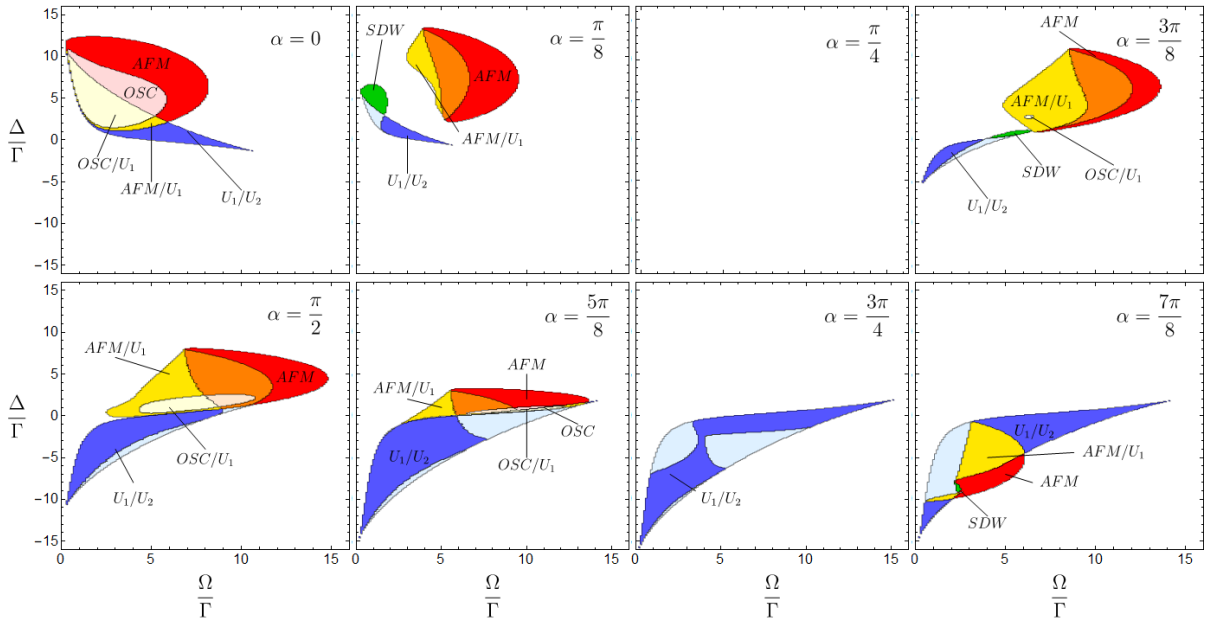


**Figure 4.2** Mean-field phase diagrams as a function of Rabi coupling and detuning, for values of $0 \leq \alpha < \pi$. We find the emergence of four key phases: uniform phases, antiferromagnetic phases, spin density wave phases and oscillatory phases. We also find examples of where these phases can be bistable with one another which means both phases can coexist within the corresponding parameter regime, and which phase the system ends up in depends on the initial conditions. These regions are denoted with double labelling e.g. AFM/$U_1$.

1/2. Therefore, it is sufficient to consider the range $0 \leq \alpha < \pi$ to cover all phases that can occur in the 1D system.

From our phase diagrams, we can see some general features that occur for all or almost all $\alpha$ values. Specifically, we can classify four key phases that emerge in the system. Firstly, for all $\alpha$, there are the spatially uniform phases, which are shown by the white regions in the phase diagrams. At low Rabi drive, the uniform phase has a high spin magnitude and the spins lie in or close to the state $(S^x, S^y, S^z) = (0, 0, -1/2)$. We define this uniform phase as the $U_1$ phase. At high drive, the spin magnitude decreases and the spins lie close to the mixed state, which we denote as the $U_2$ phase. As mentioned in Chapter 2, both of these uniform phases occur for any spin half system even without interactions as they are just general solutions to the optical Bloch equations and are solutions of the full quantum system [95] in the limit of low/high Rabi coupling respectively. For all $\alpha$, the $U_1$ phase smoothly crosses over into the $U_2$ phase for most parameter ranges. However, for $\alpha \neq \pi/4$, when the drive and detuning

are comparable to the interaction strength ($V_{12}/\Gamma \approx -5$), regimes of bistability between the $U_1$ and $U_2$ exist, which lead to sharp transitions between the two phases. Regions of bistability are denoted by the dark blue regions in the phase diagram and which phase the system ends up in within this region depends on the initial conditions. Note that for $\alpha = \pi/4$, we have a Heisenberg Hamiltonian which conserves total spin, and so the uniform phases are the only phases that occur and there is no bistability. The behaviour of the uniform phases is analogous to a liquid-gas phase diagram where the $U_1$ phase can be considered the high density liquid phase and the $U_2$ phase as low density gaseous phase. The first order transition at $|\Delta/\Gamma| \lesssim 1$ and smooth crossover at $|\Delta/\Gamma| \gg 1$ are then similar to the liquid-gas transitions where detuning and Rabi coupling take the role of pressure and temperature respectively.

It is also the case that when the drive and detuning are comparable to the interactions, for all $\alpha \neq \pi/4$, the uniform phases can become unstable to fluctuations, breaking translational invariance and giving rise to non-trivial phases. In the red regions, the uniform phase becomes unstable to fluctuations with a wavevector of $qa = \pi$ and a stable set of antiferromagnetic solutions exist. This results in the emergence of a canted antiferromagnetic (AFM) solution, with the nature of the AFM phases depending on the $\alpha$ value. When the Ising term dominates ($0 \leq \alpha < \pi/4$ and $3\pi/4 < \alpha < \pi$), the AFM solution has the largest deviation between the $S^z$ components. However, when the XY interaction dominates, the AFM solution has the strongest deviation in the $S^y$ components. As well as instabilities to $qa = \pi$, the uniform phases can become unstable to $qa < \pi$ which results in the emergence of a spin density wave (SDW) phase, provided no other stable phase exists. In the SDW phase, shown by the green regions, the spin orientation varies periodically through the lattice with a period set by the instability wavevector, $qa$. The final key phase to emerge are long-time oscillations (OSC), where the effects of the drive dominate over the effects from dissipation. We find all oscillations emerge from the instability of the AFM phase, which undergoes a Hopf bifurcation, and inherit an AFM nature. The oscillations are shown by the light red regions.

In several regions of the phase diagrams, multiple solutions to Eqs. (4.3) coexist, which can lead to bistabilities. In the yellow regions, a stable uniform solution and stable set of AFM solutions exist, which results in AFM/$U_1$ bistability. Similarly, in the light yellow regions, there is an OSC phase which is also bistable to the $U_1$ phase. However, we do find that sometimes the oscillations become unstable and so only the uniform phase exists. We have not marked these regions on the phase diagram. In the

light blue regions, both the $U_1$ phase and $U_2$ phase exist, but one becomes unstable to fluctuations. When simulating the dynamics in these regions, we find only the stable uniform solution exists i.e. there is no $U_1$/SDW phase bistability. Similarly, in the orange regions, there exist both a uniform phase and an antiferromagnetic phase, but the uniform phase is unstable. We find when simulating the dynamics in this region that only the AFM phase exists, although the AFM phase is frustrated, with the amount of frustration depending on the initial conditions. Likewise, in the light orange regions, there is an OSC phase and an unstable uniform phase. We find only the OSC phase exists, and again that there are frustration effects. As one final note on the phase diagrams, we find that there are no SDW instabilities for $\alpha = 0$. Therefore, it seems that SDW instabilities are inherently related to the XY interaction.

Our phase diagram for $\alpha = \pi/2$ is similar to a pure XY model with nearest-neighbour coupling studied in Ref. [108]. Similarly, our results for $\alpha = 0$ are similar to a nearest-neighbour Ising model studied in Ref. [107].

## 4.4 Quantum Phase Diagram

Having calculated the phase diagram at mean-field level, we now examine how it compares to the phase diagram of the full quantum system to test the validity of the mean-field approximation. To do this, we look at steady states of small quantum systems with $N = 8$ spins and PBCs by finding the zero eigenvalue of the Liouvillian (See Chapter 2). At very low Rabi coupling, we expect the mean-field approximation to capture the full quantum model because the system lies close to the steady state of Eq. (4.1), given by $\hat{\rho}_{ss} = |0\rangle\langle 0|$, where $|0\rangle = \prod_i^N |g_i\rangle$. The spin components are nearly conserved due to the Hamiltonian and $\sum_i^N S_i^z \approx -N/2$. Therefore, single excitations can then be viewed classically due to the large effective spin, allowing the system to be mapped to coupled oscillators. However, for higher Rabi coupling where the interesting phases emerge, quantum effects will be more significant. Mean-field theory is expected to be valid for a higher effective co-ordination number where quantum fluctuations can cancel on average. Therefore our results in 1D are most susceptible to quantum fluctuations. Despite the small system size, we can see some distinct features emerge for the quantum system that reflect the mean-field phases.

We first examine the spin expectation values on each site for a direct comparison to the mean-field results. We find that for the quantum system, the expectation values on each site are uniform, with little to no spatial variation. However, this is likely due

to the small system size and use of PBCs, and that spatial variation in the expectation values would arise for larger quantum systems. If we compare the quantum expectation values to the mean-field expectation values from our phase diagrams in regions where stable uniform phases exist, we find there is good agreement at strong Rabi drive and detuning. This is true for all $\alpha$, especially for $\alpha = \pi/4$, where the expectation values agree exactly for all detuning and Rabi drive. For $\alpha \neq \pi/4$, the difference between the expectation values becomes larger when the drive and detuning are comparable to interactions, particularly in regions where there is $U_1/U_2$ bistability. This is because we find no bistability in the small quantum systems, but a smooth crossover between the $U_1$ and $U_2$ phases. Therefore the quantum expectation values will eventually differ from either choice of the $U_1$ or $U_2$ mean-field solution.

Despite the fact the expectation values seem only to show a single uniform phase, the connected correlators between sites give insight into spatial structure of the fluctuations about the expectation values and possible non-uniform phases that may arise in larger quantum systems. In Fig. 4.3 (1-a), we plot the connected correlator, $\langle \hat{S}_i^z \hat{S}_l^z \rangle_c = \langle \hat{S}_i^z \hat{S}_l^z \rangle - \langle \hat{S}_i^z \rangle \langle \hat{S}_l^z \rangle$, between a site $i$ and its nearest-neighbour for $\alpha = 0$. We find that the connected correlator changes sign between nearest-neighbour sites in the region where where AFM solutions exist in the mean-field, but maintains the same sign when in the uniform region. The insets (1-b) and (1-c) show examples of how the connected correlator varies across the lattice sites for a choice of $\Delta$ and $\Omega$ in the AFM region and in the uniform region, shown by the red and blue circles respectively. We can see how both connected correlators lose long-range order quickly, but maintain an alternating sign in the AFM region, whilst being persistently positive in the uniform region. We find similar results when we plot the $\langle \hat{S}_i^y \hat{S}_l^y \rangle_c$ connected correlator for $\alpha = \pi/2$. The choice of connected correlator is based on the spin component with the strongest deviation from the spatially uniform phase in the mean-field analysis.

While the expectation values and connected correlators give some correspondence to the mean-field picture, we find that within the bistable regions, there is a much stronger signature of the mean-field results given by the index of dispersion (IOD). In regions of bistability, studies [108, 125, 126, 128] have found examples of bimodality in the expectation value distributions when using Quantum Monte Carlo wavefunction methods [129]. This bimodality arises due to the double well nature of the system when there are two stable mean-field solutions. A bimodal distribution means that the IOD, a measure of a distribution's variance normalised by its mean, will peak in regions of bistability. For our phase diagram, bistability brings the greatest change in

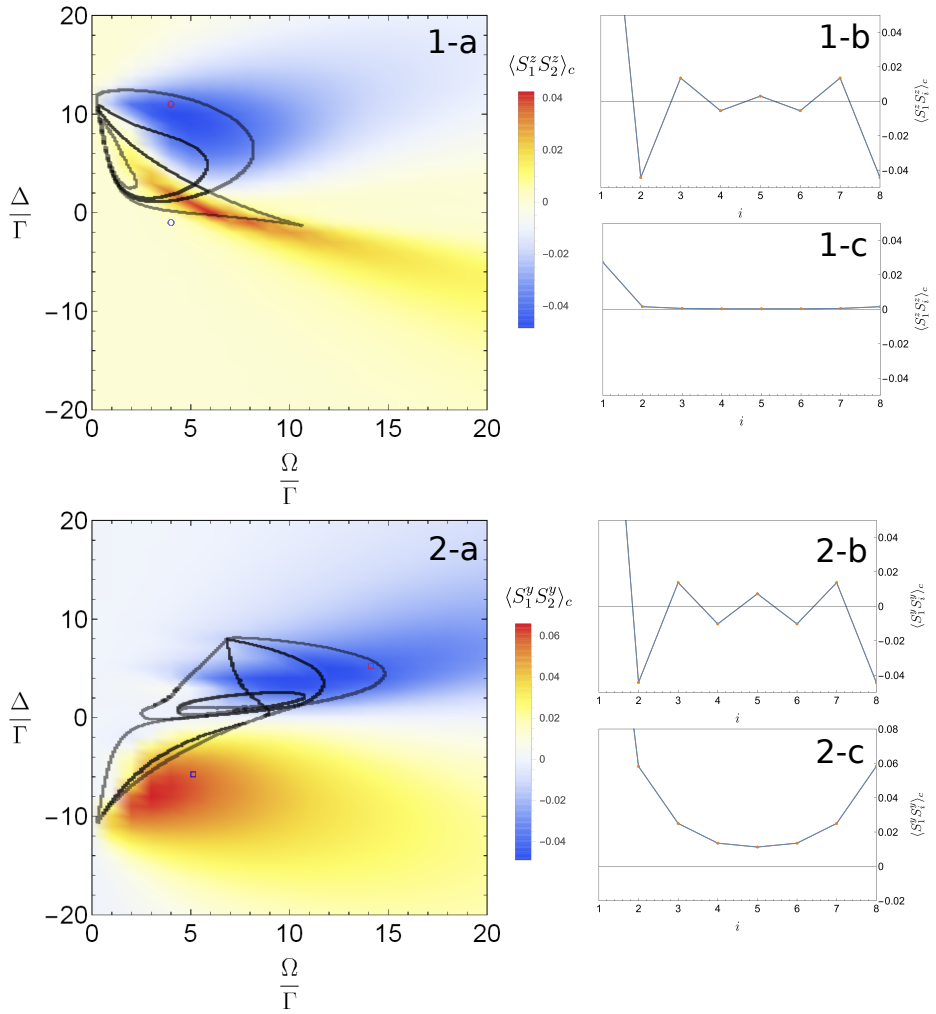


**Figure 4.3** Examples of connected correlators for the quantum system. (1-a) - The $\langle \hat{S}_1^z \hat{S}_2^z \rangle_c$ connected correlator for $\alpha = 0$. We can see the connected correlator becomes negative for nearest-neighbour sites when in the mean-field AFM region. The insets (1-b) and (1-c) show examples of how the connected correlator varies across sites for the red and blue circle respectively. We see that in both cases, long-range order is lost, but the changes of sign are as expected. (2-a) - The $\langle \hat{S}_1^y \hat{S}_2^y \rangle_c$ connected correlator for $\alpha = \pi/2$. Again, we can see that the connected correlator changes sign between nearest-neighbours when in the mean-field AFM region. The insets (2-b) and (2-c) show examples of how the connected correlator varies across sites for the red and blue squares respectively.

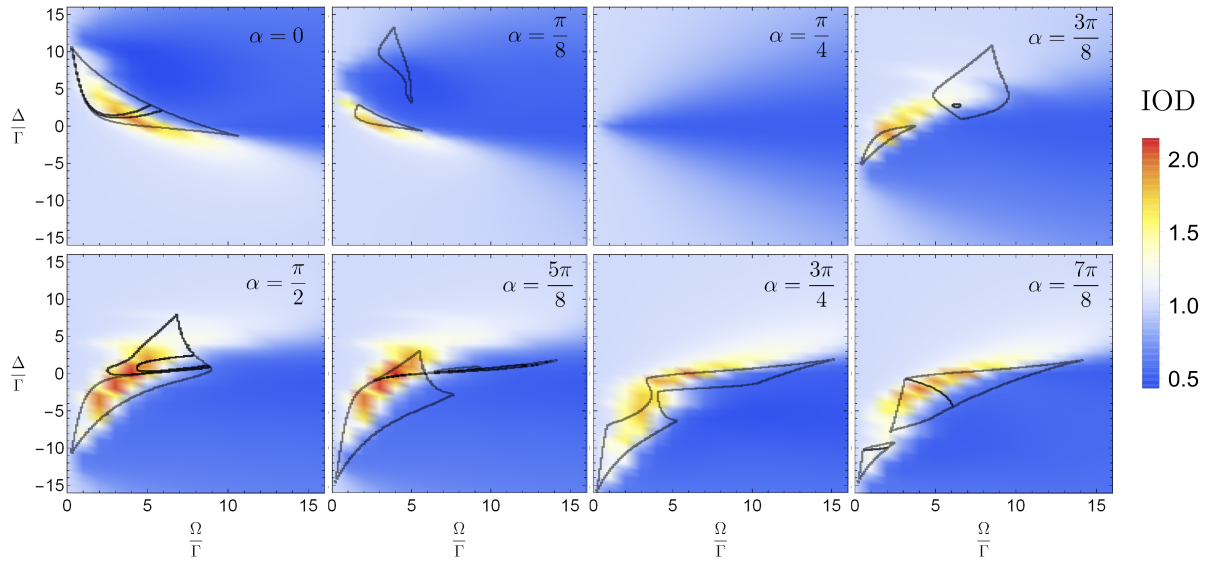


**Figure 4.4** Index of dispersion (IOD) of the number of excitations, $\langle \hat{S}^z \rangle + 1/2$. We see there is an increase in the IOD in regions of bistability, before a quick decrease to 1/2 when entering the region of the $U_2$ phase. The black contours show the regions of our mean-field phase diagram where bistability exists.

$S^z$ values between the two mean-field phases, so we look the index of dispersion of the excitations in the system, give by $\langle S^z \rangle + 1/2$. With this choice of observable, the IOD is given by

$$\mathrm{IOD} = \frac{\sum_{i,l}^{N} \left( \langle \hat{S}_i^z \hat{S}_l^z \rangle - \langle \hat{S}_i^z \rangle \langle \hat{S}_l^z \rangle \right)}{\sum_{i}^{N} \left( \langle \hat{S}_i^z \rangle + 1/2 \right)}. \tag{4.4}$$

In the limit of zero Rabi drive, when $\langle \hat{S}_i^z \rangle = -1/2$, we have IOD = 1, whereas in the limit of high Rabi drive, when $\langle \hat{S}_i^z \rangle \approx 0$, we have IOD = 1/2. In between these two limits, the IOD will either decrease or, when there is a bimodality in the distribution, increase above unity. In Fig. 4.4, we plot the IOD as a function of drive and detuning, marking the areas of mean-field bistability with the black contours. We can see from our figures that the agreement between the fluctuation region and the bistability region is very good for all $\alpha$ values, suggesting that the large peak in the IOD is indeed due to the double well structure of the mean-field solution appearing in the quantum steady state. The results for $\alpha = \pi/2$ have been shown before in [108], but the results for other $\alpha$ are new.

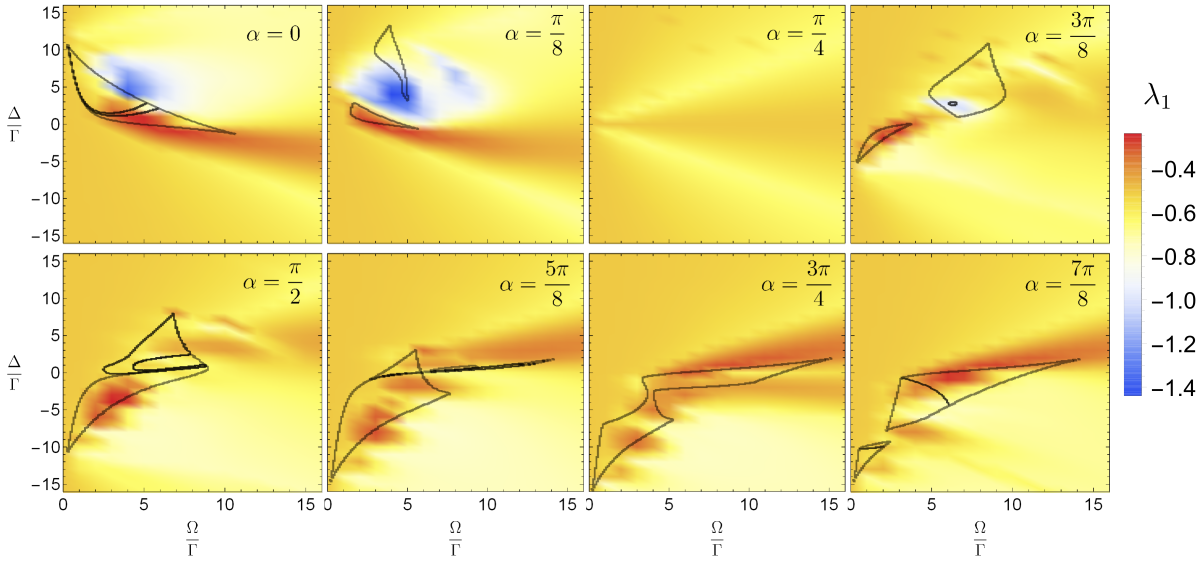


**Figure 4.5** Real part of the spectral gap of the Liouvillian. We see that there is a decrease in real part within the regime of bistability for all $\alpha$, indicating that the spectral gap could close in the limit of large enough quantum systems.

Another signature of bistability should also be evident in spectral gap of the Liouvillian. In systems with true bistability, the spectral gap should close so the system has two steady states. However, for small quantum systems, it is known that the gap will remain finite [124]. Despite this, bistability may occur in very large quantum systems, and if this is to be the case, then we expect the gap to decrease in the region of bistability even for small systems. In Fig. 4.5, we compute [130] and plot the real part of the spectral gap for a system of size $N = 6$. We see there is indeed a decrease in the gap size in the bistability region, with the magnitude of the real part of the eigenvalue dropping below $0.5\Gamma$, which is the spectral gap for a non-interacting system, as found in Chapter 2.

To measure the spectral gap in experiment, one could look at two-time correlators, whose decay depends specifically on the gap in the long-time limit. For two operators, $\hat{A}$ and $\hat{B}$, the two-time correlator is given by

$$\begin{aligned}\langle \hat{A}(t+\tau)\hat{B}(t)\rangle &= \mathrm{Tr}\{\hat{A}e^{(\tau+t-t)\hat{\mathcal{L}}}\hat{B}\hat{\rho}(t)\} \\ &= \mathrm{Tr}\{\hat{B}\hat{\rho}(t)\}\,\mathrm{Tr}\{\hat{A}\hat{\rho}_{ss}\} + \sum_{i=1}^{4^N-1} e^{\lambda_i \tau}\,\mathrm{Tr}\{\hat{L}_i\hat{B}\hat{\rho}(t)\}\,\mathrm{Tr}\{\hat{A}\hat{R}_i\},\end{aligned} \tag{4.5}$$

where in the last line, we have inserted the density matrix expansion given in Chapter 2 in Eq. (2.26), but rewritten in operator form in the original $2^N$ Hilbert space and with the initial condition $\hat{B}\hat{\rho}(t)$. If we allow $t \to \infty$, then Eq. (4.5) simplifies to

$$\begin{aligned}
&\lim_{t\to\infty} \langle \hat{A}(t+\tau)\hat{B}(t)\rangle \\
&= \mathrm{Tr}\{\hat{A}\hat{\rho}_{ss}\}\,\mathrm{Tr}\{\hat{B}\hat{\rho}_{ss}\} + \sum_{i=1}^{4^N-1} \mathrm{Tr}\{\hat{L}_i\hat{B}\hat{\rho}_{ss}\}\,\mathrm{Tr}\{\hat{A}\hat{R}_i\}e^{\lambda_i\tau} \\
&\approx \mathrm{Tr}\{\hat{A}\hat{\rho}_{ss}\}\,\mathrm{Tr}\{\hat{B}\hat{\rho}_{ss}\} + \mathrm{Tr}\{\hat{L}_1\hat{B}\hat{\rho}_{ss}\}\,\mathrm{Tr}\{\hat{A}\hat{R}_1\}e^{\lambda_1\tau},
\end{aligned} \tag{4.6}$$

where in the last line, we have assumed that $\tau$ is large and that $\lambda_1$ is well separated from the rest of the Liouvillian spectrum. This shows how the two-time correlator will decay exponentially with a decay time set by the spectral gap. Therefore, if the spectral gap does decrease in a given parameter regime, we should find that any two-time correlator will have a much longer decay than in regions where the spectral gap is large. In Fig. 4.6, we plot the real part of the second spectral gap of the Liouvillian to see if the first spectral gap is well separated from the spectral bulk. We find for a dominant Ising interaction, there is a separation inside the bistable regime, so measuring the gap from the connected correlator decay should be possible. For a dominant XY interaction, the gap from the bulk is quite small and therefore measuring the gap from the two-time correlator will be harder.

## 4.5 Discussion

We have studied the mean-field phase diagram of an driven-dissipative XXZ model with tunable XY and Ising interaction, finding that the interplay between drive and dissipation leads to four key types of non-equilibrium phases, specifically uniform phases, AFM phases, SDW phases and OSC phases as well as bistabilities between these phases. As discussed in Ref. [106], such a system could be readily implemented with Rydberg atoms or trapped ions, where decay can be controlled by optical pumping. Such systems are also realisable in coupled cavities [108, 131, 132].

The in-depth study of the full quantum system for a small number of spins revealed that the expectation values of the small quantum system agree well with the mean-field uniform phases at strong Rabi drive and detuning, but do not agree as well when the drive and detuning are comparable to the interaction strength. The biggest difference between the mean-field and quantum results is the small quantum system

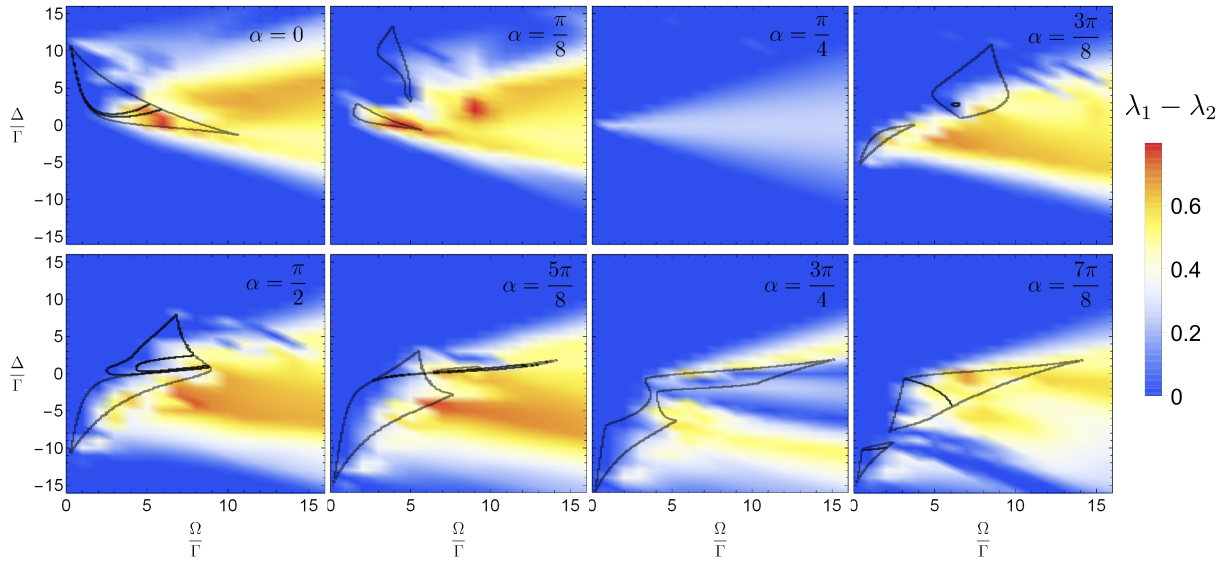


**Figure 4.6** Difference between the spectral gap and the next eigenvalue in the spectrum. We see for a dominant Ising interaction, there is an increase in separation which indicates the spectral gap could be measured from the decay of connected correlators. For an XY dominated interaction, the difference between the real part of the eigenvalues is much smaller and so measuring the gap from the connected correlator will be harder.

does not exhibit any bistabilities, OSC, AFM or SDW phases. However, analysis of the connected correlator shows how fluctuations about these expectation values give signatures of the non-spatially uniform mean-field phases and indicate the possibility of agreement between the mean-field and quantum results for large systems. A much stronger correspondence between the mean-field and quantum results is found when studying the IOD, where we have shown there is good agreement between the region where the IOD of excitations in the system peaks and mean-field bistability. The regular occurrence of this feature in other studies suggests it is a general result for spin-1/2 systems. It would be interesting to see if this is a general feature in any open quantum system exhibiting bistability in its mean-field results. We also showed there was a good agreement between the bistability region and a decreased spectral gap in the Liouvillian, which should be observable by a decrease in the decay times of two-time correlators.

Many of our results here agree with similar studies with nearest-neighbour interactions, both at the mean-field and quantum level, indicating that the power-law nature of the interactions have little effect on the resultant phases. Given this and the fact that the system is 1D, modelling the system with t-DMRG methods [133]

to achieve larger system sizes should be achievable. It would be interesting to see if the quantum fluctuations grow stronger in larger systems and lead to the breaking of spatial uniformity we have seen in our analysis, resulting in a phase diagram closer to our mean-field results. It would also be interesting to study how the IOD peak grows with system size. If the mean-field is expected to become increasingly correct with larger system sizes, then the IOD should drop to zero as the connected correlators in Eq. (4.4) become zero. However, the mean-field is unlikely to become valid for a 1D system, so the behaviour of the IOD is unclear for larger systems. Looking at how the IOD behaves in higher dimensionalities would also be interesting as we expect the mean-field approximation to get increasingly better for higher dimensions. Finally, carrying out finite-size scaling of the Liouvillian gap may indicate if the gap will eventually close in large enough quantum systems and if the separation of the bulk increases.

## 4.6 Conclusions

We have studied the mean-field phase diagram of a driven-dissipative XXZ model with a tunable Ising to XY interaction. We found the emergence of four key types of phase: uniform phases, spin density wave phases, antiferromagnetism and oscillatory phases as well as phase bistabilities. We characterised how the nature of these phases change with changes in the Ising to XY ratio. We then analyse the phases of the corresponding quantum system for small numbers of spins and found that the mean-field results correspond to key features in the quantum phase diagram. We found a strong agreement between peaks in the normalised variance of the $S^z$ expectation values and decrease in the Liouvillian gap to the regions of mean-field bistability and also agreements between connected correlators and spatially varying phases in the mean-field phase diagram.

# Chapter 5

# Phases of driven two-level systems with nonlocal dissipation

## 5.1 Introduction

In the last chapter, we saw how the presence of an environment significantly changed the steady state properties of a quantum system with dipole interactions, and gave rise to new non-equilibrium phenomena. In this chapter, we now focus on a system of polarisable atoms, which lack the static dipole interaction given by the Ising interaction, but have far-field dipole interactions which are long-ranged and dissipative. Of particular interest is the dissipative nature of the far-field dipole interactions, which give rise to nonlocal dissipation, where the decay of one atom is coupled to its neighbours. This leads to several decay modes of the system into the environment. As mentioned in Chapter 1, far-field dipole interactions are a common physical problem when the transitions of the two-level systems are in the optical regime. Therefore, understanding the role of far-field interactions is highly applicable to problems of light-scattering through polarisable media, and can lead to useful applications when the atoms in placed in ordered arrays, such as optical mirrors [93] and excitation storage [92]. It is also important in understanding scattering and light propagation in meta-materials [134] and photonic waveguides [135].

Most work on light scattering focuses on the low light intensity limit, where interactions between excitations are negligible and the mean-field approximation for the dissipative system is valid. However, much less work has been done beyond low intensities, and has been largely limited to small system sizes [126, 136–138]. As seen in the last chapter, at moderate to high intensity drive, these spin systems show novel

phases such as phase bistabilities, antiferromagnetism (AFM), spin density waves (SDW) and even oscillations (OSC) where the spins persistently oscillate despite the presence of dissipation [106, 107].

Here, we study the properties of a driven cold atomic ensemble beyond the regime of low intensity by again employing a numerical mean-field analysis of a large number of two-level systems on a lattice. We establish the open system phase diagram in a 1D geometry and find examples of bistabilities, OSC phases, SDW phases and AFM phases. We also explain how these phases arise due to interactions and the presence of nonlocal dissipation which causes superradiant and subradiant decay, finding key differences in the long-time phases between a system with local and nonlocal dissipation.

This chapter is organised as follows. In Section 5.2 we set up our model. In Section 5.3, we establish the mean field phase diagram with quantum checks in Section 5.4. Finally, in Section 5.5 we discuss our results and possible experimental realisations before drawing conclusions in Section 5.6.

## 5.2 Model

We consider a large number, $N$, of two-level systems fixed in position in a deep 1D optical lattice to form a 1D array. The two-level systems are illuminated with a uniform plane wave and coupled to one another by resonant dipole-dipole interactions. The system is also coupled to the electromagnetic field in free space, which acts as a Markovian environment and allows the dipoles to decay. The resultant Master equation is given by [139, 140]

$$\frac{d\hat{\rho}_N(t)}{dt} = -i\left[\hat{H}_{\text{sys}} + \sum_{\substack{i,l \\ i\neq l}}^{N} V_{il}\hat{\sigma}_i^+\hat{\sigma}_l^-, \hat{\rho}_N(t)\right] + \sum_{i,l}^{N}\frac{\Gamma_{il}}{2}\left[2\hat{\sigma}_i^-\hat{\rho}_N(t)\hat{\sigma}_l^+ - \left\{\hat{\sigma}_l^+\hat{\sigma}_i^-, \hat{\rho}_N(t)\right\}\right], \tag{5.1}$$

where the square brackets represent a commutator, curly brackets represent the anti-commutator. The on-site Hamiltonian is given by $\hat{H}_{\text{sys}} = \Omega/2\sum_i^N \hat{\sigma}_i^x - \Delta/2\sum_i^N \hat{\sigma}_i^z$, where $\Delta = \omega - \omega_0$ is the detuning from the two-level transition energy, $\omega_0$, and $\Omega = 2\mathbf{d}.\mathbf{E}$ is the Rabi coupling determined by the dipole moment vector $\mathbf{d}$ and the electric field vector, $\mathbf{E}$, of an external drive. We consider an experimental set up where the wavevector of the drive, $\mathbf{k}$, is perpendicular to the lattice and the electric field parallel to the lattice so that $\mathbf{E} = E_0\hat{\boldsymbol{x}}e^{-iky}$. The dipole interactions and decay terms

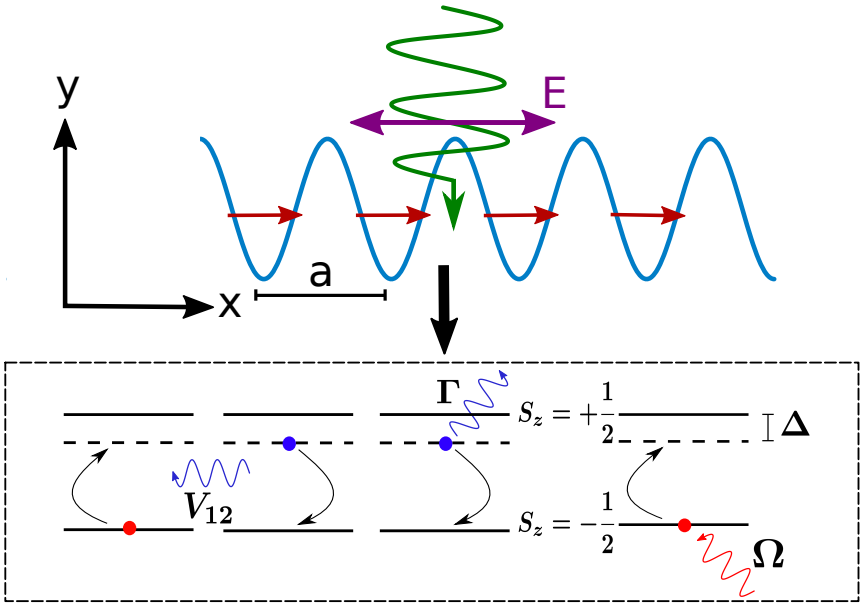


**Figure 5.1** A schematic of a 1D array of atoms under external drive. The electric field, shown by the purple arrow, is oriented parallel to the x axis and controls the orientation of the dipoles shown in red. The lattice spacing is denoted by $a$. The boxed image shows the microscopic picture of two-level systems interacting via photon exchange and dissipation, where the external drive controls the value of the Rabi coupling, $\Omega$.

are then given by

$$\begin{aligned} V_{il} &= -\frac{3\Gamma}{2}\left(\frac{\sin\kappa r_{il}}{(\kappa r_{il})^2} + \frac{\cos\kappa r_{il}}{(\kappa r_{il})^3}\right), \\ \Gamma_{il} &= 3\Gamma\left(-\frac{\cos\kappa r_{il}}{(\kappa r_{il})^2} + \frac{\sin\kappa r_{il}}{(\kappa r_{il})^3}\right), \end{aligned} \tag{5.2}$$

where the single atom decay rate, $\Gamma$, is defined in Eq. (2.21). Note that $\Gamma_{ii} = \Gamma$ so there is local as well as nonlocal dissipation in the system.

The parameter $\kappa a = 2\pi a/\lambda_0$, as mentioned in Chapter 1, is the ratio of the two-level transition wavelength, $\lambda_0$, to the lattice spacing $a$, and is important in determining the nature of the interactions and loss. If we consider $\kappa a \approx 0$, with $a$ fixed, then the system becomes closed, with the interactions reducing to the near-field dipole model of Chapters 3 and 4. If we instead consider $\kappa a \approx 0$, with $\kappa$ fixed, then the interaction strength diverges and dissipation becomes all-to-all with $\Gamma_{il} = \Gamma$. In the opposite limit where $\kappa a \gtrsim 2\pi$, the interactions become negligible and the dissipation becomes local (however, we will later find that $\kappa a \lesssim 1.2$ to observe interesting results). Throughout

the rest of this chapter, we work with $\kappa a = 0.7$ which is well within these limits and allows us to see the effects of nonlocal interactions and dissipation.

Making the Gutzwiller mean-field approximation, $\hat{\rho}_N \approx \otimes \hat{\rho}_i$ and taking the trace of Eq. (5.1) over all the sites except a given site $l$ gives the equations of motion as

$$\begin{aligned}
\frac{dS_l^x}{dt} &= -\frac{\Gamma}{2}S_l^x - \Delta S_l^y - 2\sum_{i(\neq l)}^{N} V_{il} S_l^z S_i^y + \sum_{i(\neq l)}^{N} \Gamma_{il} S_l^z S_i^x, \\
\frac{dS_l^y}{dt} &= -\frac{\Gamma}{2}S_l^y + \Delta S_l^x - \Omega S_l^z + 2\sum_{i(\neq l)}^{N} V_{il} S_l^z S_i^x + \sum_{i(\neq l)}^{N} \Gamma_{il} S_l^z S_i^y, \\
\frac{dS_l^z}{dt} &= -\Gamma(S_l^z + 1/2) - \sum_{i(\neq l)}^{N} \Gamma_{il}(S_i^x S_l^x + S_l^y S_i^y) + \Omega S_l^y - 2\sum_{i(\neq l)}^{N} V_{il}(S_i^y S_l^x - S_l^y S_i^x),
\end{aligned} \tag{5.3}$$

where $S_l^\beta(t) = \frac{1}{2}\,\mathrm{Tr}\{\hat{\sigma}_l^\beta \hat{\rho}_N(t)\}$ are the spin expectation values which have their time argument suppressed in Eqs. (5.3).

## 5.3 Mean-Field Phase Diagram

We can classify the steady states of Eqs. (5.3) and plot a phase diagram as a function of detuning and Rabi coupling. The phase diagram is shown in Fig. 5.2. To calculate the phase diagram, we perform the same steps as in Chapter 4, by finding and analysing the linear stability of all the uniform and antiferromagnetic solutions of Eqs. (5.3) within a bipartite sublattice ansatz. This determines most boundaries in the phase diagram as well as regions of bistability.

We support the stability analysis by time evolving the full dynamics of Eqs. (5.3) to the long-time limit (up to $t\Gamma = 350$) to confirm the uniform and antiferromagnetic phases and also to determine the resultant phase when the uniform or antiferromagnetic phases become unstable. This allows us to define the boundaries between SDW and OSC phases and to check that the wavevector causing instability of the uniform solutions, $q$, has the same periodicity as the SDW phases that emerge in the full dynamics. Finally, whenever the instability wavevector is of the form $qa = 2\pi/n$, where $n$ is a integer with $1 < n \leq 10$, we also simulate the dynamics in a sublattice ansatz, which involves reducing Eqs. (5.3) to $n$ sites which repeat periodically throughout the full lattice. For the time evolution, we simulate system sizes of up to 200 spins with periodic boundary conditions and use an initial condition of $(S^x, S^y, S^z) = (0, 0, -1/2)$, which

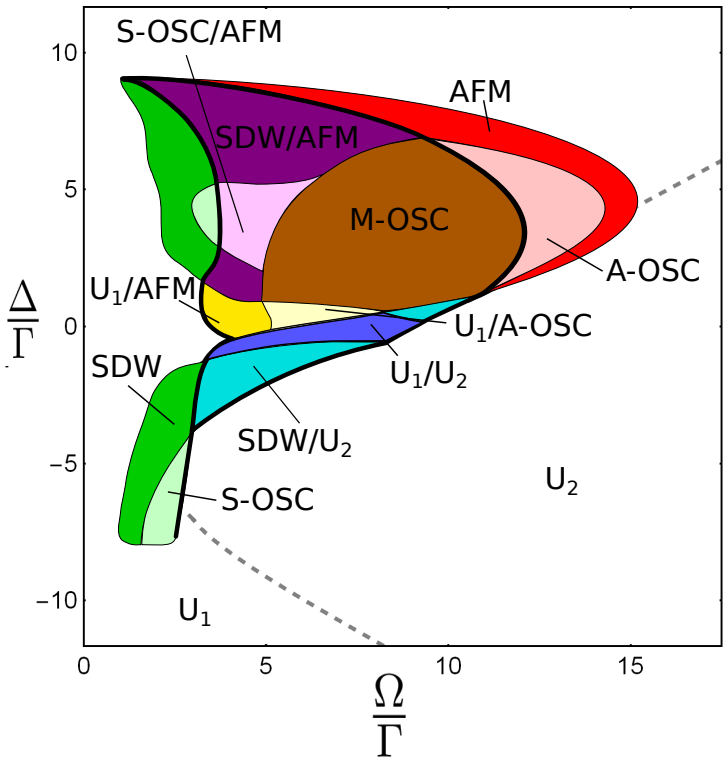


**Figure 5.2** Steady state phase diagram of the system at long times. We find a variety of phases, including AFM, SDW, and OSC. Regions with two labelled phases represent bistability between those two phases. Thin lines represent second order transitions and thick lines enclose regions of bistability within which a first order transition will occur as Rabi coupling is increased. The dashed line represents an arbitrary crossover between the $U_1$ and $U_2$ phases at $S^z = -1/4$, such that we call the region with $S^z < -1/4$ the $U_1$ phase and that with $-1/4 < S^z < 0$ the $U_2$ phase.

is most experimentally relevant as it represents all the atoms in the their groundstate. Throughout the text, $(S^x, S^y, S^z) = (0, 0, -1/2)$ will also define our use of the term 'groundstate'. We do, however, consider other initial conditions in certain regimes to check for bistability.

Our analysis shows that many different long-time phases occur in the system. As expected, we find again the occurrence of spatially uniform phases. At low Rabi coupling, for all detuning values, the system lies close to the groundstate with $S^z \to -1/2$ as $\Omega/\Gamma \to 0$, which we denote as the $U_1$ phase. At high Rabi coupling, the system lies in a state with a small value of $S^z$, where $S^z \to 0$ as $\Omega/\Gamma \gg 1$. We denote this as the $U_2$ phase. At $|\Delta/\Gamma| \gg 1$, the $U_1$ phase smoothly crosses over into the $U_2$ phase as the Rabi coupling is increased. However, when $|\Delta/\Gamma| \lesssim 1$ we find phase a sharp first order transition between the $U_1$ and $U_2$ phases, which occurs within a region of $U_1$-$U_2$ bistability. In Fig. 5.2, for $|\Delta/\Gamma| \gg 1$, we define an arbitrary crossover between the

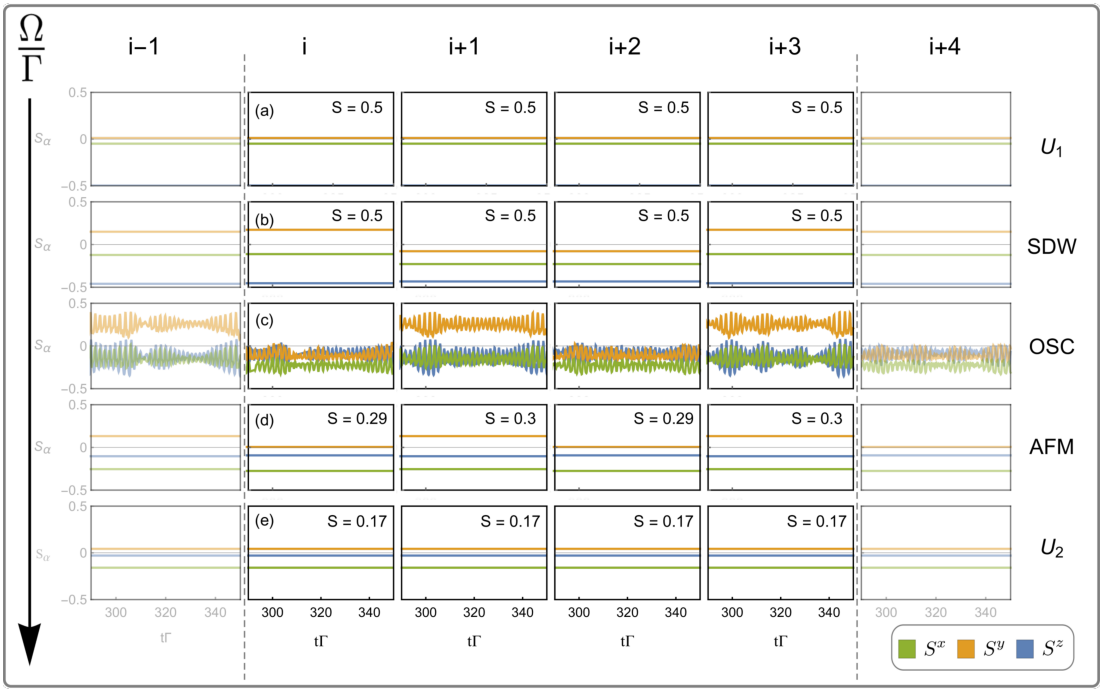


**Figure 5.3** Examples of the spin dynamics for $\Delta/\Gamma = 1.75$ for a series of sites $i$, $i+1$, $i+2$ etc. in the 1D chain. The value, $S = \sqrt{(S^x)^2 + (S^y)^2 + (S^z)^2}$, is the spin magnitude. At low Rabi coupling, there is a spatially uniform $U_1$ phase where the spins lie close to the groundstate. As the Rabi coupling increases, a SDW phase with $qa = 2\pi/4$ develops, then an oscillatory phase and then an AFM phase. Finally, at high Rabi coupling we have the $U_2$ phase where the spins lie in a mixed state and the spin magnitude decreases.

$U_1$ and $U_2$ phases by the condition $S^z = -1/4$, so one can consider the $U_1$ phase to be defined as $S^z < -1/4$ and the $U_2$ phase as $-1/4 < S^z < 0$. When the magnitudes of detuning and Rabi coupling are comparable to the interaction between nearest neighbour sites ($|V_{12}/\Gamma| = 5.32$), we also find additional non-trivial phases, which we now discuss in more detail.

*Negative Detuning* - For $\Delta/\Gamma < 0$, the uniform phase becomes unstable to perturbations with wavevectors in the range $0 < qa < \pi$. This breaks the translational invariance of the system, and results in the formation of Spin Density Wave (SDW) phases, where the spin orientation smoothly changes across the lattice with a period set by the instability wavevector [see Fig. 5.3 (b)]. The magnitude of the instability wavevector, and hence period of the SDW, varies with detuning and Rabi coupling, moving from minimal values of around $2\pi/10$ at strong negative detuning to larger values of around $2\pi/4$ near zero detuning. As well as the $U_1$-$U_2$ bistability mentioned

earlier, we find SDW-$U_2$ bistability, where a first order transition will occur between the SDW and $U_2$ phases. Where this transition occurs and what phase the system ends up in within the bistability region depends on the initial conditions.

Within certain ranges of detuning and Rabi coupling, the SDW phase can develop into an oscillatory (S-OSC) phase which persists into the long-time limit and breaks both spatial symmetry and time-translational symmetry. We found the occurrence of persistent oscillations in the last chapter and also noted that they have been reported in similar studies [106–108]. In contrast to the studies in [106–108] and the last chapter, however, we find that the oscillations here are noisy and appear chaotic, which indicates they are unstable to perturbations. We also find that while the SDW and $U_2$ can be bistable, no such bistability appears to exist between the S-OSC and $U_2$, which is possibly a consequence of the unstable nature of the oscillations. Because no such bistability exists, there is an immediate first order transition between the S-OSC and the $U_2$ phase as Rabi coupling is increased.

*Positive Detuning* - For $\Delta/\Gamma > 0$, we again find the $U_1$ phase becomes unstable to perturbations, forming a SDW. However, whereas for negative detuning the $U_1$ phase only became unstable to one or two perturbations at a time, now the $U_1$ phase becomes unstable to a range of wavevectors as Rabi coupling is increased. The wavevector that causes the largest instability (indicated by the largest positive eigenvalue in the linear stability analysis) determines the period of the resultant SDW. The wavevectors still vary with detuning and Rabi coupling, but are larger than for negative detuning, with values in the range $2\pi/3 \leq qa \leq \pi$. At $qa = \pi$, the SDW becomes a canted AFM phase. We find that in certain regimes, there are additional AFM phases that can be bistable with the SDW phase.

As for negative detuning, we find another oscillatory phase develops across a large range of Rabi coupling and detuning. At low Rabi coupling, noisy oscillations emerge from the SDW, forming an S-OSC phase, whilst at high Rabi coupling, the oscillations have a clear antiferromagnetic order (denoted A-OSC). At intermediate values of Rabi coupling, the oscillations take on a frustrated antiferromagnetic order due to the mixing of SDW and AFM solutions. This is also accompanied by regions of SDW-(A-OSC) bistability or small regions of (S-OSC)-(A-OSC) bistability. We do not show the boundaries between these regions but instead denote this mixture of phases as M-OSC for mixed oscillation. The boundary of the M-OSC region is defined by where the AFM phase becomes unstable or where the SDW phase disappears.

Oscillations for positive detuning with an antiferromagnetic nature were observed in the last chapter and other similar models with local dissipation [108], including a frustrated AFM phase which seems related to our M-OSC phase. However, the S-OSC region appears to be new and also our results show a much larger region of AFM oscillation, with oscillations that contain many beat frequencies. Fig. 5.3 (c) shows an example of the AFM oscillation.

In Fig. 5.4, we show examples of most of the phase transitions occurring within the phase diagram by simulating the full dynamics in the same parameter range as in Fig. 5.3. To study the phase transitions, we calculate the order parameter

$$\sigma = \frac{1}{N}\sum_{i}^{N}(\bar{\mathbf{S}} - \mathbf{S}_i)^2, \tag{5.4}$$

where $\mathbf{S}_i = (S_i^x, S_i^y, S_i^z)/S$, $S = \sqrt{(S_i^x)^2 + (S_i^y)^2 + (S_i^z)^2}$ and $\bar{\mathbf{S}} = \sum_j^N \mathbf{S}_j/N$ is the average spin. We also calculate the order parameter

$$T = \frac{1}{N\tau}\sum_{i}^{N}\int_0^\tau (\mathbf{S}_i(t_f) - \mathbf{S}_i(t_f + t))^2 dt, \tag{5.5}$$

where $\tau = 200/\Gamma$ and $t_f = 700/\Gamma$, which is well into the long-time limit. The order parameter $\sigma$ takes non zero values when the phase breaks translational symmetry such as in the SDW phase and $T$ takes non zero values when the phase breaks time-translational symmetry such as in the OSC phase.

We see from Fig. 5.4 that the SDW phase emerges via a second order transition from the $U_1$ phase and then becomes unstable via another second order transition to form an S-OSC phase. The S-OSC phase then undergoes a first order transition to the A-OSC phase within the M-OSC region, leading to a sharp jump in $\sigma$ and a discontinuity in $T$. As the Rabi coupling increases, the frustration in the A-OSC phase decreases which leads to an increase in the temporal order parameter. Eventually, the OSC phase transitions to the AFM phase, which then disappears via another second order transition to the $U_2$ phase. Note that the order parameters shown here won't show a transition crossing into the M-OSC region because the M-OSC boundary is determined by when the AFM solution becomes unstable as determined by the linear stability analysis.

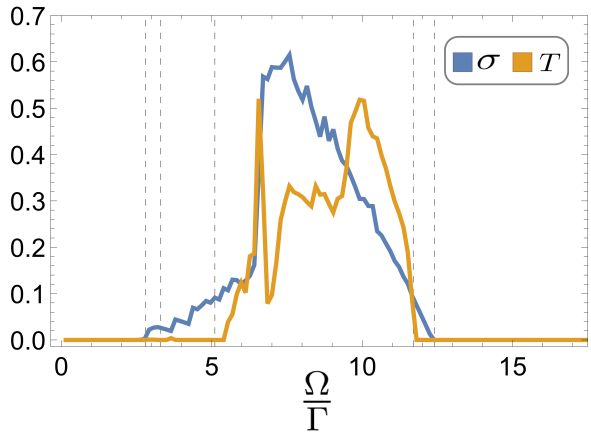


**Figure 5.4** Evolution of the order parameters $\sigma$ and $T$, given by Eqs. (5.4) and (5.5) respectively, as a function of Rabi coupling for $\Delta/\Gamma = 1.75$. The SDW phase emerges via a second order transition from the $U_1$ phase at $\Omega/\Gamma = 2.8$. (Note the jagged structure at low Rabi coupling is a finite size effect, owing to competing SDW wave vectors.) The SDW then forms into an S-OSC phase and later undergoes a first order transition at $\Omega/\Gamma = 6.6$ to the A-OSC phase within the M-OSC region. As the Rabi coupling is increased, the system moves to the AFM phase, where a further second order transition occurs between the AFM and $U_2$ phase at $\Omega/\Gamma = 12.4$. The dashed lines indicate the crossings into the SDW, SDW/AFM, OSC, AFM and $U_2$ regions respectively.

## Explanation of Features

Many aspects of the phase diagram presented here are found also for the case of $\alpha = \pi/2$ for the near-field dipole model in Chapter 4 and also for a nearest neighbour XY model with local dissipation, studied in Ref. [108]. However, there are also clear differences that arise due to the long range interactions and nonlocal dissipation. In particular, we find larger regimes of uniform phase instability at low Rabi coupling, which leads to a greater emergence of spin density waves. To understand this difference more, we study the stability of the uniform phases for systems with local and nonlocal dissipation.

To determine the uniform phases in the systems with local and nonlocal dissipation, we solve the equations of motion, Eqs. (5.3), for the uniform picture, such that $S_i^\beta = S^\beta$,

which allows us to obtain the following cubic polynomial

$$\begin{aligned} &8\left(\frac{\epsilon_\Gamma(0)^2}{4}+\epsilon_V(0)^2\right)(S^z)^3 \\ &+4\left(\frac{\epsilon_\Gamma(0)^2}{4}+\epsilon_V(0)^2+2\Delta\epsilon_V(0)-\Gamma\epsilon_\Gamma(0)\right)(S^z)^2 \\ &+\left(2\Delta^2+\frac{\Gamma^2}{2}+\Omega^2+4\Delta\epsilon_V(0)-\Gamma\epsilon_\Gamma(0)\right)S^z \\ &+\Delta^2+\Gamma^2/4=0, \end{aligned} \tag{5.6}$$

where $\epsilon_V(0) \equiv \sum_{l\neq 0}^{N} V_{l0} = -12.4\Gamma$ and $\epsilon_\Gamma(0) \equiv \sum_{l\neq 0}^{N} \Gamma_{l0} = 2.9\Gamma$. The discriminant of a cubic given by $ax^3+bx^2+cx+d$ is $b^2c^2-4ac^3-4b^3d-27a^2d^2+18abcd$. By substituting in for a, b, c and d, we can determine the number of real roots, and hence steady state solutions, of Eq. (5.6). If the discriminant is greater than zero, there are three solutions, while if it is less than zero, there is only one solution. Using this, we can easily find the region of multiple uniform solutions and how the area of this region changes as a function of lattice spacing. To look at the solutions for local dissipation only, we set $\epsilon_\Gamma(0)=0$ in Eq. (5.6). Once we have obtained the uniform solutions, we check their stability to linear perturbations by linearising Eqs. (5.3) about the uniform steady state, which gives us the matrix equation Eq. (5.7). Once again, to look at local dissipation only, we set $\epsilon_\Gamma(0)=0$ in Eq. (5.7).

Fig. 5.5 shows the instability of the uniform state for a system with local and nonlocal dissipation with the black line showing the region where three uniform solutions exist. Within this region, we show the instability of only one uniform solution (the $U_1$ phase) as one solution is always stable (the $U_2$ phase) and the other unnamed phase is always unstable to perturbations with wavevector $qa=0$. We see that both systems share similarities, such as the region of multiple uniform solutions occurring at negative detuning and the same overall shape of the instability-$U_2$ crossover. The asymmetry of the phase diagram structure across the detuning range is due to the interactions, which results in a mean-field shift of the two-level transition energy. Both bistability and smallest increase in Rabi coupling needed to move from $U_1$ to $U_2$ occurs when the detuning begins to compensate for the energy shift from the interactions, bringing the drive back on resonance again. This is perhaps easiest to see from Eqs. (5.3), where in the uniform picture $dS^{x/y}/dt \sim \pm(\Delta+2S^z\epsilon_V(0))S^{y/x}$. Considering that $-1/2 \leq S^z \leq 0$, we see resonance occurs when $\Delta/\Gamma \leq 0$. Specifically for the

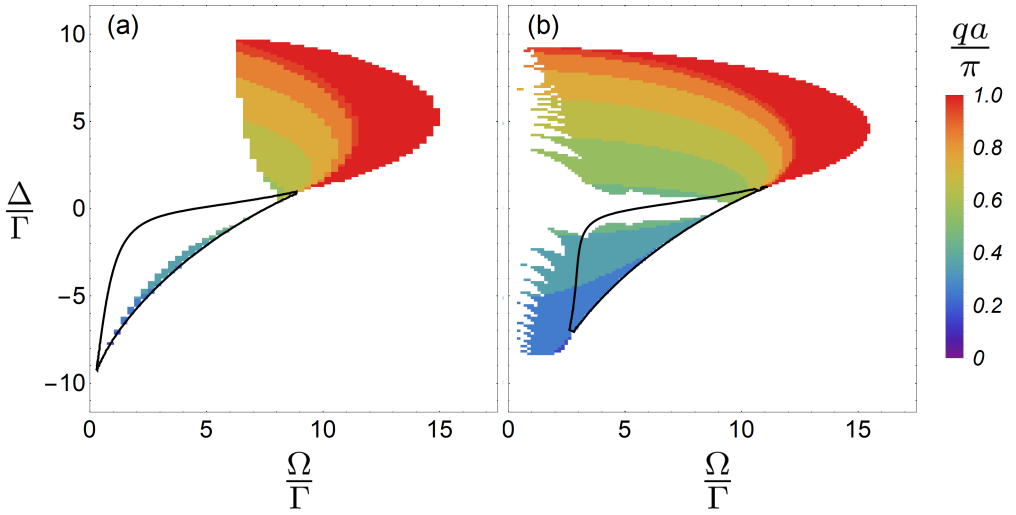


**Figure 5.5** Plot of the instability wavevector of the uniform solution for systems with (a) local dissipation and (b) nonlocal dissipation. The colour represents the magnitude of the wavevector as a multiple of $\pi$ and the black line encloses the region where multiple uniform solutions exist. We can clearly see that the system with nonlocal dissipation has a larger range of instability than the system with local dissipation at lower Rabi coupling. Note that the 'finned' structure at low Rabi coupling is a finite size effect.

$S^z = -1/4$ contour in the phase diagram, resonance occurs at $\Delta/\Gamma = -6.2$ which is approximately where the lowest Rabi coupling is needed to cross the contour.

In both systems, we find also that SDW and AFM phases can form, with a similar arrangement of instability wavevectors for positive and negative detuning. However, for the system with nonlocal dissipation, the SDW/AFM regions are larger and extend to lower Rabi coupling. To explain this, we elaborate on the linear stability analysis of the uniform phases. By linearising Eqs. (5.3) about a uniform steady state, we find the resultant matrix equation to be given by

$$\frac{d}{dt}\begin{pmatrix}\delta S^z\\ \delta S^y\\ \delta S^x\end{pmatrix} = \begin{pmatrix}-\Gamma & \Omega + f(q) & g(q)\\ -\Omega + h & -\tilde{\Gamma}(q)/2 & \tilde{\Delta}(q)\\ I & -\tilde{\Delta}(q) & -\tilde{\Gamma}(q)/2\end{pmatrix}\begin{pmatrix}\delta S^z\\ \delta S^y\\ \delta S^x\end{pmatrix}, \tag{5.7}$$

where $f(q) = -S^y(\epsilon_\Gamma(0) + \epsilon_\Gamma(q)) - 2S^x(\epsilon_V(q) - \epsilon_V(0))$, $h = S^y\epsilon_\Gamma(0) + 2S^x\epsilon_V(0)$, $g(q) = -S^x(\epsilon_\Gamma(q) + \epsilon_\Gamma(0)) - 2S^y(\epsilon_V(0) - \epsilon_V(q))$ and $I = -2S^y\epsilon_V(0) + S^x\epsilon_\Gamma(0)$. The functions $\epsilon_V(q) = \sum_{l\neq 0}^{N} V_{l0}\exp(iqr_{l0})$ and $\epsilon_\Gamma(q) = \sum_{l\neq 0}^{N}\Gamma_{l0}\exp(iqr_{l0})$ are the dispersion relations, with $\epsilon_V(0)/\Gamma = -12.4$ and $\epsilon_\Gamma(0)/\Gamma = 2.9$ for our system, and $q$ being the

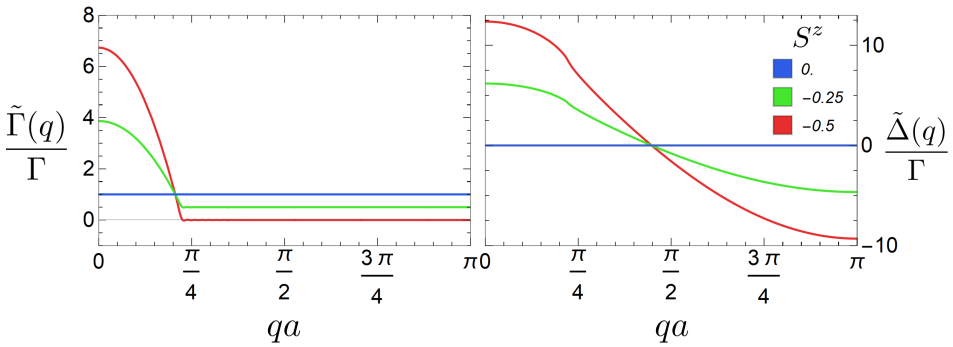


**Figure 5.6** Effective damping and detuning of the $S^{x/y}$ fluctuations for different values of $S^z$. While modification of the detuning by interactions occurs for any system with interactions, the modification of the decay rate is a consequence of nonlocal dissipation. We see that the effective damping quickly becomes subradiant for higher values of $qa$, but eventually becomes equal to the onsite decay as $S^z$ increases.

momentum fluctuation. Note that the $q$ used here is the same $q$ used to classify the SDW phases earlier in the text.

From Eq. (5.7), we see that the interactions modify the detuning, resulting in $\tilde{\Delta}(q) = \Delta + 2S^z\epsilon_V(q)$. We also see that whilst the nonlocal dissipation alters the off-diagonal elements of the matrix, the crucial difference is the fluctuations in $S^{x/y}$ have an effective damping, $\tilde{\Gamma}(q)/2 = \Gamma/2 - S^z\epsilon_\Gamma(q)$. This effective damping is a direct consequence of the nonlocal dissipation and cannot occur in a system with local dissipation, where the $S^{x/y}$ fluctuations would always experience a fixed decay rate of $\Gamma/2$.

In Fig. 5.6, we plot $\tilde{\Gamma}(q)$ and $\tilde{\Delta}(q)$ as functions of wavevector, $q$, for different values of $S^z$. Focusing on $\tilde{\Gamma}(q)$, we see that it quickly drops to minimal values for $qa \geq 2\pi/10$, which means the $S^{x/y}$ fluctuations experience a subradiant decay rate. By having a reduced dissipation, fluctuations can grow at much lower Rabi coupling compared to the local dissipation model, resulting in instabilities and the formation of SDW phases. The fact that high momentum fluctuations are subradiant can be understood as a result of destructive interference between the dipoles, which begin to oscillate out of phase, inhibiting photon emission and therefore trapping excitations in the system. As the Rabi coupling is increased, $S^z$ will decrease in value and $\tilde{\Gamma}(q)$ eventually tends to $\Gamma$. This results in the similarity between the local and nonlocal dissipation instability plots at higher Rabi coupling, as the effects of nonlocal dissipation become negligible.

Examining the characteristic polynomial from the matrix in Eq. (5.7) gives more insight into the phase diagram structure. We find that stability of the uniform solution is determined by the sign of the expression

$$\begin{aligned} A_0 =& \frac{\tilde{\Gamma}}{2}\left[\frac{\tilde{\Gamma}(q)}{2}\Gamma + \Omega(\Omega - h + f(q)) - Ig(q) - f(q)h\right] + \\ & \tilde{\Delta}(q)\left[\tilde{\Delta}(q)\Gamma - \Omega(I + g(q)) + g(q)h - If(q)\right]. \end{aligned} \tag{5.8}$$

To show this, let us write the characteristic polynomial of the matrix in Eq. (5.7) explicitly as $A_3\lambda^3 + A_2\lambda^2 + A_1\lambda + A_0$. We can formulate the Routh array of the characteristic polynomial and determine stability of the uniform solutions from the polynomial coefficients, without explicitly having to solve the cubic [141]. The Routh array is given by

| | |
|---|---|
| $A_3$ | $A_1$ |
| $A_2$ | $A_0$ |
| $\frac{A_2A_1 - A_0A_3}{A_2}$ | 0 |
| $A_0$ | 0 |

For stability, $A_2$, $A_1A_2 - A_0A_3$ and $A_0$ all need to be greater than zero for the solution to be stable. If any of the coefficients change sign, then the solution becomes unstable. Also, if $A_1A_2 - A_0A_3$ changes sign, then the system undergoes a Hopf bifurcation as we have a row of zeroes with no sign change on either side of the row. We find numerically this does not happen for the uniform solution, so does not need to be considered further. From the matrix equation, Eq. (5.7), we can calculate the values $A_0$ to $A_3$ which are given by

$$\begin{aligned} A_3 =& 1, \\ A_2 =& \Gamma + \tilde{\Gamma}(q), \\ A_1 =& \frac{\tilde{\Gamma}(q)}{2}\left(\frac{\tilde{\Gamma}(q)}{2} + 2\Gamma\right) + \Omega(\Omega - h + f(q)) \\ & + \tilde{\Delta}(q)^2 - Ig(q) - f(q)h, \\ A_0 =& \frac{\tilde{\Gamma}}{2}\left[\frac{\tilde{\Gamma}(q)}{2}\Gamma + \Omega(\Omega - h + f(q)) - Ig(q) - f(q)h\right] + \\ & \tilde{\Delta}(q)\left[\tilde{\Delta}(q)\Gamma - \Omega(I + g(q)) + g(q)h - If(q)\right]. \end{aligned} \tag{5.9}$$

We find that $A_2$ and $A_1A_2 - A_0$ are always greater than zero, so stability is given by $A_0$ only.

Having established that the stability of the uniform solution is given by $A_0$, we look at Eq. (5.8) in more detail. We see that the expression in the first set of brackets is multiplied by $\tilde{\Gamma}(q)$. If $\tilde{\Gamma}(q) \approx 0$, this means the sign of $A_0$, and hence the stability of the uniform solution, is determined by the sign of $\tilde{\Delta}(q)$ and the expression $\tilde{\Delta}(q)\Gamma - \Omega(I + g(q)) + g(q)h - If(q)$. By looking at the dispersion $\epsilon_V(q)$ plotted in Fig. 5.6, we can see that the sign of $\tilde{\Delta}(q)$ depends on the value of the detuning and the momentum wavevector. If the detuning is positive, then only wavevectors between $2\pi/4 < qa < \pi$ can cause $\tilde{\Delta}(q) < 0$ and hence instabilities, whereas if the detuning is negative, then only wavevectors with $0 < qa < 2\pi/4$ can cause instabilities. This therefore explains the ordering of spin density waves for negative and positive detuning.

We also found the emergence of two OSC phases in our phase diagram, one for $\Delta/\Gamma > 0$ and one for $\Delta/\Gamma < 0$. As mentioned earlier, aspects of the OSC phase for $\Delta/\Gamma > 0$ were seen in the near-field dipole model with local dissipation, whereas the OSC phase for $\Delta/\Gamma < 0$, which occurs on the SDW-$U_2$ boundary, is new and a consequence of nonlocal dissipation. We would intuitively expect oscillations to occur on the boundaries between two phases with different spin orientations where the orientation of the spins is susceptible to change direction [106] and so can be easily driven. Therefore, this new OSC phase is linked to the emergence of the SDW phases at negative detuning.

The oscillations within this phase appear to be noisy and chaotic. We study the emergence and dynamics of the oscillations in more detail by employing a sublattice ansatz. Analysing the stability of the sublattice solution, we determine that the oscillations arise from Hopf bifurcations [142] in the SDW phase, which lead to stable limit cycles. Checking the stability of these limit cycles using classical Floquet analysis, we find that they become unstable to perturbations with wavevectors not allowed in the sublattice system. Whilst the underlying cause of this is unclear in detail, one can imagine that if one were to drive and populate several highly subradiant modes, then the system would behave as a closed driven XY model with dipole couplings which we showed to have unstable noisy oscillations in Chapter 3.

We now focus on the OSC phases for $\Delta/\Gamma > 0$, again employing a sublattice ansatz and Floquet analysis. We find at low Rabi coupling, the SDW phase can become unstable, giving rise to oscillations that are mostly noisy and chaotic, just as for the OSC phase at $\Delta/\Gamma < 0$. However, there are additional AFM phases for

positive detuning that can be bistable with the SDW and S-OSC phases and these AFM solutions also become unstable as the Rabi coupling is increased. This gives rise to the M-OSC phase where both forms of oscillation can mix or the SDW and A-OSC phases mix. There are also regimes of SDW-(A-OSC) bistability and (S-OSC)-(A-OSC) bistability. As the wavevector of the SDW tends to $\pi$ with increasing Rabi coupling, eventually only the A-OSC phase exists. Therefore we find that nonlocal dissipation gives rise to two components for the OSC phase; firstly, the emergence of an S-OSC phase which does not occur in the system with local dissipation and secondly a region of an A-OSC phase which is much larger than in the system with local dissipation.

## 5.4 Beyond Mean Field

We have employed a mean-field approximation to compute the long-time steady state phases of our system. As discussed in the last chapter, we do not expect the mean-field approximation to hold for small quantum systems beyond low Rabi drive as quantum fluctuations become significant. This is especially true in 1D as the coordination number between lattice sites is low, although long-range interactions help increase the effective co-ordination number. However, we have shown that despite this, mean-field theory can still capture some aspects of the full quantum system. We now discuss these features to assess how much of the mean-field is captured by small quantum systems.

In regimes where mean-field theory predicts bistability, we still expect a unique steady state in the full quantum system with far-field dipole interactions [124] and a smooth crossover between the $U_1$ and $U_2$ phases [121] rather than a sharp transition. Looking at the index of dispersion, as defined in Eq. (4.4), we look for signatures of mean-field bistability. Fig. 5.7 shows a plot of the IOD for a system of $N = 10$ spins with periodic boundary conditions. We find a peak in the IOD near the onset of both bistability regions. Similar results have been seen in [126] for the uniform bistability region. We also calculate the connected correlator, $\langle S_i^y S_l^y \rangle_c \equiv \langle S_i^y S_l^y \rangle - \langle S_i^y \rangle \langle S_l^y \rangle$, for $N = 10$ spins on a chain with periodic boundary conditions. The choice of the $S^y$ components is because they show the strongest spin deviation in the mean-field picture, similar to the near-field model. In Fig. 5.8, we plot $\langle S_1^y S_2^y \rangle_c$ across the entire phase diagram, although the same results hold for any spin in the chain due to translational symmetry. Our results show that the correlations lose long range order, but take an antiferromagnetic nature for $\Delta/\Gamma > 0$. For $\Delta/\Gamma < 0$, spins become more positively correlated with their nearest neighbours in the region where the uniform phase persists,

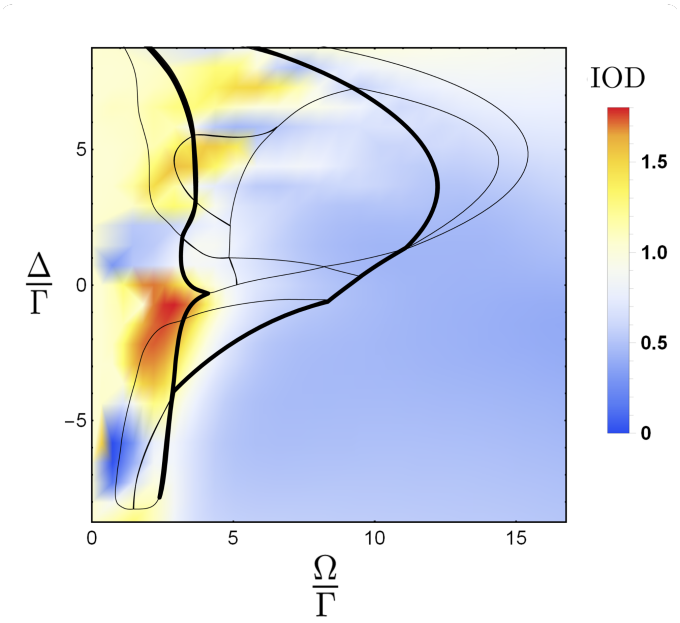


**Figure 5.7** IOD for $N = 10$ spins with periodic boundary conditions. The IOD peaks at the onset of bistability.

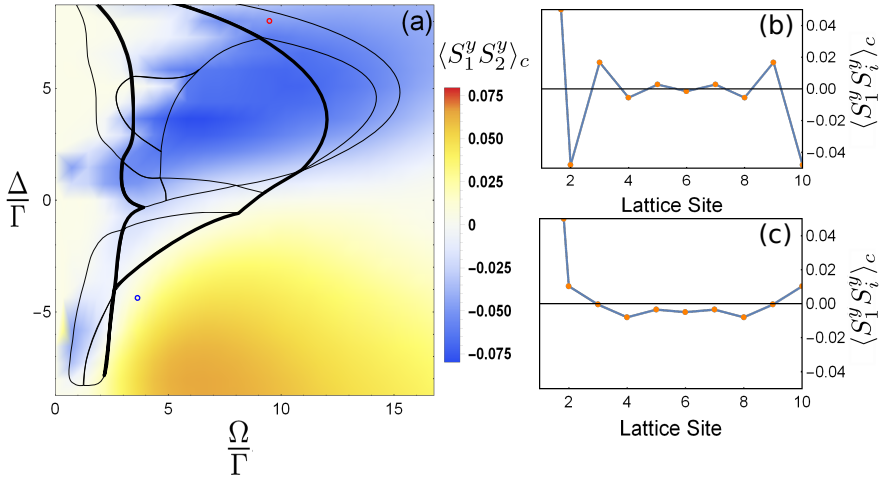


**Figure 5.8** (a) Connected correlator $\langle S_1^y S_2^y \rangle_c$ as a function of Rabi coupling and detuning for $N = 10$ spins on a chain with periodic boundary conditions. We see the correlation is negative for $\Delta/\Gamma > 0$ and positive for $\Delta/\Gamma < 0$. The black lines show the mean-field phase diagram boundaries. The insets (b) and (c) show examples of $\langle S_1^y S_i^y \rangle_c$ along the spin chain at the points indicated by the red and blue circles in (a) respectively.

which agrees with the mean-field phase diagram. Therefore our quantum checks indicate that aspects of the mean-field theory still persist in smaller quantum systems as was the case in Chapter 4.

## 5.5 Discussion

We have explored the phase diagram of an ensemble of two-level systems under an external drive and with resonant far-field dipole-dipole interactions. We have found the emergence of SDW, AFM and OSC phases and phase bistabilities, and determined how the formation of these phases relates to nonlocal dissipation. To realise such a system experimentally, Sr atoms can be used, with the two-level transition between the ${}^3P_0$ and ${}^3D_1(m = 0)$ levels [21]. This transition has a transition wavelength of $\lambda = 2.6\mu$m and would require a lattice spacing of $a = 289.6$nm to achieve $\kappa a = 0.7$. Other lattice spacings and atomic species may be used, as we expect many of our results to extend to nearby values of $\kappa a$. We do find however, that beyond a certain lattice spacing, the interaction between spins becomes insignificant. A good indicator of where this cut off occurs can be determined by looking at the region of multiple uniform solutions, enclosed by the black line in Fig. 5.5. In Fig. 5.9, we plot how the area of this region changes as a function of $\kappa a$. We find that as $\kappa a$ increases, the area decreases and eventually disappears at $\kappa a \approx 1.2$. Beyond this limit, we expect only uniform phases to exist.

In our simulations, we evolved the system to times of $t\Gamma = 350$ or greater to reach the steady state. It may be the case that some phases we find are metastable with a very long decay time. Furthermore, the majority of our simulations were carried out for an initial condition of all the spins in the groundstate, though we did use other initial conditions to examine regions of bistability. We believe our analysis accounts for the majority of phases that exist in the system, but there may be other bistable/multistable phases not captured in our phase diagram that can occur for other initial conditions. Finally, we have only considered 1D systems under uniform driving. It would be interesting to see what features change in higher dimensions, different geometries and under non-uniform driving given the presence of nonlocal dissipation. While our quantum results indicated some aspects of the mean-field theory should be observable, it would also be of interest to study the full quantum system in more detail and quantify where the mean-field theory approximation may fail.

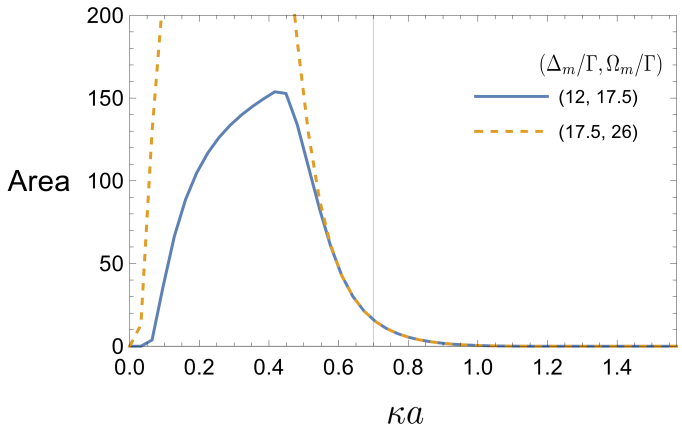


**Figure 5.9** Area of the multiple uniform solution region (shown enclosed by the black line in Fig. 5.5) as a function of lattice spacing. For $\kappa a \geq 1.2$, the area is nearly zero and we expect only uniform phases to exist beyond this limit. It should be noted that at low lattice spacing, the interaction strength diverges, causing the area of multiple uniform solutions to artificially peak and then decrease to zero within any fixed range of $\Delta/\Gamma$ and $\Omega/\Gamma$. We emphasise this by showing two curves for the ranges $-\Delta_m/\Gamma \leq \Delta/\Gamma \leq \Delta_m/\Gamma$ and $0 \leq \Omega/\Gamma \leq \Omega_m/\Gamma$. At higher $\kappa a$ the curves overlap so the cutoff doesn't affect our results. The grey line shows the choice of lattice spacing of $\kappa a = 0.7$ used in this study.

## 5.6 Conclusions

We have studied the mean-field nonlinear dynamics of a 1D chain of two-level systems coupled with dipole-dipole interactions and nonlocal dissipation being driven by an external field. We determined the phases that form in the long-time limit such as antiferromagnetism, spin density waves, oscillations and phase bistabilities. We found that nonlocal dissipation plays a key role in the emergence of these phases by coupling fluctuations in the system to different decay modes and causing a greater formation of spin density and oscillatory phases. We also found that some of the mean-field features persist in the full quantum regime.

# Chapter 6

# Dissipative Bound States

## 6.1 Introduction

Up until now, we have been focused on the long-time steady state of open quantum systems. However, in the last chapter, we saw how nonlocal dissipation resulted in a range of decay rates for a system into the environment. Some of these decay rates were quite small and so reaching the steady state would take a large amount of time. As such, it is also an interesting question to consider the dynamics on the approach to the steady state and find which excitations decay slowest. Furthermore, the dynamics of strongly coupled spin-1/2 systems can be used to explore fundamental issues in the quantum dynamics of many-body systems subject to strong inter-particle interactions.

A famous example of a strong-interaction phenomenon in quantum spins systems is provided by magnon bound states, first proposed by Bethe [143] more than 80 years ago. In this work, it was shown that magnon bound states could form in 1D spin-1/2 Heisenberg chain with nearest-neighbour interactions, lowering their energy compared to free magnons in the system. Subsequent work then extended this result to higher dimensions, anisotropic spin chains and arbitrary spin including solitons [144–147] and spin chains with long-range interactions [148–151]. Furthermore, magnon bound states have been studied in systems with frustration [152], topological structure [153, 154] and in Floquet systems [155, 156]. They have also recently been observed experimentally [63] and shown to have an important role in magnetisation switching [157], transport [158, 159] and to have interesting effects on entanglement entropy [160].

One key aspect in all of these studies is that the system is closed and so the question of bound state decay rates is not considered. However, if the system is coupled to an external environment, then the excitations will eventually decay and so it is natural

to ask how long lived these excitations can be. For a system with local dissipation, the decay rate of both free excitations and bound states will be given by $m$ times the local decay rate [161] where $m$ is the number of excitations. However, for systems involving radiative decay, the dissipation typically becomes nonlocal, where a range of decay rates to the environment exist, which are either superradiant (greater than the local decay rate) or subradiant (smaller than the local decay rate). In these scenarios, the relative decay rates of the free excitations and bound states becomes unclear. For example, is it possible for the decay rate of the bound states to be smaller than that of the free magnons?

In this chapter, we address the question of bound state decay rates in systems with nonlocal dissipation. We look at three models with a nearest-neighbour Ising interaction, which is crucial for the bound states to form, and different forms of XY interaction and nonlocal dissipation. The first two models are a nearest-neighbour and next-nearest-neighbour XY interaction for which we can obtain analytical results. The final model is an experimentally achievable setting in which to observe our results with Rydberg dressed atoms coupled to a photonic crystal waveguide.

The layout of this chapter is as follows. In Section 6.2, we derive the equations needed to obtain the energy and decay rate of the free excitations and bound states. In Section 6.3, we show that in general the decay rate of the bound state lies within the two-magnon decay rate continuum. Then in Section 6.4, we obtain the energies and decay rates for the three models. In Section 6.5 we discuss our results and experimental implementation before drawing conclusions in Section 6.6.

## 6.2 Model

We consider a macroscopic number, $N$, of two-level systems fixed in position on a 1D optical lattice with spacing, $a$, and periodic boundary conditions. The atoms interact with an electromagnetic field which acts as an environment for the system. We assume the Markovian and Born approximations, which are valid provided the coupling between the system and environment is weak. These allow us to describe the system using a master equation approach. We will later discuss the validity of this approximation in relation to our results. The resultant master equation is given by

$$\frac{d\hat{\rho}(t)}{dt} = -i\left[\hat{H}, \hat{\rho}(t)\right] + \sum_{i,l}^{N} \frac{\Gamma_{il}}{2}\left(2\hat{\sigma}_i^- \hat{\rho}(t)\hat{\sigma}_l^+ - \left\{\hat{\sigma}_l^+\hat{\sigma}_i^-, \hat{\rho}(t)\right\}\right). \tag{6.1}$$

We require that the eigenvalues of the matrix $\Gamma_{il}$ are all greater than or equal to zero, in order for Eq. (6.1) to describe decay of the excited state, driven by the operators $\hat{\sigma}_i^-$. Then the steady state density matrix is given by $\hat{\rho}_{ss} = |0\rangle\langle 0|$ where $|0\rangle = \prod_i^N |g_i\rangle$. The Hamiltonian is given by

$$\hat{H} = \Delta \sum_i^N \hat{\sigma}_i^z + \sum_{\substack{i,l \\ i\neq l}}^N V_{il}\hat{\sigma}_i^+\hat{\sigma}_l^- + \frac{J_z}{2}\sum_i^N \hat{\sigma}_i^z\hat{\sigma}_{i+1}^z. \tag{6.2}$$

Note that we will assume translational invariance for our system, such that $V_{il}$ and $\Gamma_{il}$ depend only on the relative distance, $r_i - r_j$, where $r_i$ is the coordinate of site labelled $i$. The Hamiltonian in Eq. (6.2) conserves the number of excitations in the system whilst the dissipator allows the excitations to decay. We can therefore talk about the dynamics of few-magnon excitations. To compute the energies and decay rates of one- and two-magnon excitations in our system, we employ a Green's function method.

We first start with the single magnon Green's function, defined as $G(i,j;t) = \mathrm{Tr}\{\hat{\sigma}_i^-(t)\hat{\sigma}_j^+(0)\hat{\rho}(0)\}\Theta(t) = \langle 0|\,\hat{\sigma}_i^-(t)\hat{\sigma}_j^+(0)\,|0\rangle\,\Theta(t)$, where $\Theta(t)$ is the Heaviside step function. We choose the initial condition, $\hat{\rho}(0)$, to be the pure state $|0\rangle\langle 0|$. The single magnon Green's function obeys the following equation

$$\frac{dG(i,j;t)}{dt} - \delta_{ij}\delta(t) = \left(-i\Delta - \frac{\Gamma}{2} + 4iJ_z\right)G(i,j;t) - i\sum_{p\neq j}^N \left(V_{pj} - i\frac{\Gamma_{pj}}{2}\right)G(i,p;t), \tag{6.3}$$

where $\Gamma = \Gamma_{ii}$ is the onsite decay, which is the same for each site due to the translational invariance of the system. Fourier transforming Eq. (6.3) gives the spectrum of the single magnon states from the poles of

$$G(k,\omega) = \lim_{\epsilon\to 0} i(\omega - E(k) + i\epsilon)^{-1}, \tag{6.4}$$

where

$$E(k) = -4J_z + \Delta - \frac{i\Gamma}{2} + \sum_{l=1}^N (2V_{l0} - i\Gamma_{l0})\cos(kl), \tag{6.5}$$

is the single magnon dispersion, with the real part corresponding to the energy and the magnitude of the imaginary part corresponding to the decay rate.

For two magnons, we consider the following Green's function, $G(i,j,l,m;t) = \mathrm{Tr}\{\hat{\sigma}_i^-(t)\hat{\sigma}_j^-(t)\hat{\sigma}_l^+\hat{\sigma}_m^+\hat{\rho}(0)\}\Theta(t)$, which obeys the equation

$$\begin{aligned}
&\frac{dG(i,j,l,m;t)}{dt} - (1-\delta_{ij})\delta(t)(\delta_{il}\delta_{jm}+\delta_{im}\delta_{jl}) = \\
&(-2i\Delta + 8iJ_z - \Gamma - 4iJ_z\delta_{m,l+1})\, G(i,j,l,m;t) \\
&- i\sum_{p\neq l}^{N} J_{pl}G(i,j,p,m;t) - i\sum_{p\neq m}^{N} J_{pm}G(i,j,p,l;t) \\
&+ 2i\delta_{lm}\sum_{p\neq m}^{N} J_{pm}G(i,j,p,m;t),
\end{aligned} \tag{6.6}$$

where $J_{pl} = V_{pl} - i\Gamma_{pl}/2$. This equation can be rewritten as a matrix equation and partially Fourier transformed with $G(r,r',Q,\zeta) = \sum_{R-R'} e^{-i(R-R')Q}\int_{-\infty}^{\infty} G(i,j,l,m;t)e^{i\zeta t}dt$, where we have defined the relative coordinates, $r = r_i - r_j$, $r' = r_l - r_m$ and also the centre of mass coordinates $R = (r_i + r_j)/2$, and $R' = (r_l + r_m)/2$, to give (see Appendix B)

$$G(r,r',Q,\zeta) = \Gamma(r,r',Q,\zeta)h(r) - \sum_{r''}^{N} K(r,r'',Q,\zeta)G(r'',r',Q,\zeta), \tag{6.7}$$

with

$$\begin{aligned}
K(r,r';Q,\zeta) &= \frac{2i}{N}\sum_{q\in BZ}\frac{\cos(qr')}{\zeta - S(q,Q)} \times \left[4iJ_z\cos(q) - 2i\left(V(r) - i\frac{\Gamma(r)}{2}\right)\cos(Qr/2)\right], \\
\Gamma(r,r';Q,\zeta) &= -\frac{2i}{N}\sum_{q\in BZ}\frac{\cos(qr')\cos(qr)}{\zeta - S(q,Q)}.
\end{aligned} \tag{6.8}$$

The momenta $q$ and $Q$ in Eq. (6.7) and Eq. (6.8) are the difference and sum of momenta, defined by $q = (k_1 - k_2)/2$ and $Q = k_1 + k_2$, where $k_1$ and $k_2$ are the momenta of the individual magnons. The momenta $q$ are summed over the Brillouin zone denoted by BZ. The function in the denominator of Eq. (6.8), $S(q,Q)$, is the dispersion of two free magnons, given by

$$\begin{aligned}
S(q,Q) &= E(Q/2+q) + E(Q/2-q) \\
&= -8J_z + 2\Delta - i\Gamma + \sum_{j=1}^{N}(4V_{j0} - 2i\Gamma_{j0})\cos(jQa/2)\cos(jqa),
\end{aligned} \tag{6.9}$$

which determines the poles of $\Gamma(r, r', Q, \zeta)$, whilst the two-magnon bound states are given by solutions to the determinant equation

$$\det\left[\delta_{rr''} + K(r, r'', Q, \zeta)\right] = 0. \tag{6.10}$$

Because of the nearest-neighbour Ising coupling, this determinant equation can be simplified to

$$\begin{aligned}&\left(1 - \frac{1}{N}\sum_{q\in BZ}\frac{8J_z\cos^2(qa)}{\zeta - S(q,Q)}\right)\left(1 + \frac{1}{N}\sum_{q'\in BZ}\frac{S(q',Q)+\chi}{\zeta - S(q',Q)}\right)\\ &+ \frac{8J_z}{N^2}\sum_{q,q'\in BZ}\frac{\cos(qa)\cos(q'a)(S(q',Q)+\chi)}{\left[\zeta - S(q,Q)\right]\left[\zeta - S(q',Q)\right]} = 0,\end{aligned} \tag{6.11}$$

where $\chi = 8J_z - 2\Delta + i\Gamma$. In the limit $N \to \infty$, we can rewrite Eq. (6.11) as

$$(\zeta + \chi)\left[\frac{I_0(\zeta, Q)}{8J_z} - I_0(\zeta, Q)I_2(\zeta, Q) + I_1(\zeta, Q)^2\right] = 0, \tag{6.12}$$

where

$$I_m(\zeta, Q) = \int_{-\pi}^{\pi}\frac{\cos^m(q)}{\zeta - S(q,Q)}\frac{dq}{2\pi}. \tag{6.13}$$

In Section 6.4, we shall find the energies and decay rates of the bound states by solving Eq. (6.12) (or Eq. (6.11) where appropriate) for three specific forms of the XY interaction and nonlocal dissipation: a nearest-neighbour model, next-nearest-neighbour model and a photonic crystal waveguide model. Note that $\zeta = -\chi = -8J_z + 2\Delta - i\Gamma$ is always a solution to Eq. (6.12). However, this solution always lies within the two-magnon energy continuum. In general, we will dismiss any solutions that lie inside the two-magnon energy continuum where the bound state is no longer well defined because it can scatter into the continuum states and become a resonance. While it is possible to have bound states that exist in the scattering continuum [162], these usually occur when the system has certain symmetries that protect the state, which we are not aware of existing in our models.

## 6.3 General Decay Rates of Bound States

We first show that in general, for any model with nonlocal dissipation of the form given in the master equation, Eq. (5.1), the decay rate of the bound state always lies

within the maximal and minimal decay rates of two-free magnons, which we refer to as the two-magnon decay rate continuum. This means the bound state cannot decay more quickly or slowly than its constituent parts. To show this, we consider Eq. (6.1) rewritten in diagonal form

$$\frac{d\hat{\rho}(t)}{dt} = -i\left[\hat{H}, \hat{\rho}(t)\right] + \sum_k \left(2\hat{J}_k^- \hat{\rho}(t)\hat{J}_k^+ - \left\{\hat{J}_k^+ \hat{J}_k^-, \hat{\rho}(t)\right\}\right). \tag{6.14}$$

Here, $\hat{J}_k$ is a decay operator for mode $k$, given by $\hat{J}_k^- = \sqrt{\gamma_k}\sum_i^N c_i^k \hat{\sigma}_i^-$, where $c_i^k$ is the $i^{th}$ component of the $k^{th}$ eigenvector of $\Gamma_{il}/2$ and $\gamma_k$ is the corresponding eigenvalue. For a periodic or large enough system, the eigenvector components are given by $c_i^k = e^{ikr_i}/\sqrt{N}$. To determine the decay rate of the bound state, we focus on the initial dynamics of the $|Q\rangle\langle Q|$ component of the density matrix, by computing the time evolution of $\rho_Q(t) = \langle Q|\hat{\rho}(t)|Q\rangle$, with $\rho_Q(0) = 1$ such that $\hat{\rho}(0) = |Q\rangle\langle Q|$. The wavefunction $|Q\rangle$ is the wavefunction of a bound state with momentum $Q$, given by

$$|Q\rangle = \sum_{ij}^N \alpha_Q f_Q(|r_i - r_j|) e^{iQ(r_i+r_j)/2}\hat{\sigma}_i^+\hat{\sigma}_j^+|0\rangle, \tag{6.15}$$

where $f_Q(r)$ is some localised function that determines the spatial decay of the bound state, with $r = |r_i - r_j|$, and $\alpha_Q$ is a normalisation constant given by $\alpha_Q = 1/\left(2N\sum_{r\neq 0}|f_Q(r)|^2\right)$. Note that we have assumed that the bound state is uniquely determined by its momentum. Indeed in future sections, we only find one bound state solution to Eq. (6.12) (and Eq. (6.11)) for each momentum value $Q$. In general, it is possible for more than one bound state solution to exist for a given $Q$ value, which results in an additional label on $f_Q(r)$ in Eq. (6.15) to distinguish between the different bound states that have the same momentum. However, our results in this section will still hold even if this is the case. The equation of motion for a pure bound state density matrix at short initial times is given by

$$\frac{d\rho_Q(t)}{dt} \approx -\sum_k 8\gamma_k |\alpha_Q F(Q/2-k)|^2 \rho_Q(t), \tag{6.16}$$

where $\rho_Q(t) = \langle Q|\hat{\rho}(t)|Q\rangle$ and

$$F(Q/2-k) = \sum_{r\neq 0} f_Q(r) e^{ir(Q/2-k)}, \tag{6.17}$$

is the Fourier transform of the localised function. At later times, there can be the population of coherences between the bound state and scattering states, which we have neglected. We can see that the bound state density matrix has a decay rate of $4\tilde{\gamma}_Q$, where $\tilde{\gamma}_Q \equiv \sum_k 2\gamma_k |\alpha_Q F(Q/2-k)|^2$, which is the weighted sum of all single magnon decay rates. Note that $\tilde{\gamma}_Q$, is equivalent to the decay rate we will obtain from our Green's function method.

For local dissipation where $\gamma_k = \gamma \equiv \Gamma/2$, the sum over $k$ in $\tilde{\gamma}_Q$ can be completed to give

$$\sum_k 2|\alpha_Q F(Q/2-k)|^2 = 1, \tag{6.18}$$

and so the decay rate of the bound state wavefunction (which is half the decay rate of the pure density matrix) is $2\gamma$ as expected. For nonlocal dissipation, in order to have a bound state decay rate that exists below the two-magnon decay rate continuum, we would need

$$\tilde{\gamma}_Q = \sum_k 2\gamma_k |\alpha_Q F(Q/2-k)|^2 < \gamma_{\min}, \tag{6.19}$$

where $\gamma_{\min}$ is the smallest decay rate for a single magnon. However, using Eq. (6.18), we can rewrite this condition as

$$\sum_k 2(\gamma_k - \gamma_{\min})|\alpha_Q F(Q/2-k)|^2 < 0. \tag{6.20}$$

Both $|\alpha_Q F(Q/2-k)|^2$ and $\gamma_k - \gamma_{\min}$ are always positive, which means this condition can never be fulfilled. The lowest decay rate that could possibly be achieved for the bound state is the lowest decay rate that can be achieved for two free magnons, although this may not always obey the bound state equation. The same argument applies for showing that the bound state cannot have a decay rate above the two-magnon decay rate continuum, such that

$$\sum_k 2(\gamma_k - \gamma_{\max})|\alpha_Q F(Q/2-k)|^2 > 0, \tag{6.21}$$

where $\gamma_{\max}$ is the largest decay rate in the system. Again $|\alpha_Q F(Q/2-k)|^2 > 0$, but $\gamma_k - \gamma_{\max} < 0$, so this condition can not be satisfied and the bound state decay rate must always lie within the two-magnon decay rate continuum.

## 6.4 Results

### 6.4.1 Nearest-Neighbour Model

Having shown in general that the decay rate of the bound state always lies within the two-magnon decay rate continuum, we now look at three specific models for dissipative bound states. The first model we consider is one in which all interactions and the nonlocal dissipation are nearest-neighbour (NN). The energies and decay rates of the one and two free magnon states are given by

$$\begin{aligned}
&\mathrm{Re}[E(k)] = -4J_z + \Delta + 2V_{12}\cos(ka),\\
&|\,\mathrm{Im}[E(k)]| = \frac{\Gamma}{2} + \Gamma_{12}\cos(ka),\\
&\mathrm{Re}[S(q,Q)] = -8J_z + 2\Delta + 4V_{12}\cos(Qa/2)\cos(qa),\\
&|\,\mathrm{Im}[S(q,Q)]| = \Gamma + 2\Gamma_{12}\cos(Qa/2)\cos(qa).
\end{aligned} \tag{6.22}$$

We now solve Eq. (6.12) for the bound state solution. We can evaluate the integrals as defined in Eq. (6.13) using contour integration. Substituting $z = e^{iq}$, the integral transforms into

$$I_m(t,Q) = \frac{-1}{2^m}\oint \frac{(z+z^{-1})^m}{\nu z^2 - (\zeta+\chi)z + \nu}\frac{dz}{2\pi i}, \tag{6.23}$$

where we have defined $\nu = (2V_{12} - i\Gamma_{12})\cos(Qa/2)$. The integral has a pole of order $m$ at $z = 0$ and simple poles at $z_\pm = (\zeta+\chi)/2\nu \pm \sqrt{((\zeta+\chi)/2\nu)^2 - 1}$. The two poles only coincide at $|z| = 1$, so the case of double poles can be ignored for the derivation. Evaluating the integrals gives

$$\begin{aligned}
I_0(t,Q) &= -\frac{\pm 1}{\sqrt{(\zeta+\chi)^2 - 4\nu^2}},\\
I_1(t,Q) &= -\frac{1}{\nu} - \frac{(\zeta+\chi)}{2\nu}\frac{\pm 1}{\sqrt{(\zeta+\chi)^2 - 4\nu^2}},\\
I_2(t,Q) &= -\frac{(\zeta+\chi)}{\nu^2} - \frac{(\zeta+\chi)^2}{4\nu^2}\frac{\pm 1}{\sqrt{(\zeta+\chi)^2 - 4\nu^2}},
\end{aligned} \tag{6.24}$$

where the $\pm 1$ sign depends on whether $z_+$ or $z_-$ lie in the contour. Substituting these solutions into the bound state equation, Eq. (6.12), we obtain the equation

$$\frac{\pm 1}{\sqrt{(\zeta+\chi)^2-\nu^2}}\left(2J_z\frac{(\zeta+\chi)}{\nu^2}-1\right)+\frac{2J_z}{\nu^2}=0, \tag{6.25}$$

which gives the solution $\zeta+\chi=4+\nu^2/(4J_z)$. This gives the following bound state solution

$$\zeta(Q)=-4J_z+2\Delta-i\Gamma+\frac{(2V_{12}-i\Gamma_{12})^2}{4J_z}\cos^2(Qa/2), \tag{6.26}$$

which can be written in terms of the energy and decay rate as

$$\begin{aligned}\mathrm{Re}[\zeta(Q)]&=-4J_z+2\Delta+\frac{4V_{12}^2-\Gamma_{12}^2}{4J_z}\cos^2(Qa/2),\\ |\,\mathrm{Im}[\zeta(Q)]|&=\Gamma+\frac{V_{12}\Gamma_{12}}{J_z}\cos^2(Qa/2).\end{aligned} \tag{6.27}$$

These expressions first appeared in Ref. [163], although we analyse them in more detail here. For the expressions in Eqs. (6.27), there are limits to the parameters we can choose for the solutions to satisfy the bound state equation, Eq. (6.12). However, provided we choose $V_{12}$ and $\Gamma_{12}$ such that the energy term in Eq. (6.27) lies below the two-magnon energy continuum, then we find the bound state equation is always satisfied. We also have to impose $\Gamma/2\geq|\Gamma_{12}|$ in order for the dissipator to always give decay.

Comparing the bound state solution Eq. (6.27) to the free magnon dispersions in Eq. (6.22), we see the energy and decay rate of the bound state depend on a mixture of the interaction and dissipation. The presence of nonlocal dissipation creates a negative shift in energy compared to the XY interaction, which means that the bound state energy is shifted further from the two-magnon energy continuum than in a closed system. This is important as the effects of nonlocal dissipation will not only cause the bound state to decay, but will alter its dynamics travelling through the lattice meaning that even if the bound state has a very small decay rate, it is not sufficient to ignore environmental effects. Furthermore, due to nonlocal dissipation, there is more freedom to engineer the bound state energy and decay than in a closed system. For example, the bound state energy band can be made entirely flat by choosing $V_{12}=\Gamma_{12}/2$. Also, by choosing $V_{12}=0$ such that there is no XY interaction, the bound state experiences

only local dissipation, with a decay rate of $\Gamma$, whereas the one and two free magnons still experience nonlocal dissipation. Finally, looking at Eq. (6.27) in the limit where $V_{12}, \Gamma_{12} \ll J_z$, we can see the effects of the XY interaction and nonlocal dissipation become negligible, with the energy of the bound state tending to $-4J_z$ and the decay rate tending to $\Gamma$ which would be expected for an Ising model with local dissipation.

The relative signs of the XY interaction, nonlocal dissipation and Ising interaction allow the bound state decay rate to be tuned such that it is either entirely subradiant or superradiant, with the most super- or subradiant decay at $Qa = 0$ and a decay rate of $\Gamma$ at the band edge, $Qa = \pm\pi$. To find how subradiant or superradiant it is possible to make the bound state, we extremise the decay rate of the bound state with respect to the parameters $V_{12}$ and $\Gamma_{12}$ for a fixed value of $J_z$, while still obeying the constraint that the bound state energy must lie below the two-magnon energy continuum. We also maintain a fixed decay rate $\Gamma$ (otherwise there is always a trivial minimal decay rate with $\Gamma = \Gamma_{12} = 0$). We find the extremal decay rates occur when $\Gamma_{12} = \pm 2J_z$ and $V_{12} = \pm J_z$ (where the signs can be chosen independently), and so the corresponding energies and decay rates are given by

$$\begin{aligned} &\mathrm{Re}[\zeta(Q)] = -4J_z + 2\Delta, \\ &|\,\mathrm{Im}[\zeta(Q)]| = \Gamma \mp 2J_z \cos^2(Qa/2), \end{aligned} \tag{6.28}$$

where the negative sign gives the maximal (minimal) decay rate and the positive sign gives the minimal (maximal) decay rate for $J_z < 0$ ($J_z > 0$). The largest values for $\Gamma_{12}$ and $V_{12}$ occur when the bound state makes contact with the energy continuum at $Qa = 0$. In Fig. 6.1, we show the minimal decay rate solution for $J_z < 0$ and $\Gamma = 2|\Gamma_{12}|$. The bound state solution is shown by the red band, while the other bands represent the free magnon states, which form a continuum in the thermodynamic limit. We will therefore refer to the energy curves of the free-magnon states as the two-magnon energy continuum and the corresponding decay rate curves as the two-magnon decay rate continuum. Note that the shading used on the free magnon bands gives a correspondence between the energy of the band and its associated decay rate i.e. the light bands at low energy in the top plot of Fig. 6.1 have a decay rate given by the light bands in the lower plot of Fig. 6.1. This convention will be used throughout the chapter. The bound state decay rate lies in the two-magnon decay rate continuum as expected and is smaller than half the free magnon decay rates at $Qa = \pi$ and 2/3 of the continuum at $Qa = 0$, with the lowest energy bands of the two-magnon continuum

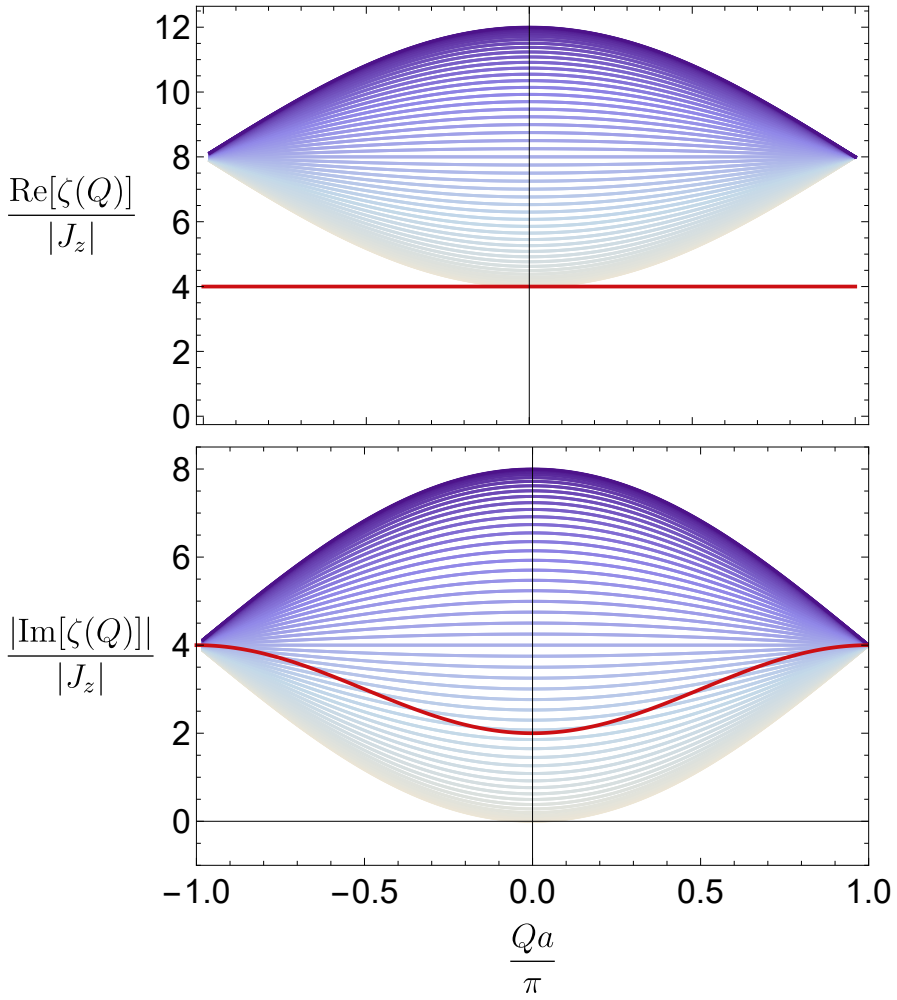


**Figure 6.1** Energy (top) and decay rate (bottom) of the bound state for a NN system for $J_z < 0$ and $\Gamma = 2|\Gamma_{12}|$. The bound state solution is shown in red whilst the shaded region represents the two-magnon continuum. The parameters used are $\Gamma_{12}/|J_z| = -2$ and $V_{12}/|J_z| = -1$ which give the smallest possible decay rate for the bound state while keeping the energy separate from the continuum.

having the smallest decay rates. For the maximal decay rate solution, the results are similar to Fig. 6.1, but the decay rates reverse, with the lowest energy bands having the highest decay rates and the bound state solution having a larger decay rate than most of the two-magnon decay rate continuum.

### 6.4.2 Next-Nearest-Neighbour Model

The NN model studied in the previous section demonstrated many features of dissipative bound states, but also missed some qualitative features of bound states with longer range hopping. We therefore consider a model where the XY interaction and nonlocal dissipation are both next-nearest-neighbour (NNN), finding that the inclusion of additional site interactions produces important differences in the properties of the bound state compared to a NN model. The one and two free magnon energies and decay rates are given by

$$\begin{aligned}
\mathrm{Re}[E(k)] =& -4J_z + \Delta + 2V_{12}\cos(ka) + 2V_{13}\cos(2ka),\\
|\,\mathrm{Im}[E(k)]| =& \frac{\Gamma}{2} + \Gamma_{12}\cos(ka) + \Gamma_{13}\cos(2ka),\\
\mathrm{Re}[S(q,Q)] =& -8J_z + 2\Delta + 4V_{12}\cos(Qa/2)\cos(qa) + 4V_{13}\cos(Qa)\cos(2qa),\\
|\,\mathrm{Im}[S(q,Q)]| =& \Gamma + 2\Gamma_{12}\cos(Qa/2)\cos(qa) + 2\Gamma_{13}\cos(Qa)\cos(2qa).
\end{aligned} \tag{6.29}$$

To derive the analytic expression for the next-nearest-neighbour bound state solution, we use the substitution $z = e^{iq}$ to transform the integral in Eq. (6.13) into the following contour integral

$$I_m(t,Q) = \frac{-1}{2^m}\oint \frac{z(z+z^{-1})^m}{\xi z^4 + \nu z^3 - (\zeta+\chi)z^2 + \nu z + \xi}\frac{dz}{2\pi i}, \tag{6.30}$$

where $\xi = (2V_{13} - i\Gamma_{13})\cos(Qa)$ and $\nu = (2V_{12} - i\Gamma_{12})\cos(Qa/2)$. The quartic in the denominator is palindromic, which means the solutions obey a quadratic in $(z + 1/z)$. Therefore, if $z$ is a solution to the quartic, then so too is $1/z$, and this immediately indicates that only two of the four roots can exist inside the contour. We also find that the residue of the roots $1/z$ and $z$ only differ by a sign. The integrals in Eq. (6.30)

can therefore be evaluated to give

$$\begin{aligned} I_0(t,Q) &= \frac{-1}{\xi}(F_1+F_2), \\ I_1(t,Q) &= \frac{-1}{2\xi}(\beta_1 F_1+\beta_2 F_2), \\ I_2(t,Q) &= \frac{-1}{4\xi}(1+\beta_1^2 F_1+\beta_2^2 F_2), \end{aligned} \tag{6.31}$$

where

$$\begin{aligned} F_{1/2} &= \pm\frac{1}{\sqrt{\beta_{1/2}^2-4}(\beta_{1/2}-\beta_{2/1})}, \\ \beta_{1/2} &= -\frac{\nu}{2\xi}\mp\sqrt{\left(\frac{\nu}{2\xi}\right)^2+\frac{(\zeta+\chi)}{\xi}+2}. \end{aligned} \tag{6.32}$$

The sign of $F_{1/2}$ depends on whether the root $z_{1/2}$ or its inverse lies inside the contour. Substituting the integral solutions into the bound state equation, Eq. (6.12), gives

$$\frac{1}{F_1}+\frac{1}{F_2}+\frac{2J_z(\beta_1-\beta_2)^2}{\xi+2J_z}=0. \tag{6.33}$$

We can now solve Eq. (6.33) to obtain the bound state solution. Before doing so, we note that there is also the possibility of a double root in Eq. (6.30) when $\zeta+\chi=2\xi+\nu^2/(4\xi)$. In this case, the denominator of the integrals in Eq. (6.13) can be simplified to $(4\xi\cos(q)-\nu)^2/(4\xi)$. We can then evaluate the NNN integrals without using contour integration, but find these solutions do not obey the bound state solution.

The bound state solution that obeys Eq. (6.33) is given by

$$\begin{aligned} \zeta(Q) = -8J_z+2\Delta-i\Gamma+4J_{13}\cos(Qa)+\frac{J_{12}^2\cos^2(Qa/2)}{J_z} \\ +\frac{J_{12}^2\cos^2(Qa/2)J_{13}\cos(Qa)}{2J_z^2}+\frac{8J_z^2}{2J_z+J_{13}\cos(Qa)}, \end{aligned} \tag{6.34}$$

where $J_{12} = V_{12} - i\Gamma_{12}/2$ and $J_{13} = V_{13} - i\Gamma_{13}/2$. Writing in terms of the energy and decay rate gives

$$\begin{aligned}
&\mathrm{Re}[\zeta(Q)] = -8J_z + 2\Delta + \frac{4V_{12}^2 - \Gamma_{12}^2}{4J_z}\cos^2(Qa/2) \\
&+ \frac{V_{13}(4V_{12}^2 - \Gamma_{12}^2) - 2\Gamma_{13}\Gamma_{12}V_{12}}{8J_z^2}\cos(Qa)\cos^2(Qa/2) \\
&+ 4V_{13}\cos(Qa) + \frac{16J_z^2(4J_z + 2V_{13}\cos(Qa))}{(4J_z + 2V_{13}\cos(Qa))^2 + (\Gamma_{13}\cos(Qa))^2}, \\
&|\,\mathrm{Im}[\zeta(Q)]| = \Gamma + \frac{V_{12}\Gamma_{12}}{J_z}\cos^2(Qa/2) + 2\Gamma_{13}\cos(Qa) \\
&+ \frac{\Gamma_{13}(4V_{12}^2 - \Gamma_{12}^2) + 8V_{13}\Gamma_{12}V_{12}}{16J_z^2}\cos(Qa)\cos^2(Qa/2) \\
&- \frac{16J_z^2\Gamma_{13}\cos(Qa)}{(4J_z + 2V_{13}\cos(Qa))^2 + (\Gamma_{13}\cos(Qa))^2}.
\end{aligned} \tag{6.35}$$

As for the NN model, there is a constraint on the values of the dissipative couplings to ensure the magnons always decay, which is $\Gamma/2 \geq |\Gamma_{12} + \Gamma_{13}|$. Likewise, we have to choose parameters that satisfy the bound state condition Eq. (6.12), finding again that provided the energy of the bound state lies below the continuum, then Eq. (6.12) is satisfied. Our NNN bound state solution is the same as that found in Ref. [151] but with a complex XY interaction. This is also true of our NN result in Eq. (6.27), which can be obtained by taking the bound state result in Ref. [144] with a complex XY interaction.

The inclusion of an additional site in the XY interaction and nonlocal dissipation results in a more complex bound state solution than in the NN model. Looking at the terms in Eq. (6.35) in more detail, we see that the NN solution in Eq. (6.27) can be recovered by letting $V_{13}, \Gamma_{13} = 0$, and that now we have additional terms due to two-site hopping processes and a term that mixes the NN and NNN parameters. Because of the new magnon hopping terms, the decay rate of the bound state is no longer fixed to be $\Gamma$ at $Qa = \pm\pi$ as was the case for NN interactions, and the smallest and largest decay rates do not have to occur at $Qa = 0$ anymore. Therefore the inclusion of NNN interactions allows more freedom in choosing at what momenta $Q$ the bound state can have its highest or smallest decay rate. However, we can now no longer engineer an entirely flat energy band due to the presence of both $\cos(Qa/2)$ and $\cos(Qa)$ terms (unless trivially the NNN couplings are set to zero). Looking at the

limit of $V_{13}, \Gamma_{13}, V_{12}, \Gamma_{12} \ll J_z$, we find Eq. (6.35) simplifies to

$$\begin{aligned} \mathrm{Re}[\zeta(Q)] &\approx -4J_z + 2\Delta + 2V_{13}\cos(Qa), \\ |\,\mathrm{Im}[\zeta(Q)]| &\approx \Gamma + \Gamma_{13}\cos(Qa). \end{aligned} \tag{6.36}$$

We find that there is now always a contribution to the decay rate from the NNN interactions, that means even tightly confined bound states still experience the effects of nonlocal dissipation, which was not the case for the NN model. We can also see that the smallest decay rate will occur at $Qa = 0$ ($Qa = \pm\pi$) and largest decay rate at $Qa = \pm\pi$ ($Qa = 0$) for $\Gamma_{13} < 0$ ($\Gamma_{13} > 0$).

We now extremise the NNN bound state decay rate for a fixed $\Gamma$ with respect to the parameters $V_{12}$, $V_{13}$, $\Gamma_{12}$ and $\Gamma_{13}$ to find the smallest and largest decay rates the bound state can have while its energy remains separate from the two-magnon energy continuum. Due to the complexity of Eqs. (6.35), we solve this numerically, finding that the solution with minimal (maximal) decay rate occurs when $V_{12} = \pm 1.135 J_z$, $V_{13} = -0.293 J_z$, $\Gamma_{12} = \pm 1.926 J_z$ and $\Gamma_{13} = 0.578 J_z$, and the maximal (minimal) solution occurs when $V_{12} = \mp 1.135 J_z$, $V_{13} = -0.293 J_z$, $\Gamma_{12} = \pm 1.926 J_z$ and $\Gamma_{13} = -0.578 J_z$ for $J_z < 0$ ($J_z > 0$), where in both cases, we are free to choose the positive or negative sign. The largest values of all parameters occur when the bound state energy makes contact with the two-magnon energy continuum at $Qa = 0$, as was the case for the NN interactions. In Fig. 6.2, we show the minimal solution with $J_z < 0$ and $\Gamma = 2|(\Gamma_{12} + \Gamma_{13})|$. Again, we find the decay rate of the bound state lies within the two-magnon decay rate continuum, with the bound state having a smaller decay rate than 30% of the continuum at $Qa = \pi$ and up to 70% of the continuum at $Qa = 0$. We should note there is a second minimal (maximal) decay rate solution with parameters $V_{12} = \Gamma_{12} = 0$, $\Gamma_{13} = +0.402 J_z$ and $V_{13} = -0.827 J_z$ and maximal (minimal) solution for $V_{12} = \Gamma_{12} = 0$, $\Gamma_{13} = -0.402 J_z$ and $V_{13} = -0.827 J_z$ for $J_z < 0$ ($J_z > 0$). However, we have not shown this solution as it is more unphysical due to the absence of the NN terms.

### 6.4.3 Photonic Crystal Waveguide Model

We now study one final model, which should be an experimentally realisable set-up to study dissipative bound states. We consider Rydberg dressed two-level atoms that are coupled to a photonic crystal waveguide (PCW). Systems of two-level atoms where one state is a Rydberg state or Rydberg dressed are already well studied as realisable quantum simulators [26–30]. Likewise, PCWs are also gaining attention as a method

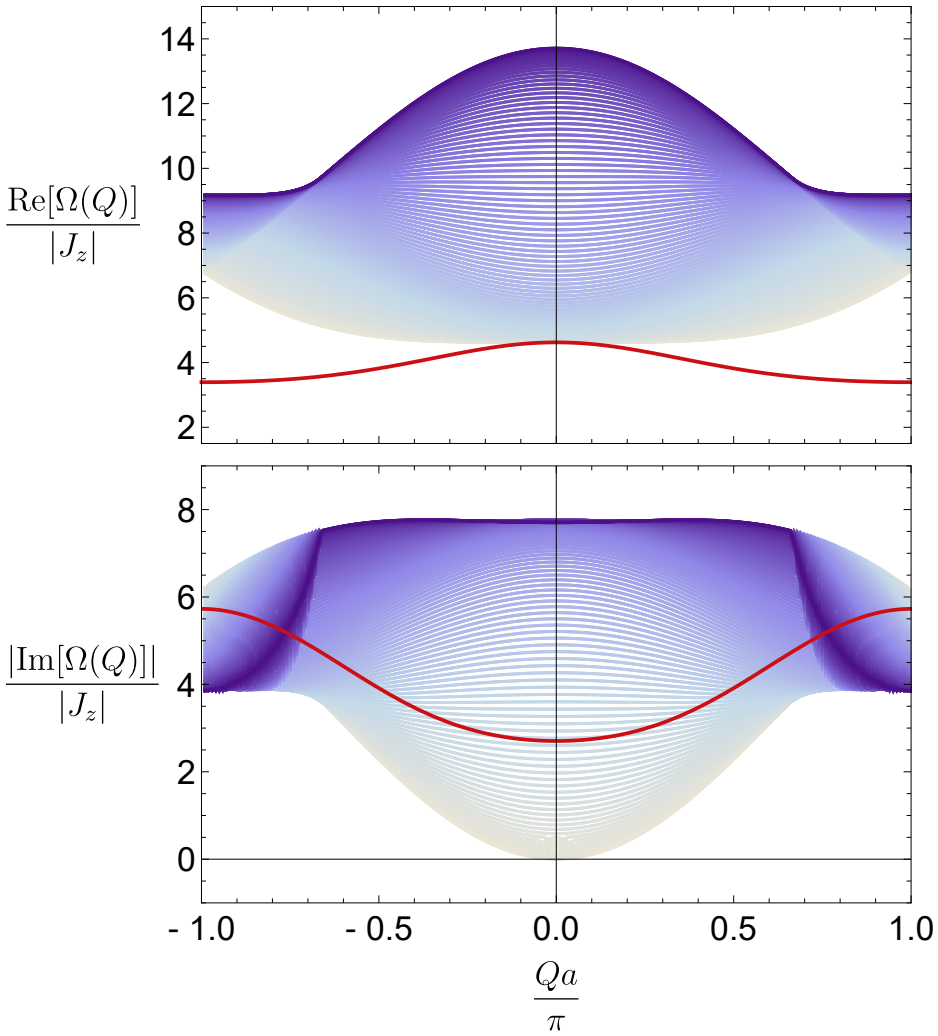


**Figure 6.2** Energy (top) and decay rate (bottom) of the bound state for a NNN system with $\Gamma = 2|(\Gamma_{12} + \Gamma_{13})|$ and $J_z < 0$.The bound state solution is shown by the red curve whilst the shaded curves represent the two free magnon solutions. The parameters used are $V_{12}/|J_z| = 1.135$, $V_{13}/|J_z| = 0.293$, $\Gamma_{12}/|J_z| = 1.926$ and $\Gamma_{13}/|J_z| = -0.578$, which give the smallest possible decay rate for the bound state while keeping the energy separate from the continuum.

for quantum simulation and quantum information processing due to the high tunability of the interactions between coupled quantum emitters [164–168]. For atoms coupled to a PCW, photons emitted from the atoms can propagate to other atoms along the chain, which mediates an effective XY interaction and nonlocal dissipation. With a system Hamiltonian, $\hat{H}_{sys} = \sum_k \left(\omega_{wg} - i\frac{\gamma_c}{2} - 2J\cos k\right)\hat{a}_k^\dagger \hat{a}_k + \sum_i \omega_{eg}\hat{\sigma}_i^z$, the interaction between the atoms and the PCW in the interaction picture is given by [169]

$$\hat{H}(t) = g\sum_i (\hat{\sigma}_i^+ e^{-i\omega_{eg}t}\hat{E}(x_i,t) + \hat{\sigma}_i^- e^{-i\omega_{eg}t}\hat{E}^\dagger(x_i,t)), \tag{6.37}$$

where $\hat{E}(x,t) = \sum_k e^{ikx}e^{i\omega_{wg}t}\hat{a}_k/\sqrt{N}$ is the electric field operator, $g$ is the coupling of the atoms to the PCW, $\omega_{eg}$ is the transition energy of the two-level system, and $\omega_{wg}$ the photon mode frequency, with a loss rate $\gamma_c$. By tracing out the photonic modes, $\hat{a}_k$, and assuming the Born and Markov approximations as outlined in Chapter 2, we can obtain a master equation of the form in Eq. (6.1). The dissipation couplings are given by $\Gamma_{il} = 2\mathrm{Re}[A_{ij}]$ and the XY interaction given by $V_{il} = \mathrm{Im}[A_{ij}]$, where $A_{ij}$ is of the form

$$\begin{aligned} A_{ij} &= g^2\int_0^\infty \langle \hat{E}(x_i,t)\hat{E}^\dagger(x_j,t-\tau)\rangle e^{i\omega_{eg}\tau}d\tau \\ &= \frac{J_{xy}e^{iK|r_{ij}|}}{2\sqrt{1-(\delta/(2J)+i\gamma_c/(4J))^2}}. \end{aligned} \tag{6.38}$$

The parameter $J_{xy} = g^2/J$ is the coupling of the atoms to the PCW, $J$ is an energy scale determining the PCW bandwidth, and $K_{wg}a = \pi - \arccos(\delta/(2J) + i\gamma_c/(4J)) = k_{wg}a + i\kappa_{wg}a$ is the PCW wavevector. The PCW wavevector depends on the detuning, $\delta = (\omega_{eg} - \omega_{wg})$, of the atomic transition frequency, $\omega_{eg}$, from the photon mode frequency, $\omega_{wg}$, and also the loss rate of photons from the PCW, $\gamma_c$. If $|\delta/J| < 2$, then the photon lies within the bandwidth and can propagate along the PCW with a group velocity given by $v = |\sqrt{4J^2 - (\delta + i\gamma_c/2)^2}|$. However, if $|\delta/J| > 2$, then the photon cannot propagate and instead exponentially decays along the PCW.

In order for bound states to form, we also need an Ising interaction. This can be engineered by dressing [26] either the excited state, $|e\rangle$ or ground state, $|g\rangle$, of an atom with a Rydberg state $|r\rangle$, giving a new state $|\tilde{e}\rangle = |e\rangle + \beta|r\rangle$ where $\beta = \zeta_d/2\Delta_d$, set by the drive $\zeta_d$ and detuning $\Delta_d$ that couple $|e\rangle$ to $|r\rangle$. The atoms then interact with an

Ising interaction of the form

$$U_{il} = \frac{U_0}{1 + (|r_i - r_l|/R_c)^6}, \tag{6.39}$$

where $U_0 = \hbar\zeta_d^4/8\Delta_d^3$ and $R_c$ is some cut off length to the interaction. For small $R_c$, this is a good approximation to a NN Ising interaction. The sign and magnitude of $U_0$ can be fixed by the laser detuning and it is also possible to add additional XY interactions between the atoms which gives more freedom in tuning $V_{ij}$ separately from $\Gamma_{ij}$.

For the PCW system, the one and two free magnon energies and decay rates are given by

$$\begin{aligned}
\mathrm{Re}[E(k)] &= -4J_z + \Delta + f(k) + f(-k), \\
|\,\mathrm{Im}[E(k)]| &= \frac{\Gamma}{2} + g(k) + g(-k), \\
\mathrm{Re}[S(q,Q)] &= -8J_z + 2\Delta + f(Q/2+q) + f(Q/2-q) + f(-Q/2+q) + f(-Q/2-q), \\
|\,\mathrm{Im}[S(q,Q)]| &= \Gamma + g(Q/2+q) + g(Q/2-q) + g(-Q/2+q) + g(-Q/2-q),
\end{aligned} \tag{6.40}$$

where $\Delta = V_{11}/2 + \delta/2 + \delta_{\mathrm{add}}$, with $\delta_{\mathrm{add}}$ being an additional detuning to those from the waveguide, and

$$\begin{aligned}
f(k) &= \left( \frac{\Gamma \sin((k_{wg}+k)a) + V_{11}[\cos((k_{wg}+k)a) - e^{-\kappa_{wg}a}]}{e^{\kappa_{wg}a} + e^{-\kappa_{wg}a} - 2\cos((k_{wg}+k)a)} \right), \\
g(k) &= \left( \frac{\Gamma[\cos((k_{wg}+k)a) - e^{-\kappa_{wg}a}] - V_{11}\sin((k_{wg}+k)a)}{e^{\kappa_{wg}a} + e^{-\kappa_{wq}a} - 2\cos((k_{wg}+k)a)} \right).
\end{aligned} \tag{6.41}$$

For the rest of this section, we will choose the additional detuning, $\delta_{\mathrm{add}}$ such that $\Delta = 0$ and so we can ignore the contributions to energy from the onsite term, $V_{11}$ and detuning from the waveguide mode $\delta$. We will also work with $J_z < 0$.

In Fig. 6.3, we plot the energy and decay rate of the single magnon dispersion for $\gamma_c/J = 2$, $\delta/J = 0$ and $J_{xy}/|J_z| = 3$. If $|\delta/J| < 2$ and $\gamma_c/J$ is small, then about the points $k = \pm k_{wg}$, the decay rate is well modelled by two Lorentzians with a width of $4\sinh(\kappa_{wg}a/2)$ and maximum value of $\Gamma/[4\tanh(\kappa_{wg}a/2)]$. Similarly, the energy of the magnon is well described by the derivative of a Lorentzian with width $4\sinh(\kappa_{wg}a/2)$ and maximal (minimal) values given by $\pm\Gamma/[8\sinh(\kappa_{wg}a/2)]$. As $\gamma_c/J$ decreases (and so $\kappa_{wg} \to 0$), the energies of the magnons and decay rates about $k = \pm k_{wg}$ diverge within

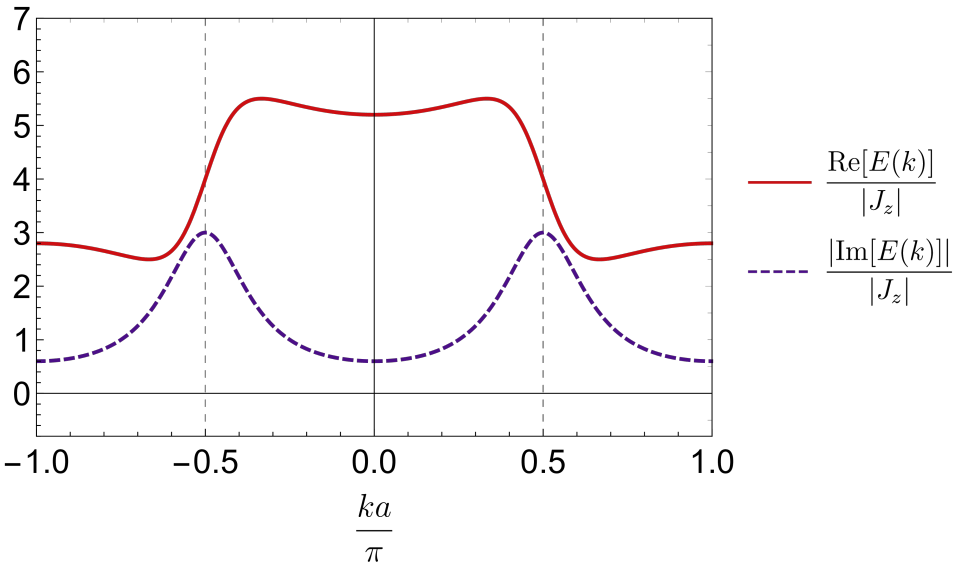


**Figure 6.3** Energy and decay rate of a single magnon for the PCW system with $\gamma_c/J = 2$, $\delta/J = 0$ and $J_{xy}/|J_z| = 3$. The energy is shown by the red (solid) line and the decay rate by the purple (dashed) line. The largest decay rates occur when $k = \pm k_{wg}$, shown by the grey lines.

the photonic bandwidth ($|\delta/J| < 2$). However, outside the bandwidth ($|\delta/J| > 2$), the energy of the magnon is bounded and its decay rate drops to zero as $\gamma_c \to 0$, leaving the system effectively closed. The single magnon dispersions can be thought of as the hybridisation of a photon propagating through the waveguide with a dispersion $\omega_k = \omega_{wg} - 2J\cos(k)$ and momentum $k$, and a single atom with energy $\omega_{eg}$.

We now look at the bound state solutions in the PCW and discuss their properties. The bound state condition, Eq. (6.12), is too complex to be solved analytically, so we instead tackle the problem numerically for finite sized systems by solving Eq. (6.11). In Fig. 6.4, we plot some typical solutions of Eq. (6.11) for a system size of $N = 99$, with $\gamma_c/J = 2$, $J_{xy}/|J_z| = 3$ and for $\delta/J = (-3, -1.5, 0, 1.5, 3)$. We see that bound state decay rate lies within the two-magnon decay rate continuum as expected, and is smaller than the decay rate of the lowest energy bands of the continuum for $\delta/J < -2$, but larger than the decay rate of the lowest energy bands of the continuum for $\delta/J > 2$. For intermediate detunings, whether the bound state decay rate is smaller or larger than the decay rate of the lowest energy bands depends on the momentum of the bound state. As for the NNN model, we find the minimal and maximal decay rate of the bound state is no longer constrained to occur at $Qa = 0$ and that the decay rate at $Qa = \pi$ is not given by $\Gamma$ as a consequence of the long-range interactions. If $\kappa_{wg}$ is large enough, then the bound state solutions are well modelled by the NNN analytics

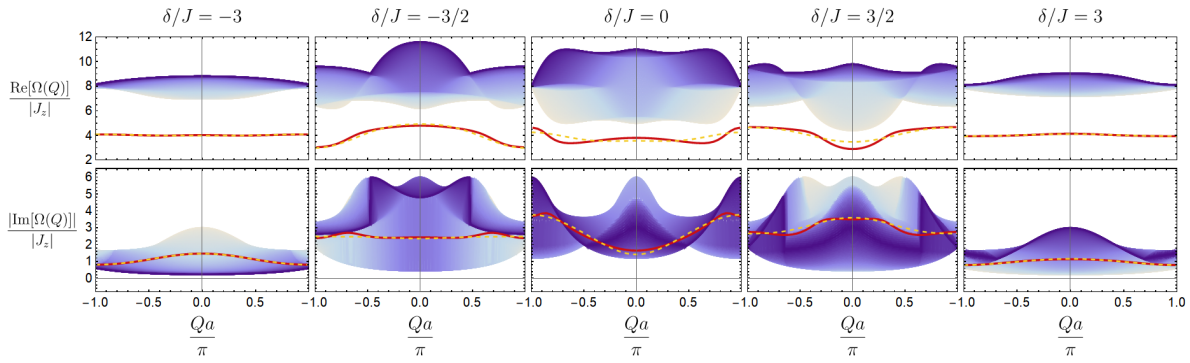


**Figure 6.4** Examples of the two-magnon bound states that can form in the PCW model for a system size of $N = 99$ with parameters $\gamma_c/J = 2$, $J_{xy}/|J_z| = 3$ and $\delta/J = (-3, -1.5, 0, 1.5, 3)$. The top panels show the energy of the bound state and the lower panels show the decay rate. The red line represents the bound state solution and the shaded region represents the continuum of two-magnon states. We find that the bound state energy lies below the two-magnon energy continuum and the decay rate of the bound state always lies within the two-magnon decay rate continuum. When $\delta/J < -2$, the bound state decay rate is always lower than that of the lowest energy bands whilst if $\delta/J > 2$, then the decay rate of the bound state is larger than the lowest energy bands. Note that for $\delta/J = 0$, the decay rates of the lowest energy bands are obscured by the highest energy bands as they share the same decay rate. We also show the NNN bound state result from Eq. (6.35) with the dashed orange line. We see the NNN result agrees well with the waveguide results when $\kappa_{wg}a$ is large.

due to the exponential decay of the PCW interaction. This can be seen by the close agreement between the NNN and PCW bound state solutions when $\delta/J = \pm 3$, which gives the largest $\kappa_{wg}$. For intermediate detunings, the agreement is not as good, but can be made increasingly better for larger $\gamma_c/J$.

In Fig. 6.5, we plot the momentum for which the bound state has the smallest decay rate as a function of $\delta/J$ and $\gamma_c/J$. We find that there is a transition between the bound state having the smallest decay rate at $Qa = 0$ when $|\delta/J| < 1.4$ to $Qa = \pi$ when $|\delta/J| > 1.4$. This transition can be explained by looking at the weak XY limit of the NNN bound state solutions given by Eq. (6.36). In the weak limit, we find that the momentum where the decay rate of the bound state is smallest transitions from $Qa = 0$ to $Qa = \pi$ when $\Gamma_{13}$ changes sign. We show when $\Gamma_{13} = 0$ in Fig. 6.5 by the red dashed lines, and find it agrees well with the transition in the PCW, with $\Gamma_{13} < 0$ when $|\delta/J| > 1.4$. The transition moves to larger values of $|\delta/J|$ as $\gamma_c/J$ increases, and also becomes sharper as the NNN solution becomes a better approximation to the PCW results.

Finally, we discuss how the bound state formation depends on $\delta/J$ and $\gamma_c/J$. Fig. 6.6 shows where the bound state rejoins the two-magnon energy continuum as a

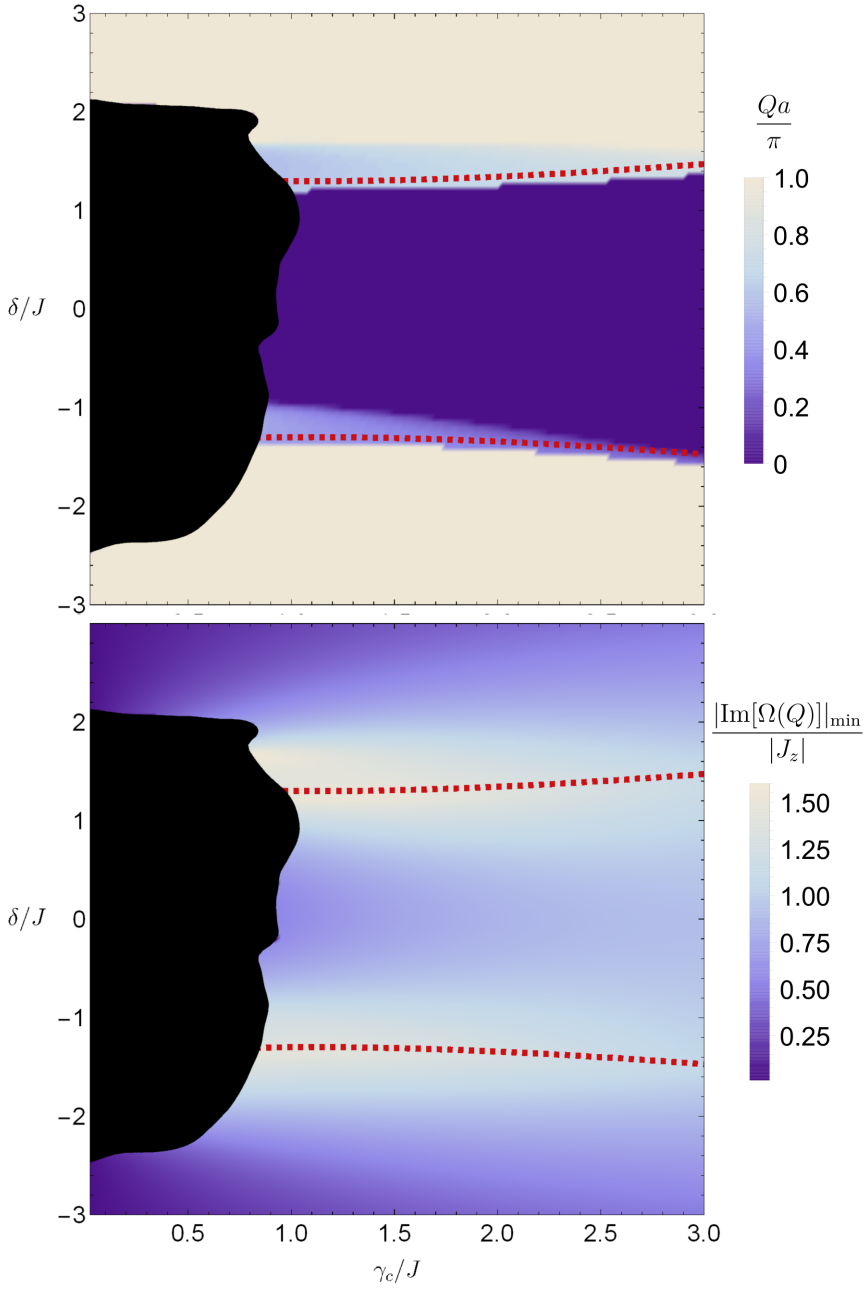


**Figure 6.5** (a) Momentum at which the smallest decay rate of the bound state occurs for a system size of $N = 99$ with $J_{xy}/|J_z| = 1.5$. We see there is a clear transition between the smallest decay rate occurring at $Qa = \pi$ when $|\delta/J| \gtrsim 1.4$, and $Qa = 0$ for $|\delta/J| \lesssim 1.4$. The red dashed lines show when $\Gamma_{13}$ changes sign which explains the transition as described in the main text. The black region shows where the bound state solution starts to merge with the two-magnon continuum. (b) Magnitude of the smallest decay rate. We see that when the crossover in momentum occurs when $\Gamma_{13} = 0$, the decay rate increases, but decreases again as $\Gamma_{13}$ becomes larger.

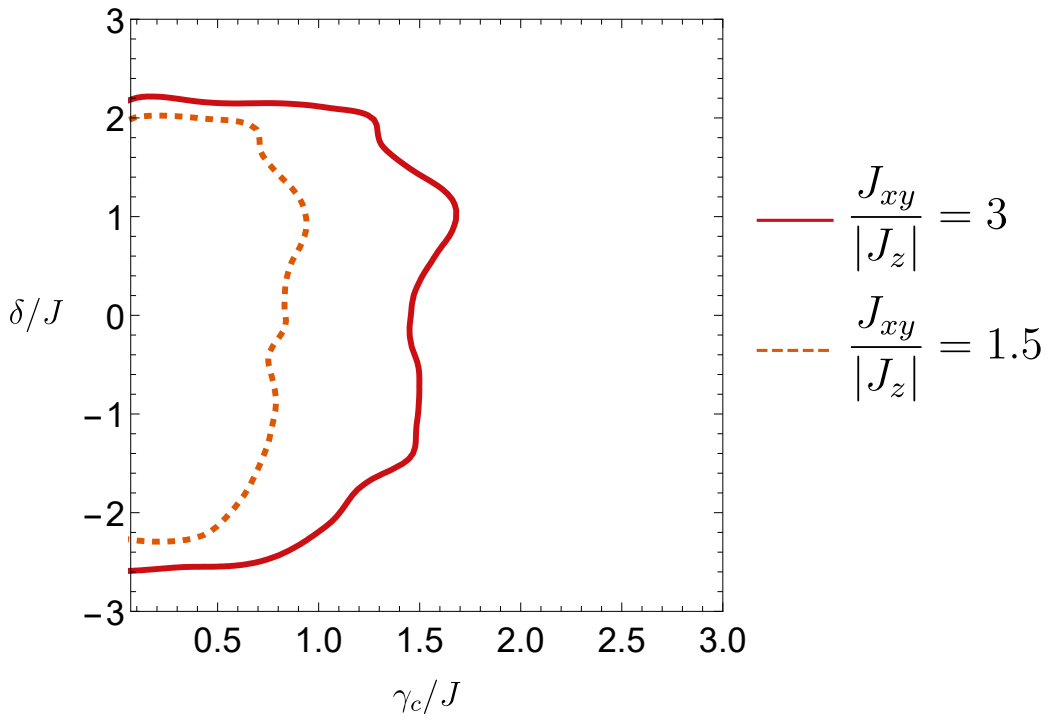


**Figure 6.6** Diagram of when the bound state can form for the PCW model for a system size of $N = 99$ with $J_{xy}/|J_z| = 1.5$ (dashed line) and $J_{xy}/|J_z| = 3$ (solid line). Between the $\delta$ axis and the bound state line, the bound state energy starts to join the two-magnon energy continuum for some or all momenta, $Q$. Outside this region, the bound state energy lies separate from the two-magnon energy continuum for all momenta $Q$. We see that the bound state can not remain separate from the two-magnon energy continuum at low $\gamma_c/J$ near the band edge or inside the bandwidth, but can remain separate from the two-magnon energy continuum everywhere else.

function of $\delta/J$ and $\gamma_c/J$. We find there is a region inside the bandwidth that extends along the $\gamma_c/J$ axis where the bound state joins the continuum and that, as $J_{xy}/|J_z|$ increases, this region also increases in size. The reason the bound state starts to rejoin the continuum for small $\gamma_c/J$ inside the bandwith is due to the diverging strength of the single magnon energy around $k = \pm k_{wg}$. For increasingly large systems, more momentum modes around these points are allowed and so the energy range of the two-magnon continuum grows until the bound state is absorbed. However, outside the bandwidth and in the small $\gamma_c/J$ limit, the bound state energy can remain separate from the two-magnon energy continuum for any value of $J_{xy}/|J_z|$, provided $\delta/J$ is large enough. This is because the two-magnon energy continuum is now bounded as $\gamma_c/J \to 0$ and so bound states can remain separate from the continuum. As mentioned in our discussion of the single magnon dispersion, the imaginary part of the PCW

interaction, Eq. (6.38), becomes negligible in this limit, and so the system becomes closed, with the decay rate of the bound state dropping to zero. When $\gamma_c/J$ becomes large, or when $|\delta/J| \gg 2$, the XY interaction becomes increasingly shorter ranged due to the exponential decay, until eventually it is negligible compared to the Ising interaction. In this limit, the bound state is well separated from the two-magnon energy continuum with the bound state energy tending to $-4J_z$ and the decay rate tending to $\Gamma$.

Our analysis of a PCW has shown how many features of dissipative bound states can be obtained for a single photonic mode and how, for large $\kappa_{wg}a$, the PCW is well described by the NNN analytics. For a single mode, it is not possible to obtain the NN results, no matter how large $\kappa_{wg}a$ is. To see why this is the case, we look at the NNN bound state solution in Eq. (6.34). We can see that for an exponentially decaying function, $J_{13} \sim J_{12}^2/J_z$, which means that there is always a NNN contribution to the bound state solution that is of the order of the NN parts, so the NNN contribution cannot be ignored. However, it could be possible to engineer more exotic XY interactions by combining many modes or coupling to more than one waveguide. This could also be done in parallel with different Rydberg dressing schemes or allowing other interactions, such as dipole interactions, to occur between atoms.

## 6.5 Discussion

We have shown that two-magnon bound states can generally form in dissipative spin chains with XY and Ising interactions. We find the inclusion of nonlocal dissipation not only gives the bound state a momentum dependent decay rate, but also alters the bound state energy compared to a closed system or system with local dissipation. Nonlocal dissipation also allows for a greater degree of freedom in engineering the energy and decay rate of the bound state. We have shown that the decay rate of the bound state cannot be smaller or larger than its constituent free magnons. Nevertheless, it is still possible to achieve bound states that have a decay rate much lower than a large proportion of the two-magnon decay rate continuum.

We now discuss the experimental set-up of the PCW model in more detail. The PCW can be realised with an alligator waveguide [166, 167], with high tunability over the allowed modes and loss processes. By choosing an appropriate Rydberg dressing scheme for either the ground or excited state of the two-level transition coupled to the PCW, it should be possible to engineer suitable Ising-like interactions with NN or even

beyond NN range. We note that the waveguide can modify the interaction between the Rydberg atoms [170]. Typically, the effect of the waveguide will make the Rydberg interactions shorter ranged than in free space which means the nearest-neighbour Ising interaction will still hold. However, even if the Ising interaction has a spatial extent beyond NN, we expect many of our results will be qualitatively the same.

When studying the bound states, one has to be careful not to violate the Markovian approximation. For the Markovian approximation to be valid, it is required that the time for a photon to travel down a PCW, $(N-1)a/v$, where $v = |\sqrt{4J^2 - (\delta + i\gamma_c/2)^2}|$ is the PCW group velocity, is much smaller than the time for the atoms to decay, $1/\Gamma = 1/(2\mathrm{Re}[A_{ii}])$ [169]. Substituting in $A_{ii}$ from Eq. (6.38) gives the condition

$$\frac{\mathrm{Re}\left[\sqrt{1-(\delta/(2J)+i\gamma_c/(4J))^2}\right]}{J_{xy}} \gg \frac{(N-1)a}{|\sqrt{4J^2-(\delta+i\gamma_c/2)^2}|}, \tag{6.42}$$

which is satisfied provided the coupling of the atoms to the waveguide is weak and also that the detuning is away from the band edge at $\delta = \pm 2J$ when $\gamma_c/J$ is small. The expression Eq. (6.42) also shows that the system needs to be finite to not violate the Markovian approximation. However, we have checked and found that there are bound state solutions with similar properties to those in the main text for finite size systems with open boundary conditions. Therefore, it should be possible to observe many of our bound states results for large enough finite sized systems with open boundary conditions or periodic boundary conditions.

Finally, measurement of the bound state decay rate and energy should be possible by observing the emission when the bound state decays. Following the steps outlined in Ref. [163], the emission properties of the bound state are given by the correlator $g(t,\boldsymbol{r}) = \langle \hat{\boldsymbol{E}}^{(-)}(t,\boldsymbol{r})\hat{\boldsymbol{E}}^{(+)}(t,\boldsymbol{r})\rangle$ which can be calculated from the electric field, $\hat{\boldsymbol{E}}^{(-)}(t,\boldsymbol{r})$. For decay of a pure bound state, $\hat{\rho}(0) = |Q\rangle\langle Q|$, the correlator $g(t,\boldsymbol{r})$ is given by

$$\begin{aligned}\frac{g(t,\boldsymbol{r})}{|\eta W(\boldsymbol{r})|^2} = \sum_k 4|\alpha_Q F(Q/2-k)|^2 \Bigg[ & \delta_{Q-k,\Delta_k^Q \sin(\beta)/c} e^{-4\tilde{\gamma}_Q t_r} \\ & + \frac{\gamma_{k+Q}}{\tilde{\gamma}_Q - \gamma_k}\delta_{k,\Delta_0^k \sin(\beta)/c}\left(e^{-2\gamma_k t_r} - e^{-4\tilde{\gamma}_Q t_r}\right)\Bigg],\end{aligned} \tag{6.43}$$

where $t_r \equiv t - r/c$, $\Delta_0^k = \mathrm{Re}[E(k)]$, $\Delta_k^Q = \mathrm{Re}[\zeta(Q)] - \mathrm{Re}[E(k)]$, $\eta = \omega_{eg}^2/(4\pi\epsilon_0 c)$ and $W(\boldsymbol{r}) = \boldsymbol{d}/r - \boldsymbol{r}(\boldsymbol{d}.\boldsymbol{r})/r^3$ is the far-field dipole emission profile. Note we have neglected any coherences between the bound state and scattering states which may occur at later

times. There are two contributions to the emission of the bound state; one from the decay of the bound state to a single magnon with momentum $k$, and one from the decay of a single magnon to the ground state. The delta functions determine the emission angle $\beta$ for each of these decay processes in terms of the momentum and energy of the bound state and single magnons, where $\beta$ is defined from the perpendicular axis from the spin chain. The total emission is then a sum over all these processes. The quantity $|\alpha_Q F(Q/2-k)|^2$ that determined the decay rate of the bound state also plays a crucial role in the angular dependence of the emission, which was noted in [163]. By examining the spatial and temporal emission of the bound state, it should be possible to determine its energy and decay rate for a given momentum $Q$.

In future work, it would be interesting to extend our results to $m$ magnon-bound states and to see how the decay rates of different magnon sectors compare to one another. Given our proof that the two-magnon bound state decay rate must lie within the continuum of decay rates, it seems likely that this would also be true for $m$ magnon states, and possibly also true for magnon states with larger spin and in systems of higher dimension. It would also be interesting to study different forms of dissipators and find systems where the bound state can have a decay rate that lies outside the two-magnon continuum.

## 6.6 Conclusions

We have studied the energies and decay rates of one and two free magnons and two-magnon bound states in an XXZ model with nonlocal dissipation. We have proved that in general the decay rate of the bound state must lie within the decay rate continuum of two free magnons. We have then examined three examples of dissipative bound states in more detail, first looking at two forms of the XY interaction and nonlocal dissipation analytically; a nearest-neighbour model and next-nearest-neighbour model. We have found that the inclusion of nonlocal dissipation leads to momentum dependent decay rates and changes in the energy of the bound state compared to a closed system or a system with local dissipation. The nonlocal dissipation also allows a higher degree of tunability in the energies and decay rates of the bound states. Finally, in our third example, we have numerically studied an experimentally realisable model to observe dissipative bound states using Rydberg dressed atoms coupled to a photonic crystal waveguide. This model demonstrated many key features of our simpler models

and could also be used to obtain our next-nearest-neighbour results within certain parameter regimes.

# Chapter 7

# Summary

In this thesis, we have studied a variety of novel non-equilibrium phenomena that can be found in driven two-level systems when coupled via near-field and far-field dipole interactions. In Chapter 3, we studied a system with near-field dipole interactions with both static and exchange nature under external drive, extending the results found in the undriven system [72]. We found that the non-equilibrium dynamics were oscillations which exhibited a bifurcation between dipole-dominated and Rabi-dominated oscillations. Despite the presence of dipole interactions which usually cause the oscillations to decohere, it was possible to still find regimes of collective behaviour when strongly driving the system for certain tilts of the dipoles and ratios of the Ising to XY dipole interaction.

In Chapter 4, we examined how the inclusion of dissipation fundamentally changed the dynamics of the system compared to Chapter 3. We found the inclusion of dissipation allowed more exotic forms of non-equilibrium phases such as antiferromagnetism, spin density waves, persistent oscillations and bistabilities within the mean-field approximation, and how these varied with the tuning of the Ising to XY interaction. We also compared small quantum systems and the mean-field phase diagram, finding key signatures of the mean-field through connected correlators and the distribution of expectation values. While these features had been touched upon in other mean-field studies, our results suggest these are generic features of dissipative spin systems. In Chapter 5, we studied the full resonant dipole-dipole interaction. We found the non-equilibrium phases that can arise with far-field dipole coupling beyond low intensity drive, which had not been identified before. We then explained how nonlocal dissipation was important in the formation of these non-equilibrium phases. As in Chapter 4, there was an emergence of many exotic phases, such as oscillations, bistabilities and

spin density waves and we also found that nonlocal dissipation causes the formation of more spin density waves and oscillations than in systems with local dissipation. We attributed this to the fact that the long-range dipole interactions allow the dipoles to oscillate out of phase and trap more photons in the system. Similarly to Chapter 4, we also found signatures of the mean-field in the full quantum picture.

Finally, in Chapter 6, we studied the dynamics of an open quantum system on approach to the steady state in a system with nonlocal dissipation and also static and exchange dipole moments. We focused on the dynamics of a two-magnon bound state, which now had a decay rate that depended on its momentum because of the nonlocal dissipation, and examined how it decays compared to two free magnons in the system. We proved that the bound state could not have a decay rate larger or smaller than the maximal or minimal decay rate of two free magnons for any arbitrary XY interaction and nonlocal dissipation. We then characterised the decay rates of the single magnons and bound states for a nearest-neighbour, next-nearest-neighbour and photonic crystal waveguide model.

## 7.1 Outlook

The biggest question raised in this thesis is the validity of the mean-field approximation. For Chapter 3 and the study of the closed system, we expect the mean-field to be accurate because of the highly classical nature of the non-equilibrium state that emerges at high drive. However, for the dissipative dynamics in Chapters 4 and 5, the applicability of the mean-field approximation is unclear. While it is expected to be valid for systems with high coordination number, such as systems with high spatial dimension or with all-to-all interactions, little is known about the validity of the mean-field approximation for power law interactions. We have shown that, in small quantum systems, some signatures of the mean-field can be found, such as the index of dispersion corresponding to regions of bistability. However, understanding in what regimes the mean-field approximation can be used will require much further work. As discussed at the end of Chapter 4, near-field dipole terms in the open quantum system seem to give results similar to that of a nearest-neighbour interaction. Therefore, given the fact the system is 1D, it may be possible to study this system using t-DMRG methods [133] to study larger systems and gain a better understanding of how strong these mean-field signatures become with larger system size. However, for the far-field

dipole system in Chapter 5, the long-range nature of the interactions makes these methods more difficult to implement and so others will have to be employed.

Understanding the validity of mean-field in the far-field dipole systems is of particular importance as there are currently many experimental efforts exploring the effects of dipole interactions in cold gas clouds [171, 172]. Experiments are still working on the low intensity limit, but are starting to move beyond this regime [173] and examine the effects of multiple excitations in disordered cold gases. Of particular interest is whether or not bistability can occur in these experiments and what signatures of this can be measured. By using the mean-field approximation, it should be possible to make clear predictions of what experimentalists may be able to measure, and simultaneously evaluate the applicability of mean-field by corroborating with experiment, which will be a natural extension of the work in Chapter 5.

Another route of further work would be to expand on the results of dissipative bound states in Chapter 6. While we proved that the decay rate of the bound states must lie within the two-magnon decay rate continuum, the possibility to study other forms of nonlocal dissipation and determine if they can result in a bound state with a higher or lower decay rate than the continuum would be interesting. Furthermore, we have only studied a nearest-neighbour Ising interaction and looked at a 1D system. Looking into longer-ranged Ising interactions and higher dimensions could lead to multiple bound states with even more exotic properties.

For all the chapters on open quantum systems, we have assumed both the Markov and Born approximations. However, there has been recent growing interest in relaxing these assumptions and studying non-markovian effects [174]. How these effects alter steady state phase diagrams or decay of excitations is largely unexplored. For all chapters, it is natural to ask how the key findings generalise to the inclusion of more energy levels, which results in larger spin systems. It would also be interesting to understand the effects of altering the underlying lattice geometry, where certain lattices, such as Kagome and triangular, lead to frustration effects between spins [175]. Finally, as briefly considered at the end of Chapter 3, it would also be useful to understand how the key findings of this thesis are altered by non-unity filling of the lattice and disorder due to small motional effects. These effects will be important for possible future experimental implementation.

# Appendix A

# Floquet Theory

Below we prove the key results from Floquet theory and how they relate to the stability of the system. For any Floquet equation, we can write the solutions in matrix form

$$\frac{d\mathbf{X}}{dt} = \mathbf{A}(t)\mathbf{X}, \tag{A.1}$$

with $\mathbf{X}(0) = \mathbf{I}$, where $\mathbf{I}$ is the indentity matrix. For any non-singular matrix $\mathbf{X}(t)$, we can find another matrix $\mathbf{Y}(t) = \mathbf{X}(t)\mathbf{B}$ that is also a solution to the equations where $B$ is some constant matrix

$$\begin{aligned} \mathbf{Y}'(t) &= \mathbf{X}'(t)\mathbf{B} \\ &= \mathbf{A}(t)\mathbf{X}(t)\mathbf{B} \\ &= \mathbf{A}(t)\mathbf{Y}(t). \end{aligned} \tag{A.2}$$

We can also show that $\mathbf{X}(t + nT)$, where $n$ is an integer, is a solution to Eq. (A.1) provided $\mathbf{A}(t)$ is periodic such that $\mathbf{A}(t + nT) = \mathbf{A}(t)$. We therefore have

$$\begin{aligned} \mathbf{X}'(t + nT) &= \mathbf{A}(t + nT)\mathbf{X}(t + nT) \\ &= \mathbf{A}(t)\mathbf{X}(t + nT). \end{aligned} \tag{A.3}$$

We can now define the matrix $\mathbf{Y}(t) = \mathbf{X}(t + nT)\mathbf{X}(nT)^{-1}$, which is immediately a solution to Eq. (A.1) because of our previous results. If $\mathbf{Y}(t)$ and $\mathbf{X}(t)$ are both solutions to Eq. (A.1), then because the solutions are unique, it must be the case that $\mathbf{Y}(t) = \mathbf{X}(t)$ and so $\mathbf{X}(t + nT) = \mathbf{X}(t)\mathbf{X}(nT)$. As an additional result, if we set $t = T$, we can show that $\mathbf{X}(nT) = \mathbf{X}(T)^n$. Therefore, $\mathbf{X}(t + nT) = \mathbf{X}(t)\mathbf{X}(T)^n$ and motivates

the definition of the constant matrix

$$\mathbf{B} = \mathbf{X}(T). \tag{A.4}$$

This is the Monodromy matrix whose eigenvalues give the Floquet multipliers, $\rho_l$. Each multiplier can be written as the exponent of a Floquet value. However, these values are not unique due to the addition of $2\pi i$ in the exponent.

We can show the multipliers relate to the stability of the orbits as follow. Let $\mathbf{b}_l$ be an eigenvector of $\mathbf{B}$, with $\mathbf{B}\mathbf{b}_l = \rho_l \mathbf{b}_l$, and let $\mathbf{x}(t)_l = \mathbf{X}(t)\mathbf{b}_l$. Then we have

$$\mathbf{x}(t+T)_l = \mathbf{X}(t+T)\mathbf{b}_l = \mathbf{X}(t)\mathbf{B}\mathbf{b}_l = \rho_l \mathbf{x}(t)_l. \tag{A.5}$$

Therefore, after time $T$, the solution to the Floquet equation becomes scaled by the multiplier. If we let time run for $nT$ times, we find

$$\mathbf{x}(t+nT) = \rho_l^n \mathbf{x}(t). \tag{A.6}$$

We can see then that if the multiplier is greater than one, the solution will diverge exponentially in time. If the multiplier is unity, the solution is periodic and if the multiplier is less than unity, the solution decays. i.e. the fluctuations die down. Therefore, the original solution is only stable if all multipliers are less than unity.

# Appendix B

# Deriving the Bound State Determinant Equation

Below, we outline the steps to obtain the bound state equation in Eq. (6.11). For an open quantum system, provided the Liouvillian operator is time independent, any Heisenberg operator, $\hat{A}_H(t)$ will obey the adjoint master equation, given by [94]

$$\frac{d\hat{A}_H(t)}{dt} = i[\hat{H}, \hat{A}_H(t)] + \sum_{i,l}^{N} \frac{\Gamma_{il}}{2} \left( 2\hat{\sigma}_l^+ \hat{A}_H(t) \hat{\sigma}_i^- - \left\{ \hat{\sigma}_l^+ \hat{\sigma}_i^-, \hat{A}_H(t) \right\} \right). \tag{B.1}$$

Therefore, the Green's function $\mathrm{Tr}\Big(\hat{A}_H(t)\hat{B}\hat{\rho}(0)\Big) = \langle 0| \hat{A}_H(t)\hat{B} |0\rangle$, with the initial condition $\hat{\rho}(0) = |0\rangle \langle 0|$, will obey

$$\langle 0| \frac{d\hat{A}_H(t)}{dt} \hat{B} |0\rangle = i \langle 0| \hat{A}_H(t)[\hat{B}, \hat{H}] |0\rangle - \sum_{i,l}^{N} \frac{\Gamma_{il}}{2} \langle 0| \hat{A}(t) \hat{\sigma}_l^+ \hat{\sigma}_i^- \hat{B} |0\rangle . \tag{B.2}$$

where $\hat{B} = \hat{B}_H(0)$ which is equivalent to the Schrodinger picture operator. For the two-magnon Green's function, $G(i,j,l,m;t) = \langle 0|\, \hat{\sigma}_i^-(t)\hat{\sigma}_j^-(t)\hat{\sigma}_l^+\hat{\sigma}_m^+ \,|0\rangle\, \Theta(t)$, this gives

$$\begin{aligned}
&\frac{dG(i,j,l,m;t)}{dt} - (1-\delta_{ij})\delta(t)(\delta_{il}\delta_{jm} + \delta_{im}\delta_{jl}) = \\
&\left(-2i\Delta + 4i\sum_{a\neq m}^{N} U_{am} + 4i\sum_{a\neq l}^{N} U_{al} - \Gamma - 8iU_{lm}\right) G(i,j,l,m;t) \\
&- i\sum_{p\neq l}^{N} J_{pl}G(i,j,p,m;t) - i\sum_{p\neq m}^{N} J_{pm}G(i,j,p,l;t) \\
&+ 2i\delta_{lm}\sum_{p\neq m}^{N} J_{pm}G(i,j,p,m;t),
\end{aligned} \tag{B.3}$$

where $J_{pl} = V_{pl} - i\Gamma_{pl}/2$. In order to solve Eq. (B.3), it will be useful to view it as a matrix equation [176] given by $(\boldsymbol{\mathcal{L}} + \boldsymbol{\delta\mathcal{L}})\boldsymbol{G} = \boldsymbol{\mu h}$, where the matrices are defined as

$$\begin{aligned}
&\mathcal{L}(l,m,p,v;t-t') = i\delta(t-t')\delta_{vm}J_{pl} + i\delta(t-t')\delta_{vl}J_{pm} + \\
&\delta(t-t')\delta_{pl}\delta_{vm}\left(\frac{d}{dt'} + 2i\Delta - 4i\sum_{a\neq m}^{N} U_{am} - 4i\sum_{a\neq l}^{N} U_{al} + \Gamma\right), \\
&\delta\mathcal{L}(l,m,p,v;t-t') = -i\delta(t-t')\delta_{pm}\delta_{lm}J_{vl} \\
&- i\delta(t-t')\delta_{vl}\delta_{lm}J_{pl} + 8i\delta(t-t')\delta_{pl}\delta_{vm}U_{pv}, \\
&h(i,j,p,v) = \delta_{ip}\delta_{jv}(1-\delta_{ij}), \\
&\mu(l,m,p,v;t-t') = \delta(t-t')(\delta_{pl}\delta_{vm} + \delta_{pm}\delta_{vl}),
\end{aligned} \tag{B.4}$$

To solve Eq. (B.3), we now follow the same steps taken by Wortis [144] by introducing the function $\Gamma(i,j,l,m;t) = G(i,l;t)G(j,m;t) + G(i,m;t)G(j,l;t)$, where $G(j,l;t)$ is the single magnon Green's function. We find that $\Gamma(i,j,l,m;t)$ obeys Eq. (B.3) without the last two terms and no $1-\delta_{ij}$ term. Viewed in terms of matrices, this means $\boldsymbol{\mathcal{L}\Gamma} = \boldsymbol{\mu}$ and so we can write $\boldsymbol{\mathcal{L}} = \boldsymbol{\mu\Gamma}^{-1}$. This allows Eq. (B.3) to be rewritten as

$$\begin{aligned}
&\Gamma(i,j,a,b;t)h(i,j) - G(i,j,a,b;t) \\
&= \int_{-\infty}^{\infty}\sum_{pv}^{N}\sum_{lm}^{N}\Gamma(l,m,a,b;t)\delta\mathcal{L}(l,m,p,v,t-t')G(i,j,p,v;t') \\
&= \int_{-\infty}^{\infty}\sum_{pv}^{N}K(a,b,p,v;t-t')G(i,j,p,v;t'),
\end{aligned} \tag{B.5}$$

where in the last line we have defined

$$\begin{aligned} K(a,b,p,v;t) &= 8iU_{pq}\Gamma(p,v,a,b;t) \\ &- i(J_{pv}/2)\left(\Gamma(v,v,a,b;t)+\Gamma(p,p,a,b;t)\right). \end{aligned} \tag{B.6}$$

In order to obtain the bound state solutions, we now need to partially Fourier transform Eq. (B.5). The Fourier transform of $\Gamma(i,j,a,b;t)$ is given by

$$\Gamma(i,j,a,b;\Omega) = \int_{-\infty}^{\infty} \Gamma(i,j,a,b;t)e^{i\Omega t}dt. \tag{B.7}$$

By using the definition of $\Gamma(i,j,a,b;t)$ and the Fourier transform of the single magnon Green's function, this can be written as

$$\begin{aligned} \Gamma(i,j,a,b;\Omega) = \sum_{k_1\in BZ}\sum_{k_2\in BZ}\left(\frac{e^{ik_1r_{ia}+ik_2r_{jb}}+e^{ik_1r_{ib}+ik_2r_{ja}}}{N}\right)\times \\ \int_{-\infty}^{\infty}\int_{-\infty}^{\infty}\int_{-\infty}^{\infty}\tilde{G}(k_1,\omega_1)\tilde{G}(k_2,\omega_2)e^{i(\Omega-\omega_1-\omega_2)t}dt\frac{d\omega_1}{2\pi}\frac{d\omega_2}{2\pi}, \end{aligned} \tag{B.8}$$

where $r_{ia} = r_i - r_a$. We now rewrite the momentum sums using the sum and difference of momenta, $Q = k_1 + k_2$ and $q = (k_1 - k_2)/2$, and also the sum and difference of coordinates $R = (r_i + r_j)/2$, $r = r_i - r_j$ and $R' = (r_a + r_b)/2$, $r' = r_a - r_b$. Once we evaluate the frequency integrals, we then obtain

$$\begin{aligned} \Gamma(i,j,a,b;\Omega) &= \sum_{Q\in BZ} e^{iQ(R-R')}\left(-\frac{2i}{N}\sum_{q\in BZ}\frac{\cos(qr)\cos(qr')}{\Omega - S(q,Q)}\right) \\ &= \sum_{Q\in BZ} e^{iQ(R-R')}\Gamma(r,r';Q,\Omega), \end{aligned} \tag{B.9}$$

where $S(q,Q)$ is the two free magnon dispersion, defined in Eq. (6.9) in the main text. Similarly, we can Fourier transform and rewrite $K(l,m,p,q;t)$ as

$$\begin{aligned} K(a,b,p,v;\Omega) = \sum_{Q\in BZ} e^{iQ(R'-R'')}\sum_{q\in BZ}\frac{2i}{N}\frac{\cos(qr'')}{\Omega - S(q,Q)}\times \\ \left(8iU(r')\cos(qr') - 2i\left(V(r') - i\frac{\Gamma(r')}{2}\right)\cos(Qr'/2)\right) \\ = \sum_{Q\in BZ} e^{iQ(R'-R'')}K(r',r'';Q,\Omega). \end{aligned} \tag{B.10}$$

where $R'' = (r_p + r_v)/2$ and $r'' = r_p - r_v$. Transforming Eq. (B.5) by inserting the results of Eq. (B.9) and Eq. (B.10) gives

$$\begin{aligned}\frac{1}{N}\int_{-\infty}^{\infty} dt \sum_{Q\in BZ} e^{iQ(R-R')}e^{-i\Omega t}\Big[G(r,r',Q,\Omega)- \\ \Gamma(r,r',Q,\Omega)h(r) + \sum_{r''}^{N} K(r,r'',Q,\Omega)G(r',r'',Q,\Omega)\Big] = 0.\end{aligned} \tag{B.11}$$

This equation is obeyed provided we set the integrand to zero such that

$$\begin{aligned}&\sum_{r''}^{N}\Big[\delta_{r'r''} + K(r',r'',Q,\Omega)\Big]G(r,r'',Q,\Omega) \\ &= \Gamma(r,r',Q,\Omega)h(r).\end{aligned} \tag{B.12}$$

The bound state solutions are found when the determinant of the matrix $\delta_{r'r''} + K(r',r'',Q,\Omega)$ is singular, which means $G(r,r'',Q,\Omega)$ cannot be written as the sum of two free magnon solutions. The bound state solutions are therefore solutions to

$$\begin{aligned}\det\Bigg[\delta_{r'r''} - \frac{2}{N}\sum_{q\in BZ} 8U(r')\frac{\cos(qr')\cos(qr'')}{\Omega - S(q,Q)} + \\ \frac{2}{N}\sum_{q\in BZ}\left[2V(r') - i\Gamma(r')\right]\frac{\cos(Qr'/2)\cos(qr'')}{\Omega - S(q,Q)}\Bigg] = 0.\end{aligned} \tag{B.13}$$

If the Ising interaction is nearest-neighbour such that $U_{il} = J_z\delta_{l,i+1}/2$, we can simplify the determinant in Eq. (B.13) to obtain Eq. (6.11) in the main text.

To simplify the determinant, we first define the Ising and XY matrices,

$$\begin{aligned}ZZ_{rr'} &= -\frac{8J_z}{N}\sum_{q\in BZ}\frac{\cos(qr)\cos(qr')\delta_{r',1}}{\Omega - S(q,Q)} \\ XY_{rr'} &= A_r B_{r'},\end{aligned} \tag{B.14}$$

where

$$\begin{aligned}A_r &= \frac{4}{N}\sum_{q\in BZ}\frac{\cos(qr)}{\Omega - S(q,Q)} \\ B_{r'} &= \left(V(r') - i\frac{\Gamma(r')}{2}\right)\cos(Qr'/2).\end{aligned} \tag{B.15}$$

This allows us to rewrite the determinant condition, Eq. (B.13), as

$$\begin{aligned}
&\det(\boldsymbol{I}+\boldsymbol{ZZ}+\boldsymbol{XY}) \\
&= \left|\begin{pmatrix} B_1A_1+ZZ_{11}+1 & B_2A_1 & . & . & B_NA_1 \\ B_1A_2+ZZ_{21} & B_2A_2+1 & . & . & B_NA_2 \\ . & . & . & . & . \\ . & . & . & . & . \\ B_1A_N+ZZ_{N1} & B_2A_N & . & . & B_NA_N+1 \end{pmatrix}\right| \\
&= \left|\begin{pmatrix} A_1+\frac{ZZ_{11}}{B_1}+\frac{1}{B_1} & A_1 & . & . & A_1 \\ A_2+\frac{ZZ_{21}}{B_1} & A_2+\frac{1}{B_2} & . & . & A_2 \\ . & . & . & . & . \\ . & . & . & . & . \\ A_N+\frac{ZZ_{N1}}{B_1} & A_N & . & . & A_N+\frac{1}{B_N} \end{pmatrix}\right| B_1..B_N.
\end{aligned} \tag{B.16}$$

The determinant can be simplified by subtracting the last column from all the other columns, $\mathrm{C}_1-\mathrm{C}_N$, $\mathrm{C}_2-\mathrm{C}_N$,...$\mathrm{C}_{N-1}-\mathrm{C}_N$, giving

$$\begin{aligned}
&(ZZ_{11}+1)\left|\begin{pmatrix} 1 & 0 & . & . & 0 & B_NA_2 \\ 0 & 1 & . & . & . & . \\ . & . & . & . & . & . \\ . & . & . & . & 0 & . \\ 0 & . & . & 0 & 1 & . \\ -\frac{B_1}{B_N} & . & . & . & . & B_NA_N+1 \end{pmatrix}\right| \\
&+(-1)^N(B_NA_1)\left|\begin{pmatrix} ZZ_{21} & 1 & 0 & . & . & 0 \\ ZZ_{31} & 0 & 1 & . & . & . \\ . & . & . & . & . & . \\ . & . & . & . & . & 0 \\ ZZ_{(N-1)1} & 0 & . & . & 0 & 1 \\ ZZ_{N1}-\frac{B_1}{B_N} & -\frac{B_2}{B_N} & . & . & . & -\frac{B_{N-1}}{B_N} \end{pmatrix}\right|,
\end{aligned} \tag{B.17}$$

where we partially Laplace expand the determinant. For the first determinant, we can swap the first and last column, $C_1 \leftrightarrow C_N$ and then swap the first and last row, $R_1 \leftrightarrow R_N$. In the second determinant, we can carry out the row-swap operation, $R_N \leftrightarrow R_{N-1}$, followed by $R_{N-1} \leftrightarrow R_{N-2}$, $R_{N-2} \leftrightarrow R_{N-3}$ etc. until the last row

becomes the first row. This then gives

$$(ZZ_{11}+1)\begin{vmatrix}\begin{pmatrix} B_NA_N+1 & -\frac{B_3}{B_N} & . & . & -\frac{B_{N-1}}{B_N} & -\frac{B_2}{B_N} \\ B_3A_3 & 1 & 0 & . & . & 0 \\ . & 0 & 1 & . & . & . \\ . & . & . & . & . & . \\ B_{N-1}A_{N-1} & . & . & . & . & . \\ B_2A_2 & 0 & . & . & 0 & 1 \end{pmatrix}\end{vmatrix}$$

$$-(B_NA_1)\begin{vmatrix}\begin{pmatrix} ZZ_{N1}-\frac{B_1}{B_N} & -\frac{B_2}{B_N} & -\frac{B_3}{B_N} & . & . & \frac{B_{N-1}}{B_N} \\ ZZ_{21} & 1 & 0 & . & . & 0 \\ . & 0 & 1 & . & . & . \\ . & . & . & . & . & . \\ ZZ_{(N-2)1} & . & . & . & . & 0 \\ ZZ_{(N-1)1} & 0 & . & . & 0 & 1 \end{pmatrix}\end{vmatrix}, \tag{B.18}$$

which are the determinants of arrowhead matrices, where an arrowhead matrix is a matrix of the form

$$\boldsymbol{G}=\begin{pmatrix} a & b_2 & b_3 & . & . & b_N \\ c_2 & d_2 & 0 & . & . & 0 \\ c_3 & 0 & d_3 & . & . & . \\ . & . & . & . & . & . \\ . & . & . & . & . & . \\ c_N & 0 & . & . & . & d_N \end{pmatrix}. \tag{B.19}$$

Using the Sherman-Morrison-Woodbury formula, we can evaluate the determinant of the arrowhead matrix by rewriting Eq. (B.19) as

$$\begin{aligned}\det(\boldsymbol{G}) &= det(\boldsymbol{A}+\boldsymbol{C}\boldsymbol{B}^T) \\ &= \det\Big(\boldsymbol{I}+\boldsymbol{B}^T\boldsymbol{A}^{(-1)}\boldsymbol{C}\Big)det(\boldsymbol{A}),\end{aligned} \tag{B.20}$$

where

$$\begin{aligned}
\boldsymbol{A} &= \begin{pmatrix} a & 0 & 0 & . & . & 0 \\ 0 & d_2 & 0 & . & . & 0 \\ 0 & 0 & . & . & . & . \\ . & . & . & . & . & . \\ 0 & 0 & . & . & . & d_N \end{pmatrix}, \\
\boldsymbol{B} &= \begin{pmatrix} b_1 & b_2 & b_3 & . & . & b_N \\ 1 & 0 & 0 & . & . & 0 \end{pmatrix}, \\
\boldsymbol{C}^T &= \begin{pmatrix} c_1 & c_2 & c_3 & . & . & c_N \\ 1 & 0 & 0 & . & . & 0 \end{pmatrix}.
\end{aligned} \tag{B.21}$$

Using this gives a determinant of

$$\det(\boldsymbol{G}) = \left[ a - \sum_{i=2}^{N} \frac{b_i c_i}{d_i} \right] \prod_{i=2}^{N} d_i. \tag{B.22}$$

Substituting the values of $a$, $b_i$, $c_i$ and $d_i$ for the two arrowhead matrices in Eq. (B.18), we obtain the determinant equation

$$\det(\boldsymbol{G}) = (ZZ_{11} + 1)(1 + \mathrm{Tr}(\boldsymbol{XY})) - A_1 \sum_{i=1}^{N} ZZ_{i1} B_i. \tag{B.23}$$

Once we plug in the definitions of $\boldsymbol{ZZ}$ and $\boldsymbol{XY}$ into Eq. (B.23), we obtain Eq. (6.11) in the main text.

# Bibliography


[1] C. D. Parmee and N. R. Cooper, Phys. Rev. A **95**, 033631 (2017).

[2] C. D. Parmee and N. R. Cooper, Phys. Rev. A **97**, 053616 (2018).

[3] C. D. Parmee and N. R. Cooper, arXiv:1812.07893 .

[4] The Nobel Prize in Physics 1997, https://www.nobelprize.org/prizes/physics/1997/summary/ (accessed 30/03/2019) .

[5] The Nobel Prize in Physics 2001, https://www.nobelprize.org/prizes/physics/2001/summary/ (accessed 30/03/19) .

[6] R. P. Feynman, Int. J. Theor. Phys. **21**, 467 (1982).

[7] I. Bloch, Nat. Phys. **1**, 23 (2005).

[8] L. Guidoni, C. Triché, P. Verkerk, and G. Grynberg, Phys. Rev. Lett. **79**, 3363 (1997).

[9] V. Galitski, G. Juzeliūnas, and I. B. Spielman, Phys. Today **72**, 38 (2019).

[10] C. Gross and I. Bloch, Science (80-. ). **357**, 995 (2017).

[11] M. Lewenstein, A. Sanpera, V. Ahufinger, B. Damski, A. Sen(De), and U. Sen, Adv. Phys. **56**, 243 (2007).

[12] D. Jaksch and P. Zoller, Ann. Phys. (N. Y). **315**, 52 (2005).

[13] L.-M. Duan, E. Demler, and M. D. Lukin, Phys. Rev. Lett. **91**, 090402 (2003).

[14] A. Altland and B. D. Simons, *Condensed Matter Field Theory* (Cambridge University Press, Cambridge, 2010).

[15] A. M. Rey, P. Cheinet, I. Bloch, M. D. Lukin, E. A. Demler, M. Feld, U. Schnorrberger, S. Trotzky, S. Folling, and A. Polkovnikov, Science (80-. ). **319**, 295 (2007).

[16] M. A. Cazalilla and A. M. Rey, Reports Prog. Phys. **77**, 124401 (2014).

[17] S. Sachdev, K. Sengupta, and S. M. Girvin, Phys. Rev. B **66**, 075128 (2002).

[18] J. Simon, W. S. Bakr, R. Ma, M. E. Tai, P. M. Preiss, and M. Greiner, Nature **472**, 307 (2011).

[19] M. Martin, N. Lemke, J. Ye, A. Rey, M. Bishof, A. Ludlow, A. Gorshkov, M. Swallows, C. Benko, X. Zhang, and C. Kraus, Ann. Phys. (N. Y). **340**, 311 (2013).

[20] X. Zhang, M. Bishof, S. L. Bromley, C. V. Kraus, M. S. Safronova, P. Zoller, A. M. Rey, and J. Ye, Science (80-. ). **345**, 1467 (2014).

[21] B. Olmos, D. Yu, Y. Singh, F. Schreck, K. Bongs, and I. Lesanovsky, Phys. Rev. Lett. **110**, 143602 (2013).

[22] A. V. Gorshkov, S. R. Manmana, G. Chen, E. Demler, M. D. Lukin, and A. M. Rey, Phys. Rev. A **84**, 033619 (2011).

[23] R. Barnett, D. Petrov, M. Lukin, and E. Demler, Phys. Rev. Lett. **96**, 190401 (2006).

[24] M. L. Wall, K. R. A. Hazzard, and A. M. Rey, in *From At. to Mesoscale*, Vol. 80309 (World Scientific, 2015) pp. 3–37.

[25] T. F. Gallagher, *Rydberg Atoms* (Cambridge University Press, Cambridge, 1994).

[26] A. W. Glaetzle, M. Dalmonte, R. Nath, C. Gross, I. Bloch, and P. Zoller, Phys. Rev. Lett. **114**, 173002 (2015).

[27] P. Schauss, Quantum Sci. Technol. **3**, 023001 (2018).

[28] H. Weimer, M. Müller, I. Lesanovsky, P. Zoller, and H. P. Büchler, Nat. Phys. **6**, 382 (2010).

[29] S. Whitlock, A. W. Glaetzle, and P. Hannaford, J. Phys. B At. Mol. Opt. Phys. **50**, 074001 (2017).

[30] T. L. Nguyen, J. M. Raimond, C. Sayrin, R. Cortiñas, T. Cantat-Moltrecht, F. Assemat, I. Dotsenko, S. Gleyzes, S. Haroche, G. Roux, T. Jolicoeur, and M. Brune, Phys. Rev. X **8**, 011032 (2018).

[31] I. M. Georgescu, S. Ashhab, and F. Nori, Rev. Mod. Phys. **86**, 153 (2014).

[32] J. I. Cirac and P. Zoller, Phys. Rev. Lett. **74**, 4091 (1995).

[33] R. Blatt and C. F. Roos, Nat. Phys. **8**, 277 (2012).

[34] A. Kay and D. G. Angelakis, EPL **84**, 20001 (2008).

[35] M. Hartmann, F. Brandão, and M. Plenio, Laser Photonics Rev. **2**, 527 (2008).

[36] G. Wendin, Reports Prog. Phys. **80**, 106001 (2017).

[37] U. L. Heras, A. Mezzacapo, L. Lamata, S. Filipp, A. Wallraff, and E. Solano, Phys. Rev. Lett. **112**, 200501 (2014).

[38] H. Bernien, B. Hensen, W. Pfaff, G. Koolstra, M. S. Blok, L. Robledo, T. H. Taminiau, M. Markham, D. J. Twitchen, L. Childress, and R. Hanson, Nature **497**, 86 (2013).

[39] A. Albrecht, A. Retzker, F. Jelezko, and M. B. Plenio, New J. Phys. **15**, 083014 (2013).

[40] J. Cai, A. Retzker, F. Jelezko, and M. B. Plenio, Nat. Phys. **9**, 168 (2013).

[41] X. Zhang, H.-O. Li, K. Wang, G. Cao, M. Xiao, and G.-P. Guo, Chinese Phys. B **27**, 020305 (2018).

[42] P. Barthelemy and L. M. K. Vandersypen, Ann. Phys. **525**, 808 (2013).

[43] M. Gring, M. Kuhnert, T. Langen, T. Kitagawa, B. Rauer, M. Schreitl, I. Mazets, D. A. Smith, E. Demler, and J. Schmiedmayer, Science (80-. ). **337**, 1318 (2012).

[44] J. Smith, A. Lee, P. Richerme, B. Neyenhuis, P. W. Hess, P. Hauke, M. Heyl, D. A. Huse, and C. Monroe, Nat. Phys. **12**, 907 (2016).

[45] M. Srednicki, Phys. Rev. E **50**, 888 (1994).

[46] J. Eisert, M. Friesdorf, and C. Gogolin, Nat. Phys. **11**, 124 (2015).

[47] P. Reimann, Nat. Commun. **7**, 10821 (2016).

[48] R. Nandkishore and D. A. Huse, Annu. Rev. Condens. Matter Phys. **6**, 15 (2015).

[49] T. Langen, R. Geiger, and J. Schmiedmayer, Annu. Rev. Condens. Matter Phys. **6**, 201 (2015).

[50] T. Ota, G. Yusa, N. Kumada, S. Miyashita, T. Fujisawa, and Y. Hirayama, Appl. Phys. Lett. **91**, 193101 (2007).

[51] B. Olmos, M. Müller, and I. Lesanovsky, New J. Phys. **12**, 013024 (2010).

[52] F. Jin, T. Neuhaus, K. Michielsen, S. Miyashita, M. A. Novotny, M. I. Katsnelson, and H. De Raedt, New J. Phys. **15**, 033009 (2013).

[53] K. R. A. Hazzard, B. Gadway, M. Foss-Feig, B. Yan, S. A. Moses, J. P. Covey, N. Y. Yao, M. D. Lukin, J. Ye, D. S. Jin, and A. M. Rey, Phys. Rev. Lett. **113**, 195302 (2014).

[54] A. Fedorov and L. Fedichkin, J. Phys. Condens. Matter **18**, 3217 (2006).

[55] C. Ates, J. P. Garrahan, and I. Lesanovsky, Phys. Rev. Lett. **108**, 110603 (2012).

[56] I. Lesanovsky, B. Olmos, and J. P. Garrahan, Phys. Rev. Lett. **105**, 100603 (2010).

[57] T. Kinoshita, T. Wenger, and D. S. Weiss, Nature **440**, 900 (2006).

[58] M. Müller, S. Diehl, G. Pupillo, and P. Zoller, in *Adv. At. Mol. Opt. Phys.*, Vol. 61 (2012) pp. 1–80.

[59] J. T. Barreiro, M. Müller, P. Schindler, D. Nigg, T. Monz, M. Chwalla, M. Hennrich, C. F. Roos, P. Zoller, and R. Blatt, Nature **470**, 486 (2011).

[60] I. Rotter and J. P. Bird, Reports Prog. Phys. **78**, 114001 (2015).

[61] B. Yan, S. A. Moses, B. Gadway, J. P. Covey, K. R. A. Hazzard, A. M. Rey, D. S. Jin, and J. Ye, Nature **501**, 521 (2013).

[62] H. Labuhn, D. Barredo, S. Ravets, S. de Léséleuc, T. Macrì, T. Lahaye, and A. Browaeys, Nature **534**, 667 (2016).

[63] T. Fukuhara, P. Schauß, M. Endres, S. Hild, M. Cheneau, I. Bloch, and C. Gross, Nature **502**, 76 (2013).

[64] D. Peter, *Quantum states with topological properties via dipolar interactions*, Ph.D. thesis, University of Stuttgart (2015).

[65] D. Maxwell, D. J. Szwer, D. Paredes-Barato, H. Busche, J. D. Pritchard, A. Gauguet, K. J. Weatherill, M. P. A. Jones, and C. S. Adams, Phys. Rev. Lett. **110**, 103001 (2013).

[66] D. Maxwell, D. J. Szwer, D. Paredes-Barato, H. Busche, J. D. Pritchard, A. Gauguet, M. P. A. Jones, and C. S. Adams, Phys. Rev. A **89**, 043827 (2014).

[67] D. Barredo, H. Labuhn, S. Ravets, T. Lahaye, A. Browaeys, and C. S. Adams, Phys. Rev. Lett. **114**, 113002 (2015).

[68] S. Bettelli, D. Maxwell, T. Fernholz, C. S. Adams, I. Lesanovsky, and C. Ates, Phys. Rev. A **88**, 043436 (2013).

[69] A. V. Gorshkov, S. R. Manmana, G. Chen, J. Ye, E. Demler, M. D. Lukin, and A. M. Rey, Phys. Rev. Lett. **107**, 115301 (2011).

[70] A. Micheli, G. K. Brennen, and P. Zoller, Nat. Phys. **2**, 341 (2006).

[71] J. Schachenmayer, I. Lesanovsky, A. Micheli, and A. J. Daley, New J. Phys. **13**, 059503 (2011).

[72] M. P. Kwasigroch and N. R. Cooper, Phys. Rev. A **90**, 021605 (2014).

[73] B. C. den Hertog and M. J. P. Gingras, Phys. Rev. Lett. **84**, 3430 (2000).

[74] D. C. Johnston, Phys. Rev. B **93**, 014421 (2016).

[75] J. Keaveney, A. Sargsyan, U. Krohn, I. G. Hughes, D. Sarkisyan, and C. S. Adams, Phys. Rev. Lett. **108**, 173601 (2012).

[76] R. Friedberg, S. Hartmann, and J. Manassah, Phys. Rep. **7**, 101 (1973).

[77] R. H. Dicke, Phys. Rev. **93**, 99 (1954).

[78] M. Gross and S. Haroche, Phys. Rep. **93**, 301 (1982).

[79] B. Zhu, J. Cooper, J. Ye, and A. M. Rey, Phys. Rev. A **94**, 023612 (2016).

[80] Y. A. Fofanov, A. S. Kuraptsev, I. M. Sokolov, and M. D. Havey, Phys. Rev. A **84**, 053811 (2011).

[81] R. T. Sutherland and F. Robicheaux, Phys. Rev. A **93**, 023407 (2016).

[82] T. Bienaimé, N. Piovella, and R. Kaiser, Phys. Rev. Lett. **108**, 123602 (2012).

[83] T. Bienaimé, R. Bachelard, N. Piovella, and R. Kaiser, Fortschritte der Phys. **61**, 377 (2013).

[84] M. D. Lee, S. D. Jenkins, and J. Ruostekoski, Phys. Rev. A **93**, 063803 (2016).

[85] W. Guerin, M. O. Araújo, and R. Kaiser, Phys. Rev. Lett. **116**, 083601 (2016).

[86] S. D. Jenkins, J. Ruostekoski, J. Javanainen, S. Jennewein, R. Bourgain, J. Pellegrino, Y. R. P. Sortais, and A. Browaeys, Phys. Rev. A **94**, 023842 (2016).

[87] J. Pellegrino, R. Bourgain, S. Jennewein, Y. R. P. Sortais, A. Browaeys, S. D. Jenkins, and J. Ruostekoski, Phys. Rev. Lett. **113**, 133602 (2014).

[88] S. Jennewein, M. Besbes, N. J. Schilder, S. D. Jenkins, C. Sauvan, J. Ruostekoski, J.-J. Greffet, Y. R. P. Sortais, and A. Browaeys, Phys. Rev. Lett. **116**, 233601 (2016).

[89] S. D. Jenkins and J. Ruostekoski, Phys. Rev. A **86**, 031602 (2012).

[90] R. J. Bettles, S. A. Gardiner, and C. S. Adams, Phys. Rev. A **92**, 063822 (2015).

[91] W. Feng, D.-W. Wang, H. Cai, S.-Y. Zhu, and M. O. Scully, Phys. Rev. A **95**, 033845 (2017).

[92] G. Facchinetti, S. D. Jenkins, and J. Ruostekoski, Phys. Rev. Lett. **117**, 243601 (2016).

[93] R. J. Bettles, S. A. Gardiner, and C. S. Adams, Phys. Rev. Lett. **116**, 103602 (2016).

[94] H.-P. Breuer and F. Petruccione, *The Theory of Open Quantum Systems* (Oxford University Press, 2007).

[95] B. Kraus, H. P. Büchler, S. Diehl, A. Kantian, A. Micheli, and P. Zoller, Phys. Rev. A **78**, 042307 (2008).

[96] D. Peter, S. Müller, S. Wessel, and H. P. Büchler, Phys. Rev. Lett. **109**, 025303 (2012).

[97] P. Bak and R. Bruinsma, Phys. Rev. Lett. **49**, 249 (1982).

[98] P. Hauke, F. M. Cucchietti, A. Müller-Hermes, M.-C. Bañuls, J. Ignacio Cirac, and M. Lewenstein, New J. Phys. **12**, 113037 (2010).

[99] J. Schachenmayer, A. Pikovski, and A. M. Rey, Phys. Rev. X **5**, 011022 (2015).

[100] J. P. Á. Zúñiga, G. Lemarié, and N. Laflorencie, in *AIP Conf. Proc.*, Vol. 1610 (2014) pp. 102–107.

[101] S. Wiggins, *Introduction to Applied Nonlinear Dynamical Systems and Chaos*, edited by F. John, J. E. Marsden, L. Sirovich, M. Golubitsky, and W. Jager (Springer-Verlag, New York, 1990).

[102] N. Goldman and J. Dalibard, Phys. Rev. X **4**, 031027 (2014).

[103] L. Bonsall and A. A. Maradudin, Phys. Rev. B **15**, 1959 (1977).

[104] T. Kuwahara, T. Mori, and K. Saito, Ann. Phys. (N. Y). **367**, 96 (2016).

[105] M. Kitagawa and M. Ueda, Phys. Rev. A **47**, 5138 (1993).

[106] C. Chan, T. E. Lee, and S. Gopalakrishnan, Phys. Rev. A **91**, 051601 (2015).

[107] T. E. Lee, H. Häffner, and M. C. Cross, Phys. Rev. A **84**, 031402 (2011).

[108] R. M. Wilson, K. W. Mahmud, A. Hu, A. V. Gorshkov, M. Hafezi, and M. Foss-Feig, Phys. Rev. A **94**, 033801 (2016).

[109] T. E. Lee, S. Gopalakrishnan, and M. D. Lukin, Phys. Rev. Lett. **110**, 257204 (2013).

[110] J. Qian, G. Dong, L. Zhou, and W. Zhang, Phys. Rev. A **85**, 065401 (2012).

[111] J. Qian, L. Zhang, J. Zhai, and W. Zhang, Phys. Rev. A **92**, 063407 (2015).

[112] C. Carr, R. Ritter, C. G. Wade, C. S. Adams, and K. J. Weatherill, Phys. Rev. Lett. **111**, 113901 (2013).

[113] N. Šibalić, C. G. Wade, C. S. Adams, K. J. Weatherill, and T. Pohl, Phys. Rev. A **94**, 011401 (2016).

[114] H. Weimer, Phys. Rev. Lett. **114**, 040402 (2015).

[115] M. F. Maghrebi and A. V. Gorshkov, Phys. Rev. B **93**, 014307 (2016).

[116] J. Jin, A. Biella, O. Viyuela, L. Mazza, J. Keeling, R. Fazio, and D. Rossini, Phys. Rev. X **6**, 031011 (2016).

[117] M. Sadrzadeh and A. Langari, J. Phys. Conf. Ser. **969**, 012114 (2018).

[118] E. T. Owen, J. Jin, D. Rossini, R. Fazio, and M. J. Hartmann, New J. Phys. **20**, 045004 (2018).

[119] M. Hoening, W. Abdussalam, M. Fleischhauer, and T. Pohl, Phys. Rev. A **90**, 021603 (2014).

[120] M. Höning, D. Muth, D. Petrosyan, and M. Fleischhauer, Phys. Rev. A **87**, 023401 (2013).

[121] J. J. Mendoza-Arenas, S. R. Clark, S. Felicetti, G. Romero, E. Solano, D. G. Angelakis, and D. Jaksch, Phys. Rev. A **93**, 023821 (2016).

[122] C. Joshi, F. Nissen, and J. Keeling, Phys. Rev. A **88**, 063835 (2013).

[123] A. Hu, T. E. Lee, and C. W. Clark, Phys. Rev. A **88**, 053627 (2013).

[124] S. G. Schirmer and X. Wang, Phys. Rev. A **81**, 062306 (2010).

[125] T. E. Lee, H. Häffner, and M. C. Cross, Phys. Rev. Lett. **108**, 023602 (2012).

[126] B. Olmos, D. Yu, and I. Lesanovsky, Phys. Rev. A **89**, 023616 (2014).

[127] C. Ates, B. Olmos, J. P. Garrahan, and I. Lesanovsky, Phys. Rev. A **85**, 043620 (2012).

[128] C. Savage and H. Carmichael, IEEE J. Quantum Electron. **24**, 1495 (1988).

[129] A. J. Daley, Adv. Phys. **63**, 77 (2014).

[130] C. Navarrete-Benlloch, arXiv:1504.05266 .

[131] M. A. Armen and H. Mabuchi, Phys. Rev. A **73**, 063801 (2006).

[132] J. Jin, D. Rossini, M. Leib, M. J. Hartmann, and R. Fazio, Phys. Rev. A **90**, 023827 (2014).

[133] U. Schollwöck, Rev. Mod. Phys. **77**, 259 (2005).

[134] W. D. Newman, C. L. Cortes, A. Afshar, K. Cadien, A. Meldrum, R. Fedosejevs, and Z. Jacob, Sci. Adv. **4**, eaar5278 (2018).

[135] P. Solano, P. Barberis-Blostein, F. K. Fatemi, L. A. Orozco, and S. L. Rolston, Nat. Commun. **8**, 1857 (2017).

[136] R. Jones, R. Saint, and B. Olmos, J. Phys. B At. Mol. Opt. Phys. **50**, 014004 (2017).

[137] D. Yu, Phys. Rev. A **89**, 063809 (2014).

[138] D. Yu, J. Mod. Opt. **63**, 428 (2016).

[139] D. F. V. James, Phys. Rev. A **47**, 1336 (1993).

[140] R. J. Bettles, *Cooperative Interactions in Lattices of Atomic Dipoles*, Ph.D. thesis (2016).

[141] K. Ogata, *Modern Control Engineering*, 3rd ed., edited by A. Dworkin and A. M. Longobardo (Prentice Hall, New Jersey, 1997).

[142] W. Liu, J. Math. Anal. Appl. **182**, 250 (1994).

[143] H. Bethe, Zeitschrift f\"ur Phys. **71**, 205 (1931).

[144] M. Wortis, Phys. Rev. **132**, 85 (1963).

[145] F. D. M. Haldane, J. Phys. C Solid State Phys. **15**, L1309 (1982).

[146] B. W. Southern, R. J. Lee, and D. A. Lavis, J. Phys. Condens. Matter **6**, 10075 (1994).

[147] T. Schneider, Phys. Rev. B **24**, 5327 (1981).

[148] J. B. Torrance and M. Tinkham, Phys. Rev. **187**, 587 (1969).

[149] C. K. Majumdar, J. Math. Phys. **10**, 177 (1969).

[150] I. Ono, S. Mikado, and T. Oguchi, J. Phys. Soc. Japan **30**, 358 (1971).

[151] F. Letscher and D. Petrosyan, Phys. Rev. A **97**, 043415 (2018).

[152] L. Kecke, T. Momoi, and A. Furusaki, Phys. Rev. B **76**, 060407 (2007).

[153] X. Qin, F. Mei, Y. Ke, L. Zhang, and C. Lee, Phys. Rev. B **96**, 195134 (2017).

[154] X. Qin, F. Mei, Y. Ke, L. Zhang, and C. Lee, New J. Phys. **20**, 013003 (2018).

[155] A. Agarwala and D. Sen, Phys. Rev. B **96**, 104309 (2017).

[156] K. Kudo, T. Boness, and T. S. Monteiro, Phys. Rev. A **80**, 063409 (2009).

[157] J. Barker, U. Atxitia, T. A. Ostler, O. Hovorka, O. Chubykalo-Fesenko, and R. W. Chantrell, Sci. Rep. **3**, 3262 (2013).

[158] C. B. Krimphoff, M. Haque, and A. M. Läuchli, Phys. Rev. B **95**, 144308 (2017).

[159] M. Ganahl, E. Rabel, F. H. L. Essler, and H. G. Evertz, Phys. Rev. Lett. **108**, 077206 (2012).

[160] J. Mölter, T. Barthel, U. Schollwöck, and V. Alba, J. Stat. Mech. Theory Exp. **2014**, P10029 (2014).

[161] P. Longo and J. Evers, Phys. Rev. Lett. **112**, 193601 (2014).

[162] C. W. Hsu, B. Zhen, A. D. Stone, J. D. Joannopoulos, and M. Soljačić, Nat. Rev. Mater. **1**, 16048 (2016).

[163] P. Longo and J. Evers, Phys. Rev. A **90**, 063834 (2014).

[164] M. J. Hartmann, J. Opt. **18**, 104005 (2016).

[165] J. D. Hood, A. Goban, A. Asenjo-Garcia, M. Lu, S.-P. Yu, D. E. Chang, and H. J. Kimble, Proc. Natl. Acad. Sci. **113**, 10507 (2016).

[166] A. Goban, C.-L. Hung, S.-P. Yu, J. Hood, J. Muniz, J. Lee, M. Martin, A. McClung, K. Choi, D. Chang, O. Painter, and H. Kimble, Nat. Commun. **5**, 3808 (2014).

[167] J. S. Douglas, H. Habibian, C.-L. Hung, A. V. Gorshkov, H. J. Kimble, and D. E. Chang, Nat. Photonics **9**, 326 (2015).

[168] A. González-Tudela, C.-L. Hung, D. E. Chang, J. I. Cirac, and H. J. Kimble, Nat. Photonics **9**, 320 (2015).

[169] G. Calajó, F. Ciccarello, D. Chang, and P. Rabl, Phys. Rev. A **93**, 033833 (2016).

[170] H. R. Haakh and S. Scheel, Phys. Rev. A **91**, 052707 (2015).

[171] S. Jennewein, L. Brossard, Y. R. P. Sortais, A. Browaeys, P. Cheinet, J. Robert, and P. Pillet, Phys. Rev. A **97**, 053816 (2018).

[172] R. Saint-Jalm, M. Aidelsburger, J. L. Ville, L. Corman, Z. Hadzibabic, D. Delande, S. Nascimbene, N. Cherroret, J. Dalibard, and J. Beugnon, Phys. Rev. A **97**, 061801 (2018).

[173] A. Browaeys (Private Communication), .

[174] H.-P. Breuer, E.-M. Laine, J. Piilo, and B. Vacchini, Rev. Mod. Phys. **88**, 021002 (2016).

[175] C. Lacroix, P. Mendels, and F. Mila, eds., *Introduction to Frustrated Magnetism*, Springer Series in Solid-State Sciences, Vol. 164 (Springer Berlin Heidelberg, Berlin, Heidelberg, 2011).

[176] N. Majlis, *The Quantum Theory of Magnetism* (World Scientific, 2000).